Mechanical Properties and Phase Transitions in Hard Polygons and the Origin of Colloidal Crystal Photonic Band Gaps

by

James Antonaglia

A dissertation submitted in partial fulfillment
of the requirements for the degree of
Doctor of Philosophy
(Physics)
in The University of Michigan
2019

Doctoral Committee:

Professor Sharon C. Glotzer, Chair
Professor Xiaoming Mao
Professor Roberto Merlin
Professor Robert Ziff

James Antonaglia

jamesaan@umich.edu

ORCID iD: 0000-0003-4287-0488

ACKNOWLEDGEMENTS

I would first like to thank my adviser Sharon C. Glotzer, my co-adviser and mentor Greg van Anders, and my committee member and mentor Xiaoming Mao. They have not only challenged me, but taught me to challenge myself, and they gave me the self-confidence I needed to continue through a lot of the difficulties I faced. Sharon taught me the value of good scientific communication and presentation, Greg taught me how to translate theory into practice, and Xiaoming helped me frame my work very early on to win a National Science Foundation Graduate Research Fellowship Prize. I am immensely indebted to their help.

Everyone in the Glotzer lab has helped me accomplish the work of this thesis; our community is strong and comprised of such a diverse group of students with a variety of expertises. Vyas Ramasubramani, Carl Simon Adorf, Bradley Dice, Matthew Spellings, and Joshua Anderson all helped me immensely to get my computer programs up and running correctly, and they always offered excellent constructive advice on best computation practices. I want to thank Wenbo Shen, Joshua Anderson, Carl Simon Adorf, Bradley Dice, and Rose Cersonsky for great opportunities to work on projects together. The most fun I have doing science is doing science with other people, lending out my skills and having them received with enthusiasm while receiving so many useful skills in return, and there couldn't be better collaborators to do that. I'd also like to thank James Proctor and Shannon Moran among many others for your valuable friendship in the lab; the culture we cultivated made the last several years engaging and rich. I want to thank Karen Coulter for all of her organization and helping me navigate the lab, especially when just starting.

Outside of the lab, there are many people without whom graduate school would've been

impossible to weather. I've had excellent roommates, Marie St. Peter and Melissa Robinson, turn into wonderful friends that taught me so much about cooking, now a favorite hobby of mine. My gaming playgroup, Christopher Brown, Ryan Dewey, Parker Koch, William Dean, Max Dubrinsky, Marcus Berger, and Christopher Altheim, gave me a great community and allowed me to show my creative and competitive side. My friends and colleagues at the Neutral Zone were instrumental in my developing desire to teach and be close to students.

Finally, I'd like to thank my family, Sue, Jim, and Laura Antonaglia, and my uncle Niel Hlavatovich for their unwavering support. Hearing from them in every phone call how proud they are of me kept me going through all the homework, all the computer bugs, and all the paper revisions. Lastly, I want to thank my partner Ángel Burciaga for his commitment, love, and support during my Ph.D.

TABLE OF CONTENTS

LIST OF FIGURES

LIST OF TABLES

C.2 Character table for the point group C_{4v}, which characterizes the symmetries of simple cubic at the Δ point ($\mathbf{k} = (2\pi/a, 0, 0)$). The columns are labeled by the operations of each conjugacy class: E is the identity operation, C_4^2 are rotations by π around the four-fold axis along the x-axis (100), C_4 are rotations by $\pi/2$ or $-\pi/2$ around the four-fold axis along the (100) axis, $2iC_4^2$ are rotoinversions by π around either the (010) or (001) axis, and $2iC_2$ are rotoinversions by π around either the (011) or (01$\bar{1}$) axis. The rows are listed by the five irreps of C_{4v}. There are four 1d irreps and only one 2d irrep. 81

LIST OF APPENDICES

Appendix

ABSTRACT

The synthesis of nanoparticles and colloids with anisotropic interactions and intricate shapes has led to the possibility of an assortment of complex self-assembled soft matter phases. In the first part of this work, I construct a theoretical minimal model to investigate the role of translational and rotational entropy in self-assembled solids of hard particles. Using computer simulations, I calculate the frequency of each normal mode of the solid and find the entropy contained in each translational and rotational wave. I show the entropy of a solid of hard hexagons is distributed nontrivially at many length scales among translational and rotational modes and construct maps in reciprocal space showing which fluctuations have more entropy. In the second part, I show that a solid of hard squares, like hard regular triangles, exhibit a strange high-density chiral symmetry-breaking transition. I show this transition is in the Ising universality class and that it is driven by a competition between rotational and translational entropy. In the third part of this work, I explore the origins of photonic band gaps in a wide variety of crystal structures formed of dielectric spheres. This problem has significant interest in the context of self-assembled soft matter as a route to design color-changing colloidal materials. I examine what characteristics of electromagnetic modes are responsible for opening a band gap in photonic materials. This problem is well-understood for photonics in two dimensions, but my coauthors and I show that the design heuristics developed for that problem do not hold in three dimensions.

CHAPTER I

Introduction

Plato's dichotomy between order and chaos [8] has a long intellectual history that pervades both the public and the academic imagination. Entropy, the name given to the force of disorder [24], is responsible for things generally falling apart. The basic principles of statistical mechanics state that a system of particles will adopt a macroscopic configuration that maximizes its entropy (subject to macroscopic constraints such as a constant temperature or constant pressure). Entropy is maximized when particles have the most available microstates, that is, options to configure themselves; it is said that there are many more ways to have a disordered mess of things than there are to have an organized arrangement of things. This definiton ostensibly names entropy as the quantifier of disorder.

A primary goal of the theory of statistical physics is to describe phase transitions, in which entropy plays a large role. Phase transitions are macroscopic changes in the properties of large systems of particles or constituents, and often entail a change in the degree of order [56]. For example, liquids are more disordered and thus have more entropy than solids do. However, maximizing the number of available configurations, that is, increasing the entropy, can lead to *order* instead of disorder. In fact, many phase transitions to more ordered states can be driven by entropy like rod-shaped liquid crystal particles [68, 53] and hard disks and spheres [3, 88].

Entropy-driven phase transitions confront Plato's dichotomy with an apparent paradox: a

macroscopically ordered system can exhibit more microscopic disorder than a macroscopically disordered system [35, 36]. For some transitions like entropy-driven liquid crystalline [35] and crystalline order [82], the "order from disorder" can be rationalized through intuitive arguments for simple enough model systems. For example, rod-like particles transit from an isotropic fluid to a nematic liquid crystal phase, because they gain translational entropy by aligning along one axis. Rotational entropy is "sacrificed" for translational entropy. However, resolving the order-from-disorder paradox for more complex types of order [41, 28, 2, 43] requires a detailed description of the entropy in an ordered system.

My first project attempts to address this question in Chapter II. Using a model system of hard hexagonal particles, which self-organize into an ordered crystal lattice through entropy alone, I decompose the entropy of the system into rotational and translational parts. This decomposition can, in principle, be performed on any ordered crystal structure in order to determine the relative contributions of rotation and translation to the solid's entropy.

My second project examines a bizarre entropy-driven phase transition that was first observed in hard triangles [89]. Hard triangles self-assemble into a honeycomb lattice and align themselves face to face. However, at a high density of around 87% packing fraction, the triangular particles prefer to twist some small angle while retaining the well-ordered honeycomb lattice. The particles can twist either clockwise or counterclockwise, thus undergoing *chiral symmetry breaking*. I show this transition also occurs in hard squares, and I explore the nature of this phase transition that is driven solely by entropy in Chapter III.

My third project, seemingly unrelated to the role of entropy in colloidal solids, concerns the properties of three-dimensional photonic crystals. A photonic crystal is a nano-structured periodic arangement of material that interact with light, such as dielectrics or metals. A lattice of dielectric material affects the motion of light through the material in much the same way that a lattice of atoms affect the motion of electrons through a material. Photonic crystals have a wide range of potential applications [62, 79, 52]. Two dimensional photonics have well-founded theoretical design principles [61], but principles to design photonic crystals

in three dimensions are based on general heuristics. I worked with Rose Cersonsky and Julia Dschemuchadse on an entropically stabilized colloidal crystal that exhibits a *photonic band gap* [19]; a band gap is a range of frequencies of light that does not propagate through the material, creating an ideal mirror. Motivated by this serendipitous discovery of a band gap material, Rose worked to develop a large database of photonic materials. My part in this project is to motivate design structural design principles by examining the motifs of electromagnetic field lines within a material, presented in Chapter IV.

Lastly, all the data for all three projects was maintained with the data management framework signac [1].

CHAPTER II

Constructing entropy maps for hard particle colloidal crystals

2.1 Introduction

The objective of this chapter is to characterize the entropy in an entropically stabilized colloidal solid [7]. The system selected was a two-dimensional system of hard regular hexagons. This is an ideal system to examine for a few reasons: 1) the group of rotations in the plane is one-dimensional, governed by one angle, 2) the equilibrium lattice configuration of hard regular hexagons has well-defined lattice positions and orientations, and 3) the equilibrium configuration is a triangular lattice with only one particle per unit cell. The large assumption to approach this system of hard particles is that the particles, rather than rattling against each others' hard surfaces, are interacting with each other *via* soft, differentiable, *effective* entropic potentials. This supposition lets us bring to bear on the problem all of the mathematical machinery used to describe the collective motion of atoms bound to each other by smooth potentials [12]. The total entropy of the system in its solid phase is governed by the thermal fluctuations of collective displacements and changes in orientation of all of the particles together, so this chapter examines the physics of these collective modes.

In Section 2.2, I describe the model used to analyze this system in depth and additionally describe the computational methods used. In Section 2.3, I present some data that supports

4

the assumptions made in modeling the particles with smooth, effective interactions. In Section 2.4, I present the dispersion relations for the system's collective modes which are used to calculate their contribution to the total entropy of the lattice.

2.2   Model and methods

In this section, I detail the mathematics of the harmonic model used to describe the lattice dynamics of the hard hexagon solid. The statistical properties of the soft, harmonic interaction potential is specified. I then detail the computational methods used to simulate and analyze the system.

2.2.1   Modeling billiard interactions with soft potentials

A universal property of crystalline solids is the support of collective, wave-like elementary excitations, *i.e.* phonons [20]. The properties of phonons in solids provide information about the potential that binds particles together. In a hard particle system, however, the potential is mathematically pathological; the energy is 0 if two particles do not overlap and ∞ otherwise. Nevertheless, hard particle solids support collective wave-like excitations, and the properties of these waves are determined by the *effective* entropic interactions between particles in the solid [48, 72, 77, 87]. Solids of hard particles with shape are also interesting in that they support *librational* waves or *librons*, wave-like excitations of the orientations of particles [71]. This type of wave is also seen in molecular crystals [25, 26, 29, 45].

All of the thermodynamic properties of a hard particle crystal are governed by its partition function, defined in the NVT ensemble as,

$$Z = \frac{1}{h^{3N}} \int \prod_i d^2\mathbf{p}^i dL^i \, e^{-\beta \mathcal{H}_{\text{kin}}} \int \prod_i d^2\mathbf{r}^i d\theta^i e^{-\beta \mathcal{H}_{\text{hard}}}. \tag{2.1}$$

The first integral over the linear and angular momenta of all the particles (indexed by i) contains all of the temperature dependence of the system and is governed by the kinetic energy

part of the Hamiltonian, $\mathcal{H}_{\text{kin}} = \sum_i (p^i)^2/2m + (L^i)^2/2I$. The second integral is governed by the hard particle interaction $\mathcal{H}_{\text{hard}}(\mathbf{r}^i, \theta^i)$, which is 0 for non-overlapping configurations of particles and ∞ otherwise. Because we know the hard particle system under consideration forms a well-ordered solid, we replace $\mathcal{H}_{\text{hard}}$ with an effective Hamiltonian $\mathcal{H}_{\text{eff}}$ that is quadratic in all the configurational degrees of freedom of the particles. This replacement will hereupon be referred to as the *harmonic approximation*. The harmonic Hamiltonian $\mathcal{H}_{\text{eff}}$ is the leading order interaction that stabilizes a crystalline solid, so instead of *a priori* coarse-graining the hard-particle interactions into an effective interaction, we posit *post facto* that the hard-particle solid is governed by this type of effective interaction. The harmonic interaction is fully characterized by the *dynamical matrix* $K^{ij}_{\mu\nu}$,

$$\beta\mathcal{H}_{\text{eff}} = \frac{1}{2} x^i_\mu K^{ij}_{\mu\nu} x^j_\nu, \quad \mathbf{x}^i = \begin{pmatrix} u^i_x & u^i_y & \theta^i \end{pmatrix}. \tag{2.2}$$

The generalized coordinate $\mathbf{x}^i$ is introduced to contain $\mathbf{u}^i$, the displacement of particle i from its equilibrium position, and θ^i, the angular displacement of particle i from its equilibrium orientation; μ and ν index over the components of $\mathbf{x}^i$ (Einstein summation notation is implied here). The matrix $K^{ij}_{\mu\nu}$ is a matrix of coupling constants that contains all of the information about which particles interact with which others and the strength of those effective interactions. This matrix is defined with an implicit factor of β to account for its completely entropic origin.

The dynamical matrix $K^{ij}_{\mu\nu}$ is partially diagonalized by a discrete Fourier transform,

$$x_\mu(\mathbf{k}) = \frac{1}{\sqrt{N}} \sum_i x^i_\mu e^{i\mathbf{k}\cdot\langle\mathbf{r}^i\rangle}. \tag{2.3}$$

Here, the average positions $\langle\mathbf{r}^i\rangle$ are taken to be on a triangular lattice with lattice spacing a; the wavevectors $\mathbf{k}$ then live in the hexagonal first Brillouin zone of the triangular dual

lattice. The effective harmonic Hamiltonian is then,

$$\beta\mathcal{H}_{\text{eff}} = \frac{1}{2}\sum_{\mathbf{k}} x_\mu(\mathbf{k})K_{\mu\nu}(\mathbf{k})x_\nu^*(\mathbf{k}). \tag{2.4}$$

Using this effective Hamiltonian, the partition function is then,

$$Z = \frac{1}{\Lambda^{2N}\theta_T^N}\prod_{\mathbf{k}}\int\sum_\mu dx_\mu(\mathbf{k})\,e^{-\frac{1}{2}x_\mu(\mathbf{k})K_{\mu\nu}(\mathbf{k})x_\nu^*(\mathbf{k})}. \tag{2.5}$$

Using a change of variables $u_\mu \to u_\mu/\Lambda$ and $\theta \to \theta/\theta_T$, the thermal wavelength Λ and thermal angle θ_T that result from integration over the particle momenta can be incorporated into the matrix $K_{\mu\nu}(\mathbf{k})$ to give all of its entries the same units:

$$Z = \prod_{\mathbf{k}}\int\sum_\mu dx_\mu(\mathbf{k})\,e^{-\frac{1}{2}x_\mu(\mathbf{TK}(\mathbf{k})\mathbf{T})_{\mu\nu}x_\nu^*}, \quad \mathbf{T} = \begin{pmatrix} \Lambda & 0 & 0 \\ 0 & \Lambda & 0 \\ 0 & 0 & \theta_T \end{pmatrix}. \tag{2.6}$$

This partition function is integrable exactly. Because there is no potential energy in the system at all, the free energy $F = U - TS = -TS$, so defining $k_B = 1$, the entropy is thus

$$S = -\beta F = \log Z = -\frac{1}{2}\sum_{\mathbf{k}}\log\det\left(\frac{\mathbf{TK}(\mathbf{k})\mathbf{T}}{2\pi}\right). \tag{2.7}$$

The matrix $\mathbf{T}$ is comprised of thermal wavelength factors, $\Lambda = h/\sqrt{2\pi m k_B T}$ and $\theta_T = h/\sqrt{2\pi I k_B T}$, where I is the moment of inertia of a hexagon. Setting $\hbar = k_B T = 1$, $\Lambda = 1/\sqrt{2\pi m}$ and $\theta_T = 1/\sqrt{2\pi I}$. In Section 2.3, I show that off-diagonal terms coupling $u_\mu(\mathbf{k})$ and $\theta(\mathbf{k})$ are zero under the harmonic approximation, so the matrix $\mathbf{T}$ commutes with all of the matrices $\mathbf{K}(\mathbf{k})$. The product $\mathbf{TKT}$ is then equivalent to $\mathbf{T^2K}$, the eigenvalues of which are frequencies of the normal modes of the crystal. The total entropy of the crystal is then

a sum of the logarithms of the normal mode frequencies,

$$S = -\frac{1}{2} \sum_{\mathbf{k}} \sum_{\mu} \log \omega_\mu^2. \tag{2.8}$$

Note that the phonon and libron entropies contain factors of the mass and moment of inertia, respectively, which account for the entropies of linear and angular momenta. The goal of simulating the system of hexagons is then to determine the matrices $\mathbf{K}(\mathbf{k})$ and thus the normal mode frequencies to compute contributions to the total entropy mode by mode.

2.2.2 Simulation and analysis methods

Simulations of hard hexagons were performed using the hard-particle Monte Carlo (HPMC) module [6] for HOOMD-blue [4, 38] in the NVT ensemble. System sizes of $N = 100^2$ hexagons were used for densities near the hexatic-solid transition [54, 65, 5], and 50^2 hexagons for higher packing fractions ($\phi > 0.75$). Systems were initialized into hexagonal lattices, thermalized and equilibrated at a selected density, and sampled over 1×10^7 Monte Carlo (MC) sweeps at high density, and 5×10^7 MC sweeps at low density. Four independent samples were run at each density.

To extract the entries of the dynamical matrices $\mathbf{K}(\mathbf{k})$, a generalized equipartition theorem is used. For a Hamiltonian harmonic in its degrees of freedom x_μ, the matrix of second order correlation functions is then related to the matrix of coupling constants $\mathbf{K}$ as

$$\langle x_\mu(\mathbf{k})x_\nu(\mathbf{k}')\rangle - \langle x_\mu(\mathbf{k})\rangle \langle x_\nu(\mathbf{k}')\rangle = k_B T K_{\mu\nu}^{-1}(\mathbf{k})\delta_{\mathbf{k}+\mathbf{k}',0}. \tag{2.9}$$

For the Fourier modes studied here, the mean $\langle x_\mu(\mathbf{k})\rangle = 0$. The matrices $K_{\mu\nu}(\mathbf{k})$ are then taken from sufficiently sampled correlation functions; this method is often referred to as *displacement covariance analysis* (DCA) [44]. For each density, 4000 total independent frames are taken to calculate the correlation functions between Fourier modes.

There is a difficulty obtaining accurate estimates for the correlation functions $\langle x_\mu(\mathbf{k})x_\nu^*(\mathbf{k})\rangle$

for densities lower than around $\phi = 0.75$. Particles at this density have enough room to diffuse away from the lattice sites that they began the simulation at, swapping positions with other nearby particles. This confounds the calculation of a meaningful displacement vector, $\mathbf{u}^i = \mathbf{r}^i - \langle \mathbf{r}^i \rangle$. At these densities a method for estimating the Fourier modes $x_\mu(\mathbf{k})$ needs to be agnostic of which particle distinguishably belongs to a particular equilibrium lattice position. A method to do this was developed by Walz and Fuchs using Zwanzig-Mori hydrodynamic projection operators [64, 91, 83]. This method is detailed in Appendix B. Even though it agrees with DCA at high densities, its implementation is significantly slower than DCA, so it is only used to obtain the dynamical matrix elements at densities $\phi \leq 0.75$.

2.3 Validating assumptions

In this section, I validate two large assumptions that are made in formulating the mode-by-mode entropy decomposition of the previous section. The first is that the harmonic approximation accurately describes the physics of the hard hexagon solid. This assumption can be verified *post facto* by measuring the degree of anharmonicity and by calculating the system's total entropy by an independent method. The second is that the libron and phonon modes are decoupled from each other. I show that this assumption holds given a sufficiently symmetric space group of the equilibrium solid state, and I measure the degree of coupling between the two types of modes.

2.3.1 Measuring anharmonicity

To validate the harmonic approximation, the total entropy of the hard hexagon solid as calculated by summing over normal modes is compared to the total entropy calculated using the equation of state of the system, shown in Figure 2.1. For this system of hard particles where interaction energies are either infinite or zero, the system pressure is directly proportional to the temperature, so the total entropy can be computed by integrating the

9

pressure *via* a Maxwell relation,

$$\left.\frac{\partial S}{\partial V}\right|_{N,T} = \left.\frac{\partial P}{\partial T}\right|_{N,V} = \frac{P}{T}.$$

I find excellent agreement on the total entropy using both thermodynamic integration and harmonic mode-by-mode decomposition until around $\phi = 0.72$. Hard regular hexagons transit to the hexatic phase around $\phi = 0.71$, so the harmonic solid approximation is expected to break down near this density. That the harmonic approximation quantifies the total entropy of the system so well is consistent with the surprisingly harmonic behavior of a hard sphere crystal shown in experiment by Cheng *et al.* [22].

Additionally, the degree of anharmonicity can be quantified mode-by-mode rather than by its effect on the total entropy. For harmonic degrees of freedom, fourth-order correlation functions $\langle x_\mu x_\nu x_\sigma x_\gamma \rangle$ decompose into sums of products of second-order correlation functions (for a reference of the properties of Gaussian distributions relevant here, see Appendix A). For systems of 10^4 particles, this makes an intractible array with $\mathcal{O}(10^{16})$ entries (after having accounted for the total permutation symmetry in the indices). Many of these entries are very small compared to other entries, so we restrict our examination of this correlation function to the following form:

$$A_{\mu\nu}(\mathbf{k}_1, \mathbf{k}_2) = \langle x_\mu(\mathbf{k}_1) x_\mu^*(\mathbf{k}_1) x_\nu(\mathbf{k}_2) x_\nu^*(\mathbf{k}_2) \rangle. \tag{2.10}$$

If the quadratic approximation is a good one, then $A_{\mu\nu}(\mathbf{k}_1, \mathbf{k}_2)$ should break up into a sum of three terms:

$$A_{\mu\nu}(\mathbf{k}_1, \mathbf{k}_2) \approx S_{\mu\nu}(\mathbf{k}_1, \mathbf{k}_2) = \langle v_\mu(\mathbf{k}_1) v_\mu^*(\mathbf{k}_1) \rangle \langle v_\nu(\mathbf{k}_2) v_\nu^*(\mathbf{k}_2) \rangle$$

$$+ \langle v_\mu(\mathbf{k}_1) v_\nu^*(\mathbf{k}_2) \rangle \langle v_\mu(\mathbf{k}_1) v_\nu^*(\mathbf{k}_2) \rangle + \langle v_\mu(\mathbf{k}_1) v_\nu(\mathbf{k}_2) \rangle \langle v_\mu^*(\mathbf{k}_1) v_j^*(\mathbf{k}_2) \rangle. \tag{2.11}$$

In the harmonic approximation, the first term on the right-hand side is nonzero for all choices

of $\mathbf{k}_1$ and $\mathbf{k}_2$. Therefore, restricting the generalized 4-point correlation function to the form defined by $A_{\mu\nu}(\mathbf{k}_1, \mathbf{k}_2)$ yields at least one term that's generally nonzero. Even this restriction gives us $\mathcal{O}(10^9)$ possible entries for a system of 10^4 particles, so we further only choose $\mathbf{k}$-vectors that lie along the high-symmetry paths shown in the plots of the original manuscript ($\Gamma \to M \to K \to \Gamma$).

We compute the array $A_{\mu\nu}(\mathbf{k}_1, \mathbf{k}_2)$ and the sum of two-point functions $S_{\mu\nu}(\mathbf{k}_1, \mathbf{k}_2)$ and their ratio A/S. We histogram the ratio A/S at low, medium, and high densities ($\phi = 0.74, 0.8, 0.9$), shown in Figure 2.2. The distribution of ratios has a standard deviation of 0.03 at all three densities, which supports the hypothesis that the harmonic approximation captures the statistical behavior of the hard particle crystal's degrees of freedom.

2.3.2 Measuring libron-phonon coupling

If there is coupling between the libron and phonon modes at second order, the eigenmodes of the dynamical matrix will generally be linear combinations of rotational and translational fluctuations. In this case, the total entropy, which breaks up into a sum of logarithms of the eigenfrequencies, is not interpretable as a sum of purely translational and purely rotational parts. In this section, I show that if the solid system is sufficiently symmetric, the harmonic coupling between libron and phonon modes is guaranteed to be zero. It is easiest to find the requisite symmetries that guarantee phonon and libron decoupling in a continuum elastic picture of the solid, rather than a microscopic mechanical picture. The general elastic energy for a solid with a particle orientation displacement field $\theta(\mathbf{r})$ and infinitesimal strain tensor $u_{ij}(\mathbf{r})$ to second order in these fields and up to second order in spatial derivatives is

$$\mathcal{U}^{(2)} = \int d^2r \, \frac{1}{2}C_{\mu\nu\sigma\gamma}u_{\mu\nu}u_{\sigma\gamma} + \frac{1}{2}B_+\theta^2 + \frac{1}{2}B_- \left(\partial\theta\right)^2 + F_{\mu\nu}u_{\mu\nu}\theta + G_{\mu\nu\sigma}\theta(\partial_\mu u_{\nu\sigma}). \quad (2.12)$$

$F_{\mu\nu}$ and $G_{\mu\nu\sigma}$ are tensors quantifying the cross-coupling between $u_{\mu\nu}$ and θ. Under a rotation of the coordinate axes by ϕ, the tensor $u_{\mu\nu}(\mathbf{r})$ transforms to $u'_{\mu\nu}(\mathbf{r}') = R_{\mu\sigma}R_{\nu\gamma}u_{\sigma\gamma}(\mathbf{r})$, where

11
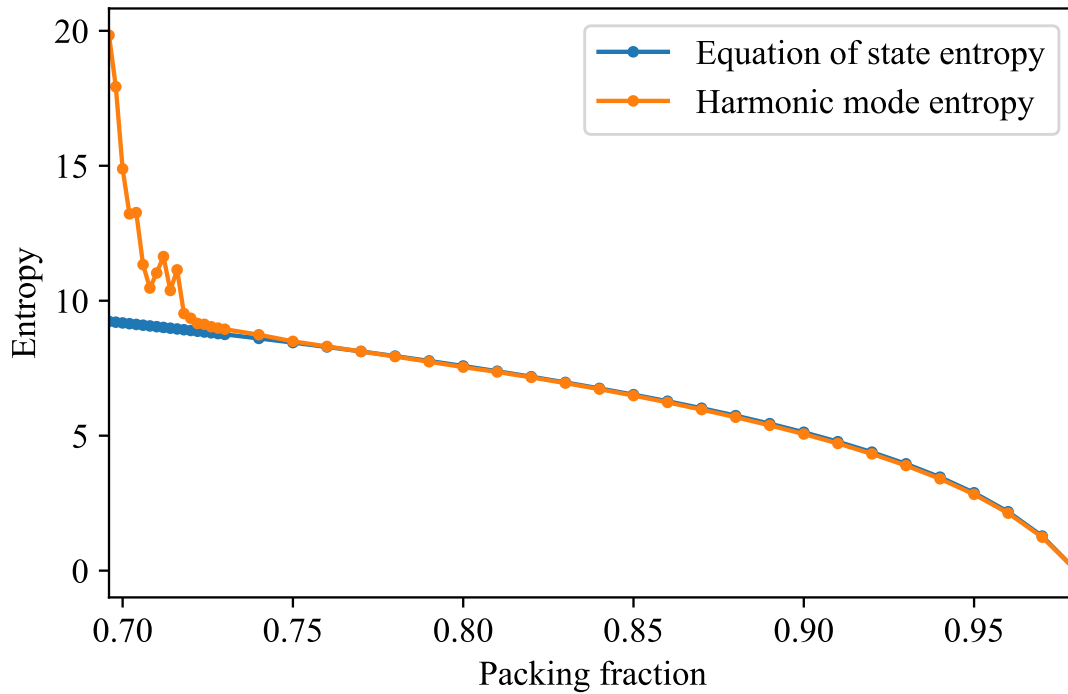
Figure 2.1: Total entropy per particle calculated both using the Maxwell relation $\frac{\partial S}{\partial V} = \frac{\partial P}{\partial T}$ and by counting the individual entropic contributions of each harmonic mode. The entropy is set to 0 arbitrarily at $\phi = 0.98$ to better compare the two methods. There is excellent agreement between the two methods that diverges only when the system gets close to melting, where the harmonic approximation becomes invalid.
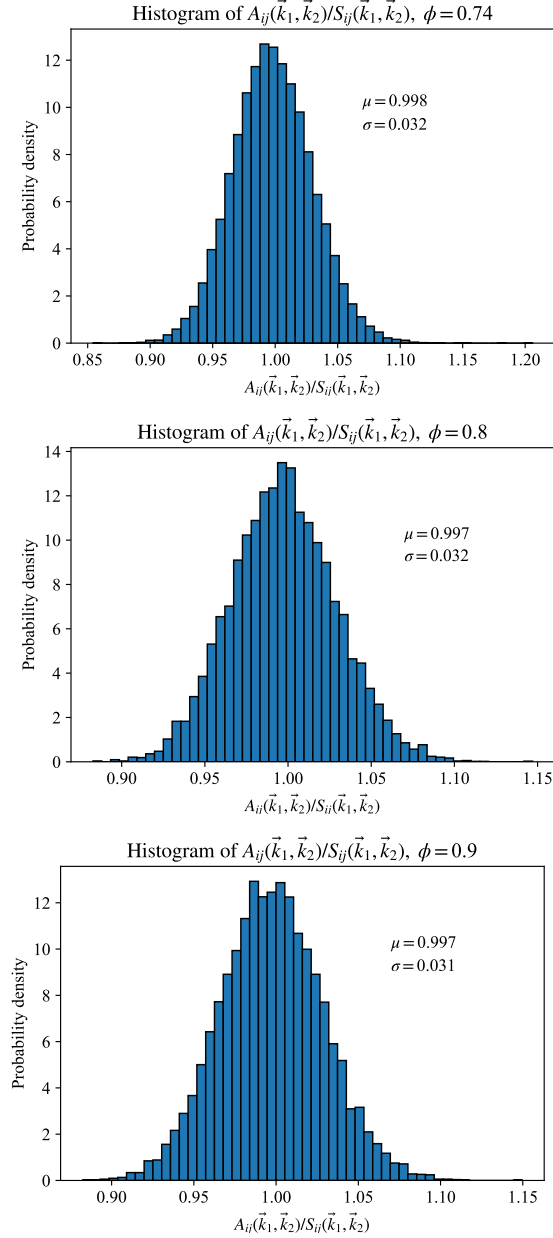
Figure 2.2: The ratio of four-point correlation functions to the sums of products of two-points correlation functions. This quantity can be calculated for any four degrees of freedom; presented here is a histogram of ratios of four-point functions to sums of products of two-point functions. A value of 1 indicates perfect decomposition of a four-point correlation function into products of two-points functions. That the standard deviation of this quantity is small and constant for many densities indicates the quality of the harmonic approximation.

$R_{\mu\sigma}$ is a rotation matrix. The field $\theta(\mathbf{r})$ transforms like a scalar under rotations, because the equilibrium angle also rotates. However, under inversion through a mirror plane, the θ field transforms with a minus sign, that is, $\theta'(\mathbf{r}') = -\theta(\mathbf{r})$. This transformation can be written as $\mathbf{M} = \begin{pmatrix} 1 & 0 \\ 0 & -1 \end{pmatrix}$. If the crystal symmetry includes a mirror plane, the energy density $F_{\mu\nu}u_{\mu\nu}(\mathbf{r})\theta(\mathbf{r})$ must be invariant under $u_{\mu\nu}(\mathbf{r}) \rightarrow u'_{\mu\nu}(\mathbf{r}') = M_{\mu\sigma}M_{\nu\gamma}u_{\sigma\gamma}(\mathbf{r})$ and $\theta(\mathbf{r}) \rightarrow \theta'(\mathbf{r}') = -\theta(\mathbf{r})$. This symmetry thus restricts the form of $F_{\mu\nu}$:

$$F_{\mu\nu} = -M_{\mu\sigma}M_{\nu\gamma}F_{\sigma\gamma}.$$

This condition requires $F_{11} = F_{22} = 0$ but does not restrict F_{12}. However, if the crystal structure also exhibits some rotational invariance, another condition on $F_{\mu\nu}$ is generated:

$$F_{\mu\nu} = R_{\mu\sigma}R_{\nu\gamma}F_{\sigma\gamma}, \quad \mathbf{R} = \begin{pmatrix} \cos\frac{2\pi}{n} & -\sin\frac{2\pi}{n} \\ \sin\frac{2\pi}{n} & \cos\frac{2\pi}{n} \end{pmatrix}.$$

Here, the n-fold rotational symmetry of the structure is expressed in $\mathbf{R}$. For $F_{11} = F_{22} = 0$, this condition reduces to $\left(\cos\frac{4\pi}{n} - 1\right)\mathbf{F} = 0$ which restricts $\mathbf{F} = 0$ for $n \geq 3$. Thus, the plane groups with point groups $D_{3,4,6}$ guarantee $F_{ij} = 0$—in this work, the hard hexagon solid exhibits D_6 symmetry. This symmetry condition is *sufficient* but not *necessary* to produce zero libron-phonon coupling. Likewise, $G_{\mu\nu\sigma}$ is constrained by at least two mirror planes to be equal to zero, leading to the decoupling of the phonon and libron modes. In general, higher order, anharmonic couplings involving three or more factors of $u_{\mu\nu}$ and θ or three or more derivatives can introduce couplings between the phonons and librons. For example, an anharmonic term proportional to $u_{\mu\mu}\theta^2$, which would be permitted under the symmetries that disallow a term such as $u_{\mu\mu}\theta$, would generate nonzero couplings between phonons and librons at harmonic order.

To quantify these anharmonic contributions to the dynamical matrix at harmonic order,

the total entropy of the system is calculated using Equation 2.7. The eigenvalues are calculated using the dynamical matrices $\mathbf{K}(\mathbf{k})$ and then calculated again explicitly neglecting the off-diagonal components coupling the phonons and librons. The difference between these two total entropies, shown in Figure 2.3, then quantifies the contribution of phonon-libron coupling to the frequency spectrum of the solid. That the difference in entropy is on the order of $0.01k_BT$ for all densities, even densities near melting where the harmonic approximation is less reliable, shows the coupling between phonons and librons to be sufficiently small to be neglected at harmonic order.
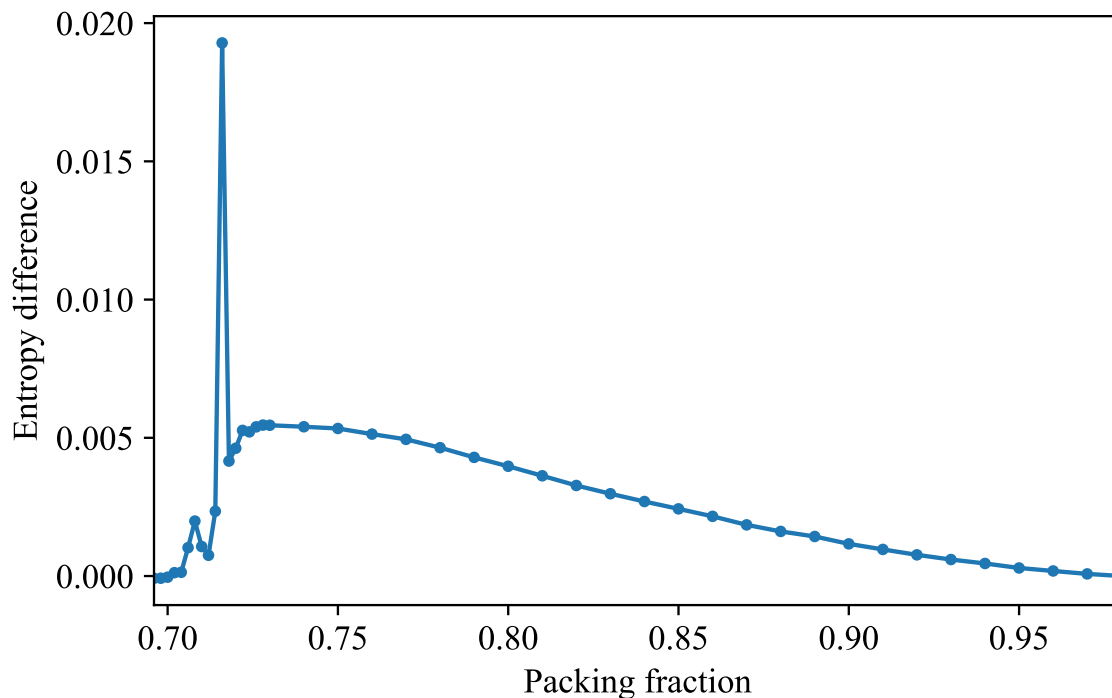
Figure 2.3: Difference in the total entropy per particle if harmonic coupling between librons and phonons are neglected or included. The difference is less than $0.01k_BT$ for all densities sufficiently above melting, which shows that any harmonic-order cross-coupling is attributable to higher-order interactions.

2.4 Mapping the entropy from dispersion relations

In this section, I explore the decomposition of the total entropy of the hard hexagon solid mode by mode, justified by the analysis of the previous section.

2.4.1 Computing dispersion relations at all densities

The dispersion relation, the relation that gives the frequency of a wave as a function of its wavevector, determines the total entropy of a hard particle solid, as discussed in Section 2.2. The wavevector for the hard hexagon solid lives in the first Brillouin zone (BZ) of the triangular lattice, which is a hexagonal region of k-space.

Presented in Figure 2.4 are phonon and libron dispersion relations for a range of densities for high symmetry points in the Brillouin zone. The dispersion relations shown also contain dashed lines signifying a theoretical prediction for the form of the curves fit to the data. This theoretical prediction is based on a micromechanical balls-and-springs-like model of the hexagons on a triangular lattice interacting with each other's nearest neighbors by a harmonic spring interaction with spring constants A, B_+, and B_-. In this model, each hexagon has six neighbors defined by the real space lattice vectors $\{\pm\mathbf{a}_1, \pm\mathbf{a}_2, \pm\mathbf{a}_3 = \pm(\mathbf{a}_1 + \mathbf{a}_2)\}$, the dynamical matrix $K_{\mu\nu}(\mathbf{k})$ is

$$K_{11}(\mathbf{k}) = 2A \sum_{\mathbf{a}_i} \hat{a}_{i,x}\hat{a}_{i,x} \sin^2 \frac{\mathbf{k} \cdot \mathbf{a}_i}{2}. \tag{2.13}$$

$$K_{12}(\mathbf{k}) = 2A \sum_{\mathbf{a}_i} \hat{a}_{i,x}\hat{a}_{i,y} \sin^2 \frac{\mathbf{k} \cdot \mathbf{a}_i}{2}. \tag{2.14}$$

$$K_{22}(\mathbf{k}) = 2A \sum_{\mathbf{a}_i} \hat{a}_{i,y}\hat{a}_{i,y} \sin^2 \frac{\mathbf{k} \cdot \mathbf{a}_i}{2}. \tag{2.15}$$

$$K_{33}(\mathbf{k}) = 2B_- \sum_{\mathbf{a}_i} \sin^2 \frac{\mathbf{k} \cdot \mathbf{a}_i}{2} + 2B_+ \sum_{\mathbf{a}_i} \cos^2 \frac{\mathbf{k} \cdot \mathbf{a}_i}{2}. \tag{2.16}$$

Here, the sum $\sum_{\mathbf{a}_i}$ represents the sum over all six neighbor vectors. The off-diagonal components coupling phonons and librons $K_{13} = K_{23} = 0$, as discussed in Section 2.3.2. Inclusion

of next-nearest neighbor interactions would furnish terms proportional to new coupling constants A_2 and $B_{2,\pm}$, and those terms would depend on sums over lattice vectors joining next-nearest neighbors. A model including these second-neighbor coupling constants can be used to fit the dispersion curves from simulation, but are generally an order of magnitude smaller than the first-neighbor constants, as shown in Figure 2.5.

There are several features of the dispersion relations that are common at all densities. First, we find deviations between our simulation data and the linear elastic model are only appreciable near the edge of the Brillouin zone. The edges correspond to short distances, and is precisely where we would expect a linear elastic model of hard interactions to break down. Although deviations increase with density as expected, we find that the linear elastic model provides a good approximation for most of the Brillouin zone, even for relatively high densities of 0.9. Second, we find that phonon modes are always ungapped, which is guaranteed by Goldstone's theorem. Third, we find that the libron modes are gapped at all densities, but that their group velocity increases rapidly with system density.

Now with the dispersion relations, with Equation 2.7, the entropy of each individual mode is calculated.

2.4.2 Mode-by-mode decomposition of the total entropy

The entropy of any mode with frequency ω is simply $-\log \omega$, as determined in Equation 2.7. The entropy thus can be plotted over the entire Brillouin zone, shown in Figure 2.6. Brillouin zones are shown in this figure as "entropy maps," in which all points are colored according to the mode that provides more entropy than any other mode at that wavevector, using Eq. 2.7.

A similar entropy map results at densities just above the hexatic-solid transition ($\phi = 0.722$) and close to dense packing ($\phi = 0.9$) in which entropy at all wavevectors comes predominantly from translational disorder, though for different reasons. The predominance of translational disorder just above the hexatic-solid transition arises because, although the
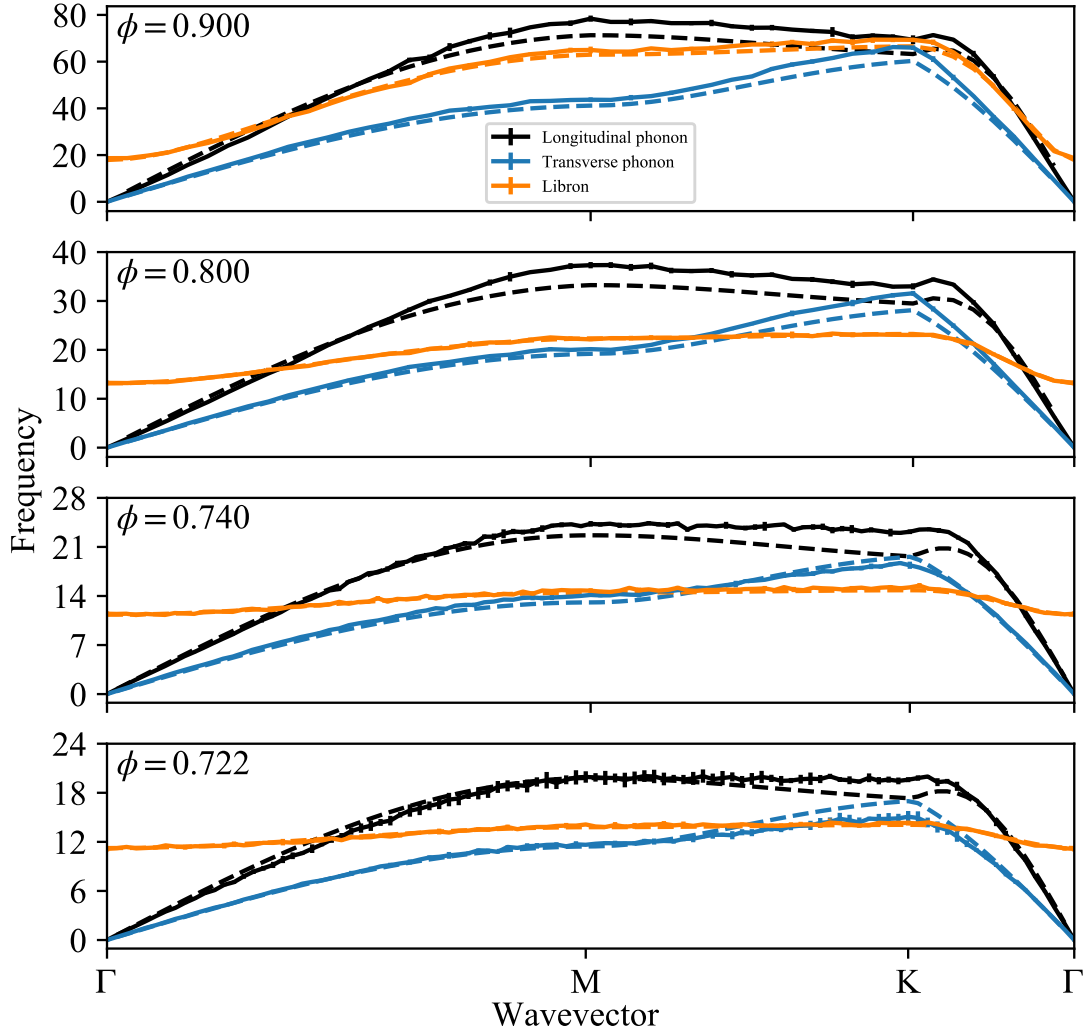
Figure 2.4: Dispersion relation for hard hexagon crystals at various packing fractions across a high-symmetry path in the first Brillouin zone. All dispersion relations decrease with decreasing density, but the phonon dispersions become ill-defined at densities close to the hexatic-solid phase transition. Dashed lines indicate theoretical dispersion relations with best-fit stiffness parameters. Error bars are 1-σ sample standard deviations of the dispersion frequencies averaged from four independent simulations.
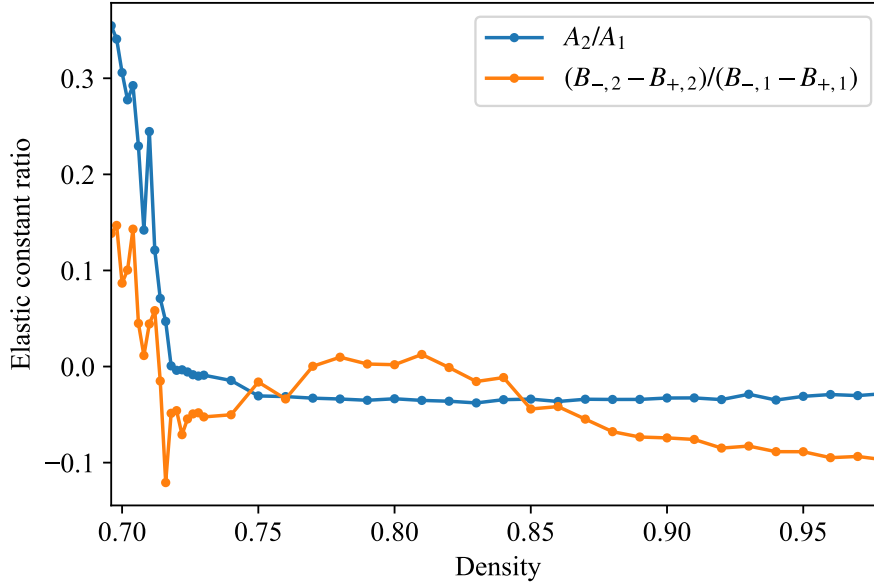
Figure 2.5: Second-neighbor elastic constants compared to those from nearest-neighbor inter-actions. Second-neighbor interactions are generally much weaker than nearest-neighbor interactions, but become more important nearer the melting point. Though, at these densities, the harmonic approximation loses validity.

libron group velocity (the slope of its dispersion relation) is small, the libron mass gap remains robust while the phonon frequencies soften as the hexatic phase is approached, which is orientationally ordered but translationally disordered [65]. This behavior is in contrast to what occurs at high densities, though the entropy map is the same. At high densities the phonon and libron group velocity are comparable, but the libron mass gap pushes its frequencies above those of the transverse phonon. That the libron is gapped is a generic feature of orientationally ordered anisotropic solids [85, 16], so I expect this feature to generalize to other hard particle solids. However, the hexatic-solid transition is not a generic feature of all hard particle solids; in fact, hard polygons demonstrate rich melting behavior [5], and their entropy maps could offer useful insight into distinguishing the melting behavior of different systems without the need for large and long melting simulations.

I end this chapter with a few qualitative remarks on the hard hexagon system used to illustrate the mode-by-mode entropy decomposition approach. The entropy maps in
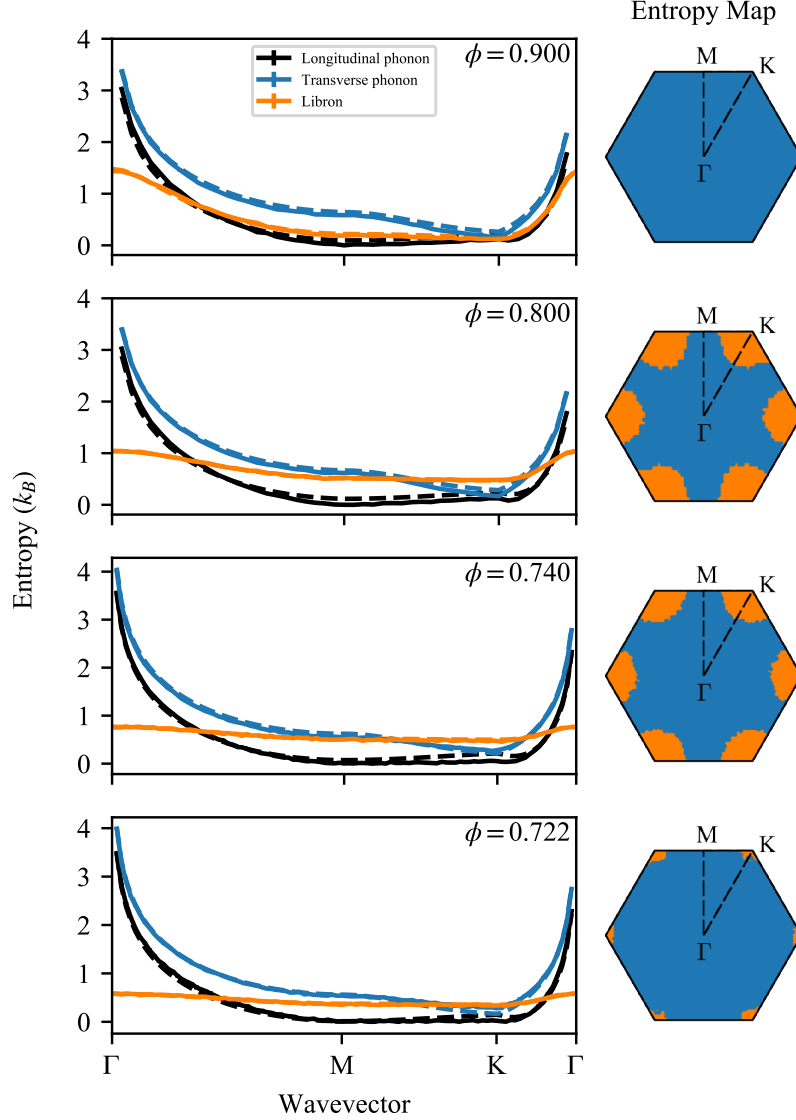
Figure 2.6: Contributions to the total entropy of the hard hexagon solid decomposed mode by mode. The entropy of each mode is $-\log \omega$. Error bars are smaller than the line thickness. Dashed lines indicate entropies from theoretical dispersion relations with best-fit stiffness parameters. Right panels are the first Brillouin zone where each **k**-point is colored orange if the frequency of the libron is lower than that of the transverse phonon and blue otherwise. This coloring offers a "map" of **k**-space that identifies which modes have the highest entropy (lowest frequency). At both high and low densities, phonons are mostly always of lower frequency than librons at any **k**-point, so their entropies are always larger than libron entropies regardless of length scale. However, at intermediate densities, the entropy (frequency) map has nontrivial structure where librons contribute more to the system entropy at short wavelengths. Here we are interested in comparisons between entropies of different modes, but for the purposes of plotting the entropies we arbitrarily define the total entropy of the hard hexagon solid to be 0 at $\phi = 0.98$, the highest density simulated.

Figure 2.6 provide insight into both the long-wavelength and short-wavelength physics of the hexagon solid. At long wavelengths (small k), translational entropy contributes by far the most to the entropy of the solid. Long-wavelength properties such as elastic moduli are therefore likely insensitive to properties of the solid characterized by particle rotations, like detailed particle shape. On the other hand, short-wavelength physics (k near the edge of the BZ), is governed by both rotational and translational entropy nearly equally. It is thus on short length scales that particle shape becomes important.

In the next chapter, I apply some of the tools used in this project to analyze two other systems of hard polygon solids: the hard square solid and the hard triangle solid, particularly at very high density where they exhibit a strange chiral symmetry-breaking phase transition.

CHAPTER III

Chiral symmetry breaking in hard regular polygons

3.1 Introduction

A variety of achiral hard particles have been previously shown to form chiral structures. Zhao *et al.* found in experiment that rounded regular triangles exhibit a chiral symmetry breaking transition [89], and Zhao and Mason found a similar transition in hard square crosses [90]. Carmichael and Shell demonstrated in simulation that rounded triangles, rounded rectangles and rounded squares undergo phase transitions at high densities to chiral structures due to the dependence of the densest packing structure on density and particle roundness [17]. Mayoral and Mason showed in simulation that hard rhombs exhibit chiral symmetry breaking and provided a mean-field argument for the favorability of the chiral state based on the phase space volume available to a single rhomb in a frozen cage of its neighbors [60]. Gantapara, Qi, and Dijkstra find a chiral transition for both regular and right isosceles triangles in simulation [37]. Additionally, Pakalidou *et al.* observed a chiral symmetry breaking transition in concave platelets [70].

In this chapter, I show that hard squares undergo the same chiral transition as found in hard regular triangles in [37]. I additionally corroborate the results of Gantapara *et al.* with my own simulations of hard triangles. In Section 3.2, I describe the hard particle systems under study, the approaches I use to analyze them, and the computational methods used to simulate them. In Section 3.3, I provide and examine the data that identifies the

chiral transition, such as equations of state and the density dependence of moments of the order paramter. In Section 3.4, I characterize the chiral transition by performing finite-size scaling analysis on both the square and triangle systems. I find that, for squares, the critical exponent ν associated with the diverging correlation length is 0.97 ± 0.08 and the exponent β governing the decay of the order parameter is 0.13 ± 0.03. The triangle exponents are $\nu = 0.98 \pm 0.08$ and $\beta = 0.15 \pm 0.008$. These exponents are consistent with the exponents of the 2D Ising order-disorder transition, which has $\nu = 1$ and $\beta = \frac{1}{8}$. In Section 3.5, I use the methods of Chapter II to compute the rotational and translational entropy through the chiral transition.

3.2   Model and methods

In this section, I review the theory of continuous phase transitions and scaling theory in finite-sized systems, referring mostly to Nightingale, Binder, and Fisher among others [55, 66, 13]. This theory is required to determine the critical exponents of the chiral transition and identify its universality class, *i.e.*, what other continuous transitions it behaves like near the critical point [39]. Then, I describe the computational methods used to simulate and analyze the transitions.

3.2.1   Continuous phase transitions at finite system size

A phase transition can be characterized by an order parameter that distinguishes two phases with a value of zero in the disordered phase and a nonzero value in the ordered phase. A continuous transition occurs when this order parameter changes continuously from zero to nonzero as a tuning parameter is changed [39]. In the commonly treated Ising transition, the order parameter is the total magnetization, and the tuning parameter is the temperature; the magnetization is zero for temperatures above the critical temperature T_C and nonzero below it. The tuning parameter, usually denoted $t = (T - T_C)/T_C$, is a dimensionless distance to criticality. For the hard particle system in this chapter, I use $t = (\phi - \phi_C)/\phi_C$, as the system

density ϕ is the tuning parameter for the chiral transition.

The order parameter that characterizes the chiral transition is θ, the mean chiral angle,

$$\theta = \frac{1}{N} \sum_i \theta^i. \tag{3.1}$$

Here, θ^i is the angle the ith particle's body makes with respect to the equilibrium orientation θ_0 modulo the rotational symmetry of the particle. For squares, θ_0 can be set to zero generally, but the hard triangle solid exhibits a unit cell with antiparallel particle constituents, so θ_0 is zero for one particle and π for the other.

Continuous phase transitions are characterized by a diverging correlation length as the system approaches its critical point. Fluctuations of particle motion become correlated over extremely long distances, and that distance becomes infinite at the critical point. In an infinite system, in the ordered phase, the order parameter follows a power law near the critical point,

$$\theta(t) \sim |t|^\beta. \tag{3.2}$$

The value of the exponent β is the same for any transition said to belong to the same *universality class*. The divergence of the correlation length is governed by another exponent ν:

$$\xi(t) \sim |t|^{-\nu}. \tag{3.3}$$

The correlation length is defined above and below the critical density, so I use the notation $|t|$ to take care of when t is positive or negative.

In finite systems, this divergence poses difficulties for transitions in finite-sized systems, like those necessarily run on computers that may only contain a few thousand particles rather than 10^{23}. Because the correlation length ξ cannot grow beyond the size of the system L, the above scaling relations are modified by *scaling functions* described by *finite size scaling theory*. The system is no longer governed by a single length scale ξ near the critical point,

24

but rather the ratio L/ξ. The order paramter $\theta(t)$, now a function of L, behaves as,

$$\theta(t, L) = |t|^\beta f\left(L\xi^{-1}\right) = |t|^\beta f\left(Lt^\nu\right) = L^{-\beta/\nu} f'\left(Lt^\nu\right). \tag{3.4}$$

$f\left(L\xi^{-1}\right)$ is some scaling function that depends only on the nondimensionalized quantitiy L/ξ, but using the scaling relationship between ξ and t from Equation 3.3, f can be written as a function of Lt^ν, or equivalently, $tL^{1/\nu}$. By multiplying this function by $(tL^{1/\nu})^{-\beta/\nu}$, the prefactor $|t|^\beta$ can be eliminated in favor of $L^{-\beta/\nu}$, implicitly specifying a new scaling function $f'(tL^{1/\nu})$. This manipulation, seemingly cosmetic, leads to the important practical result that the function

$$f'(tL^{1/\nu}) = L^{\beta/\nu}\theta(t, L), \tag{3.5}$$

is only a function of the combined variable $tL^{1/\nu}$.

Plotting the combined quantity $L^{\beta/\nu}\theta(t, L)$ against the combined quantity $x = tL^{1/\nu}$ for many system sizes L yields one universal curve $f'(x)$. This technique, referred to as *data collapse*, is a straightforward approach to identify not only the critical density ϕ_C implicitly defined in t, but also the values of the exponents β and ν. The values ϕ_C, β, and ν are manipulated until all curves for each L lay on top of each other, that is, they collapse to a universal curve.

Scaling forms can be found for the nth moment of the order parameter θ. The nth moment is calculated as,

$$M_n(t, L) = \langle \theta^n \rangle_L = \left\langle \frac{1}{N}\sum_i (\theta^i)^n \right\rangle_L. \tag{3.6}$$

Here, $\langle \cdot \rangle_L$ signifies an ensemble average in a system of linear dimension L (in simulations, this ensemble average is an average over independent frames of a simulation). $L = a\sqrt{N}$ for squares and $L = a\sqrt{\frac{N}{2}}$ for triangles, where a is the lattice constant at packing fraction ϕ. Finite-size scaling theory shows that the quantity $M_n(\phi, L)$ takes the following form near

the critical point ϕ_C [55, 13]:

$$M_n(t, L) = L^{-n\beta/\nu} f_n \left(t L^{1/\nu} \right). \tag{3.7}$$

Here, $f_n(x)$ are more universal scaling functions. The Binder cumulant [13] is a useful quantity to compute to determine ϕ_C with high accuracy and to determine ν; it is defined in terms of the second and fourth moments:

$$U(t, L) = 1 - \frac{M_4(t, L)}{3M_2^2(t, L)} = f_U \left(t L^{1/\nu} \right). \tag{3.8}$$

Here, $f_U(x)$ is another universal scaling function that is some combination of $f_2(x)$ and $f_4(x)$. The exponent β has been eliminated, so only the two quantities ϕ_C and ν need to be tuned. Furthermore, $U(t, L)$ achieves the universal value U^* at $\phi = \phi_C$ or $t = x = 0$ regardless of the system size L. Plotting $U(t, L)$ as a function of ϕ for many values of L thus identifies the critical density ϕ_C as the density at which all the $U(\phi, L)$ are equal and intersect, circumventing the need to do any fitting or collapsing. With a sufficiently good estimate for ϕ_C, performing a collapse of $U(t, L)$ for multiple values of L is significantly easier and provides a good estimate for ν. Alternatively, collapses can be performed on the moments $M_n(t, L)$ directly to obtain both ν and β.

3.2.2 Simulation methods

Simulations were run with the hard particle Monte Carlo (HPMC) module of HOOMD-blue [4, 6] in the NVT ensemble with fixed box sides and angles under periodic boundary conditions, the same conditions used in Chapter II. A random translation or rotation is proposed for a particle, then that proposed move is accepted if the particle overlaps no other particles and rejected otherwise; a single MC sweep is comprised of one proposed move per particle. Systems are initialized in their close-packed lattice structure and run for 3×10^8 MC sweeps for squares and for 2.4×10^8 MC sweeps for triangles. The first 5×10^7 sweeps for

squares (4×10^7 for triangles) equilibrate the system, then 10^3 snapshots were taken in the remainder of the simulation. These simulations are long to ensure statistically independent sample snapshots; the chiral transition occurs at high packing fraction, which entails long vibrational autocorrelation times ($\tau \approx 10^4$ MC sweeps for long wavelength vibrations). For each density, four independent replicas were run with different initial random seeds. Square systems were run with particle numbers $N = 32^2$, 64^2, 128^2, 192^2, and 256^2, and triangle systems were run with $N = 2 \times 64^2$, 2×128^2, and 2×256^2 to account for the two-particle unit cell of their close-packed structure. The pressure was calculated at each packing fraction using the scale distribution function method available in HOOMD [33]; the equation of state is shown in Figures 3.3 and 3.4. This simulation protocol ensures 4000 statistically independent sample snapshots for each tested density and system size, which is sufficient to study the chiral transition using finite-size scaling techniques.

3.3   Identifying the chiral transition

The chiral transition for hard squares and triangles is a continuous transition that: 1) maintains the underlying crystal lattice, 2) leaves no discernible signal in the equation of state, and 3) is described by an order parameter that has statistical behavior typical of an Ising-like transition. Figure 3.1 plots the angle the simulation box makes in an NPT simulation of hard squares, where the box edges are allowed to flexibly fluctuate in length and angle. That the angle remains $90°$ through the transition indicates the underlying Bravais lattice is preserved, if only compressed as the density increased. Figure 3.2 shows for $N = 256^2$ hard squares the critical fluctuations of the order parameter near the critical point.

In the following subsections, I explain that the equation of state is typical of continuous transitions. Then I show some raw data, the moments of the order parameter for both systems. These statistical quantities help identify the critical density.
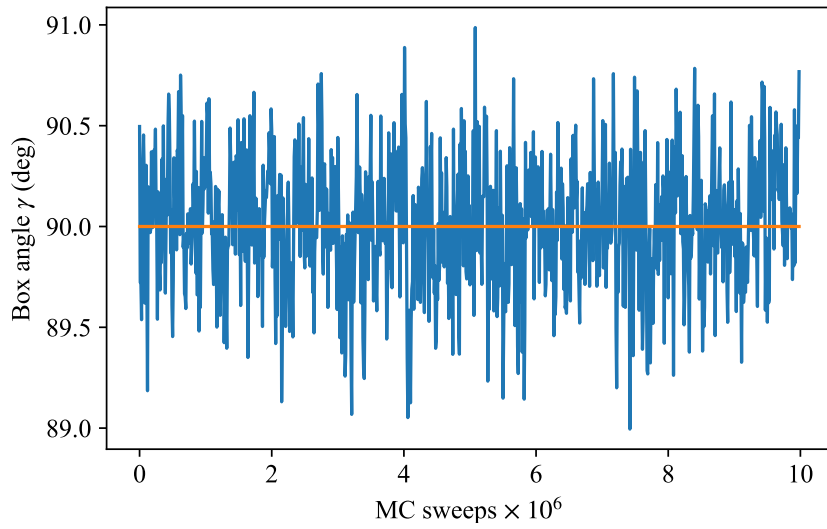
Figure 3.1: The angle between the two vectors defining the periodic boundary conditions in an NPT simulation of hard squares. 32^2 squares were equilibrated with "floppy" box boundary conditions at $\beta P = 200$, corresponding to a density of $\phi = 0.971$, well into the chiral phase. The two box vectors were allowed to independently fluctuate, and trial moves for each vector were proposed once every sweep. The angle γ between the two box vectors over 10^7 sweeps is $90.0° \pm 0.3°$; the box maintains an equilibrium square shape even in the chiral phase.
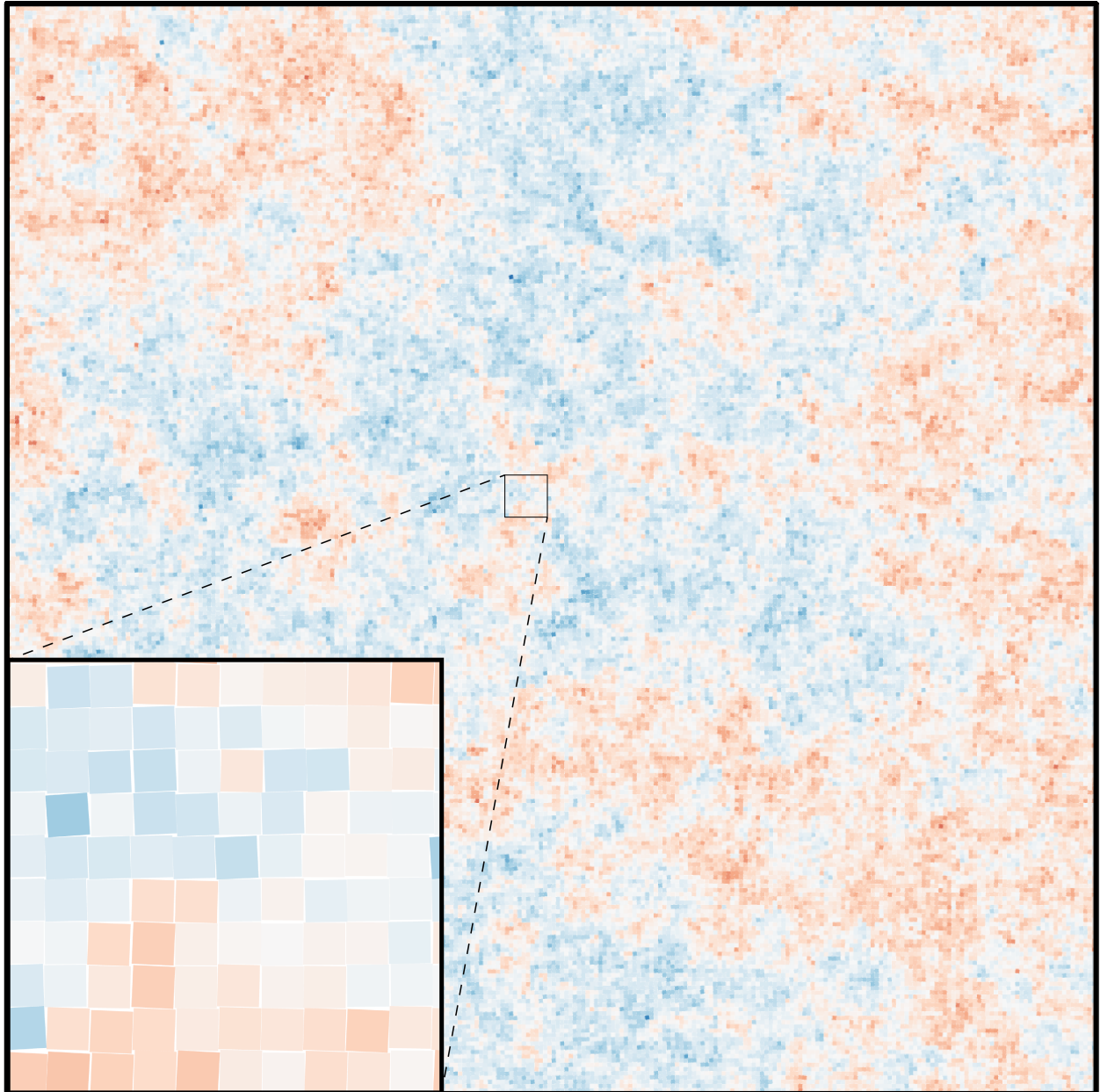
Figure 3.2: Snapshot of 256^2 hard squares at $\phi = 0.954$, very near the critical point determined to be $\phi = 0.9537$. Red particles have chiral angles tilted to the clockwise and blue particles have chiral angles tilted counterclockwise. Large critical fluctuations span the system, and chiral and achiral phases do not coexist separately; this chiral transition is continuous.
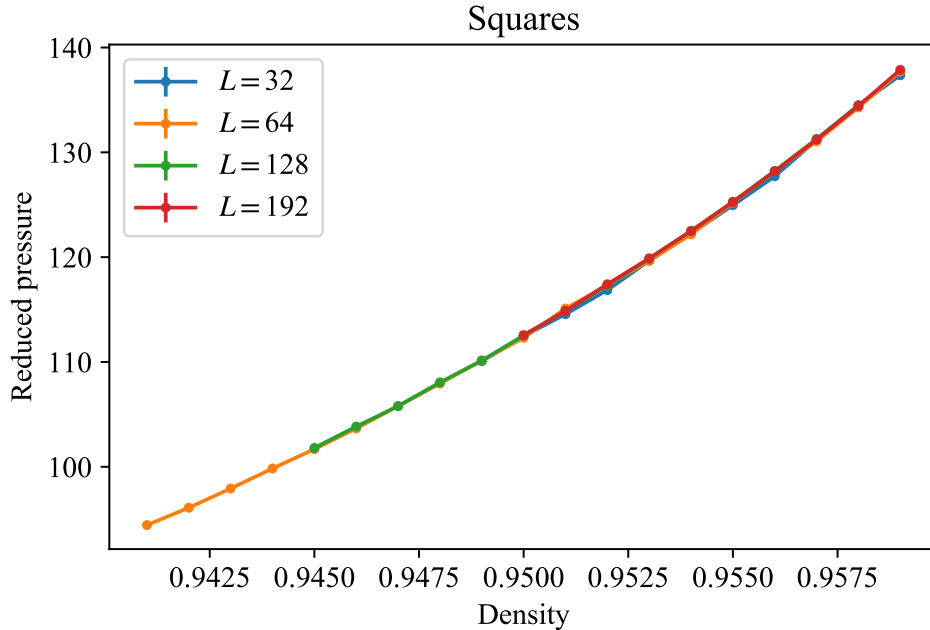
Figure 3.3: Equation of state for hard squares at several system sizes. Each system is composed of L^2 squares in a square lattice. All system sizes show the same equation of state. 1-σ error bars are smaller than the plot markers.

3.3.1 Equation of state

Typically, phase transitions are easy to identify from the equation of state, the relationship between pressure and volume (here for hard particle systems, packing fraction is a more convenient variable). In first order transitions (discontinuous transitions), as pressure is changed, the volume jumps discontinuously by some ΔV, so in the equation of state, the transition is characterized by a discontinuity. For continuous transitions, there is no jump in the volume, and it remains continuous as pressure is changed.

The equations of state for squares and triangles are taken from simulation and shown in Figures 3.3 and 3.4. Both curves show no signature of a first order phase transition, and it is difficult to discern if there is a small inflection point, which is a common feature in continuous transitions. This is unsurprising considering that there is very little structural change between the achiral and chiral phases. This apparent lack of an inflection point will be explored in Section 3.5.
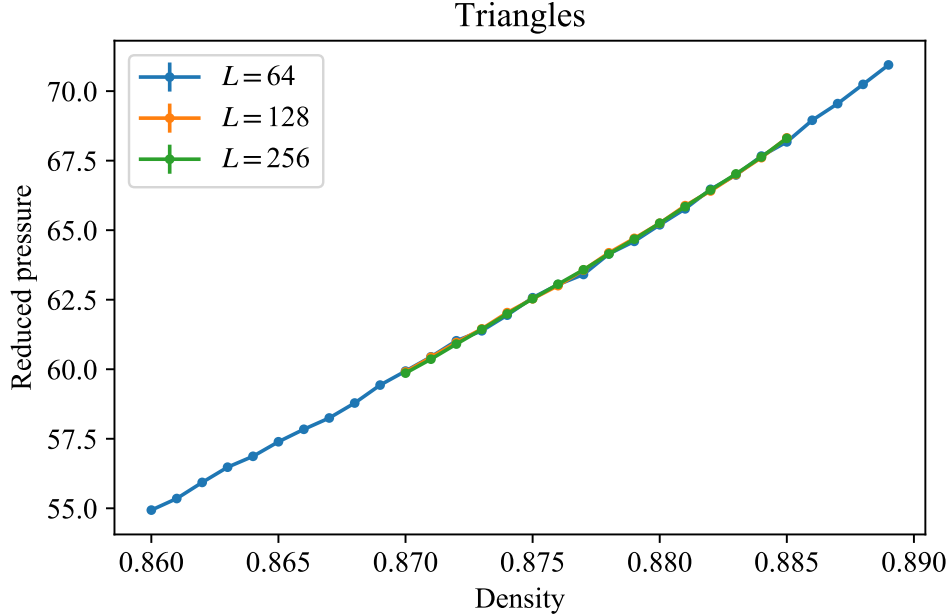
Figure 3.4: Equation of state for hard triangles at several system sizes. Each system is composed of $2L^2$ triangles in a honeycomb lattice. All system sizes show the same equation of state. 1-σ error bars are smaller than the plot markers.

3.3.2   Moments of the chiral order parameter

As explained in Section 3.2, the moments of the order parameter θ are useful in identifying the chiral phase transition. In Figure 3.5, I plot the absolute value of the order parameter $\langle|\theta|\rangle_L$. In the insets of Figure 3.6 are the Binder cumulant $U(t, L)$ and the second moment $M_2(t, L)$. The fourth moment $M_4(t, L)$ in principle does not provide more information than the second moment, but for completeness is shown in Figure 3.7.

Figure 3.5 shows the absolute value of the order parameter $\langle|\theta|\rangle_L$ as a function of density for different system sizes. The order parameter $\langle\theta\rangle_L$ is problematic in finite system sizes, because, while it is well-behaved in the achiral phase, it jumps from positive to negative abruptly in the chiral phase. The transition breaks the chiral symmetry, and both $+\theta$ and $-\theta$ are equally probable global configurations for the order parameter. In the thermodynamic limit, a system undergoing this symmetry breaking chooses one or the other, as the energy barrier to switch is $\mathcal{O}(N)$. In finite systems, however, these jumps are observable over long enough observation times, though they become less frequent for larger system sizes. The
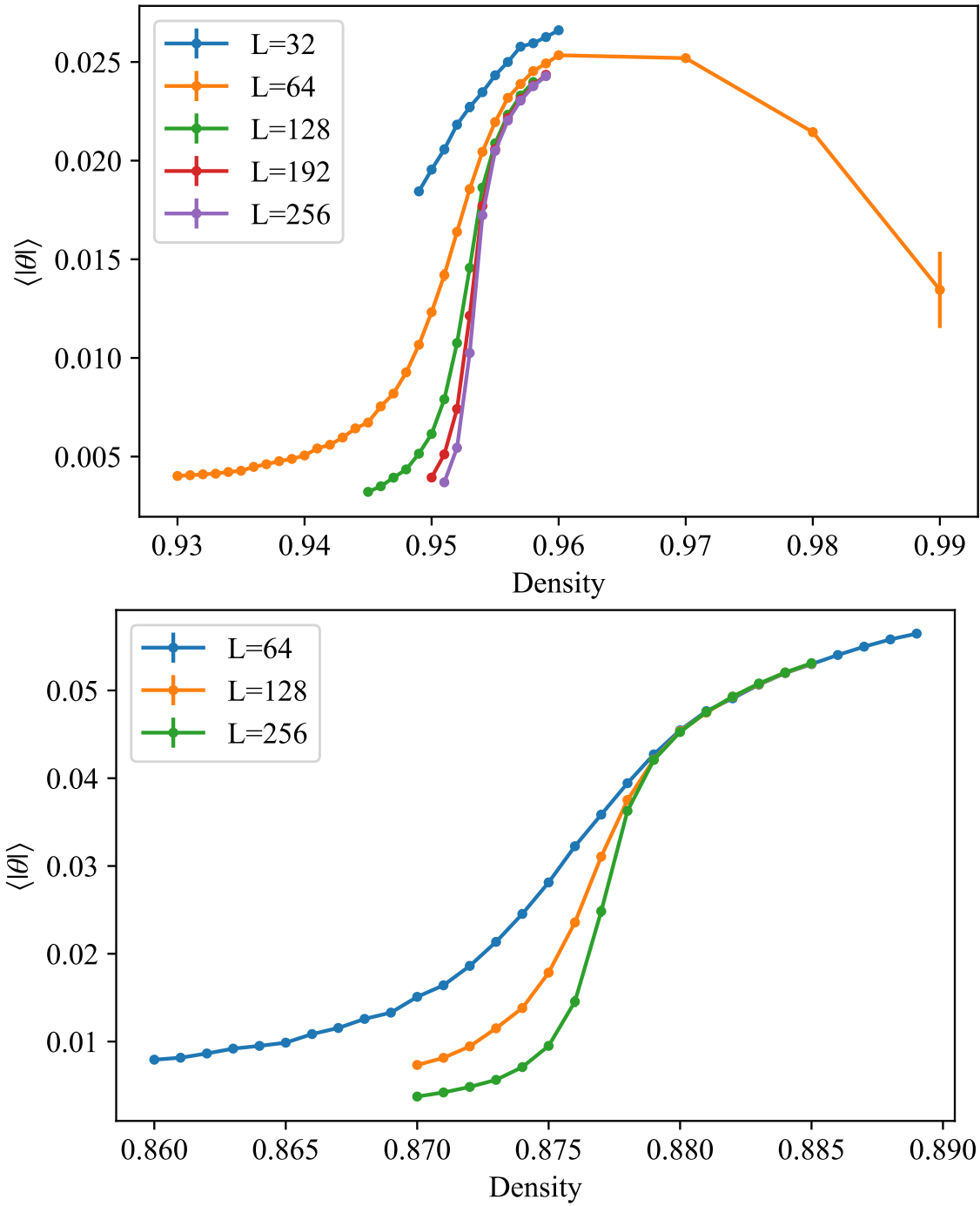
Figure 3.5: Absolute value of the order parameter $\langle|\theta|\rangle_L$ for squares (top) and triangles (bottom).
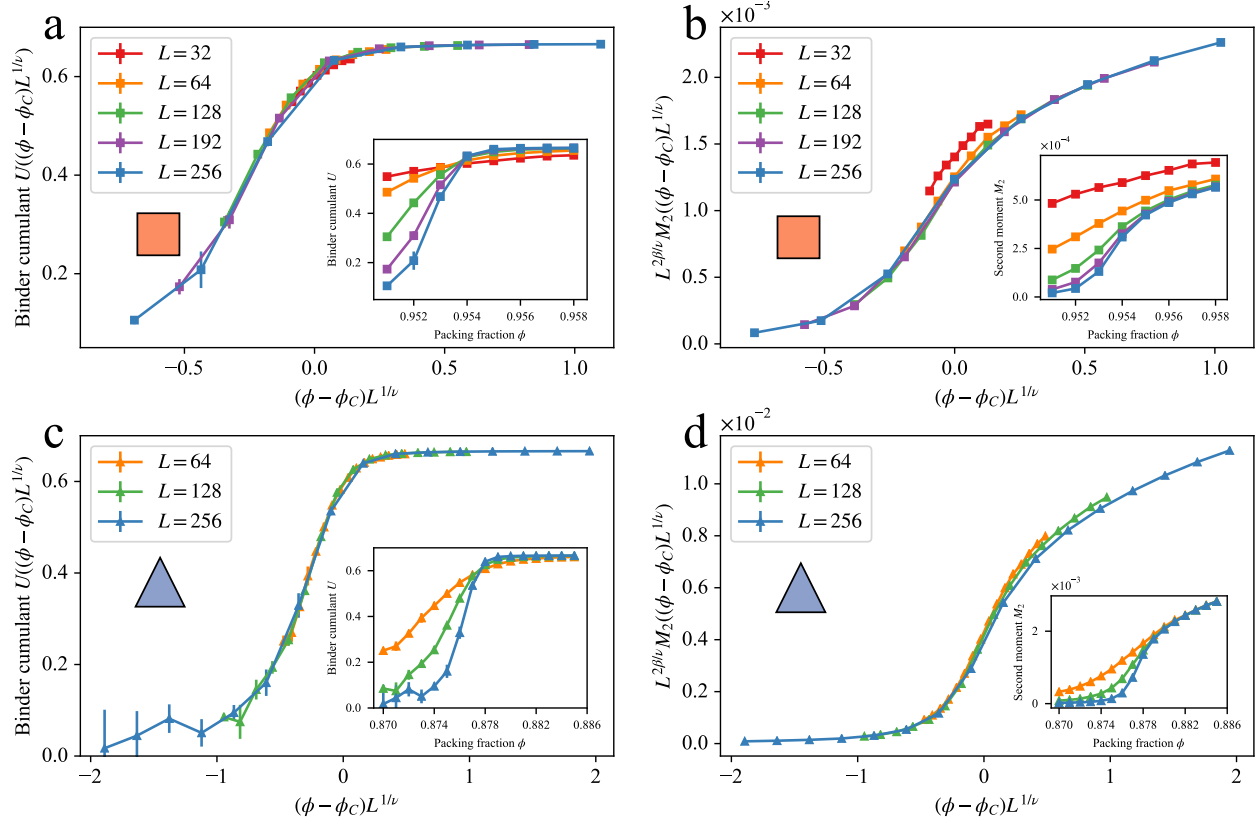
Figure 3.6: Binder cumulants (insets) and collapses (main figure) for squares (a) and triangles (c) and second moments of the order paramter (insets) and collapses (main figure) for squares (b) and triangles (d). The point of intersection of all curves in the insets of (a) and (c) identifies the critical density.

quantity $\langle |\theta| \rangle_L \to \langle \theta \rangle_L$ as $L \to \infty$.

The insets of Figure 3.6(a,c) show the Binder cumulant for squares and triangles at each L; the cumulants are calculated as ratios of the second and fourth moments shown in the inset of Figure 3.6(b,d) and 3.7 respectively. The point of mutual intersection of the Binder cumulants for each system size indicates the phase transition point. For squares, the system size $L = 32$ turns out to be too small to be used to collapse the curves; in the remaining analysis, this size is presented but not used to analyze the critical point.
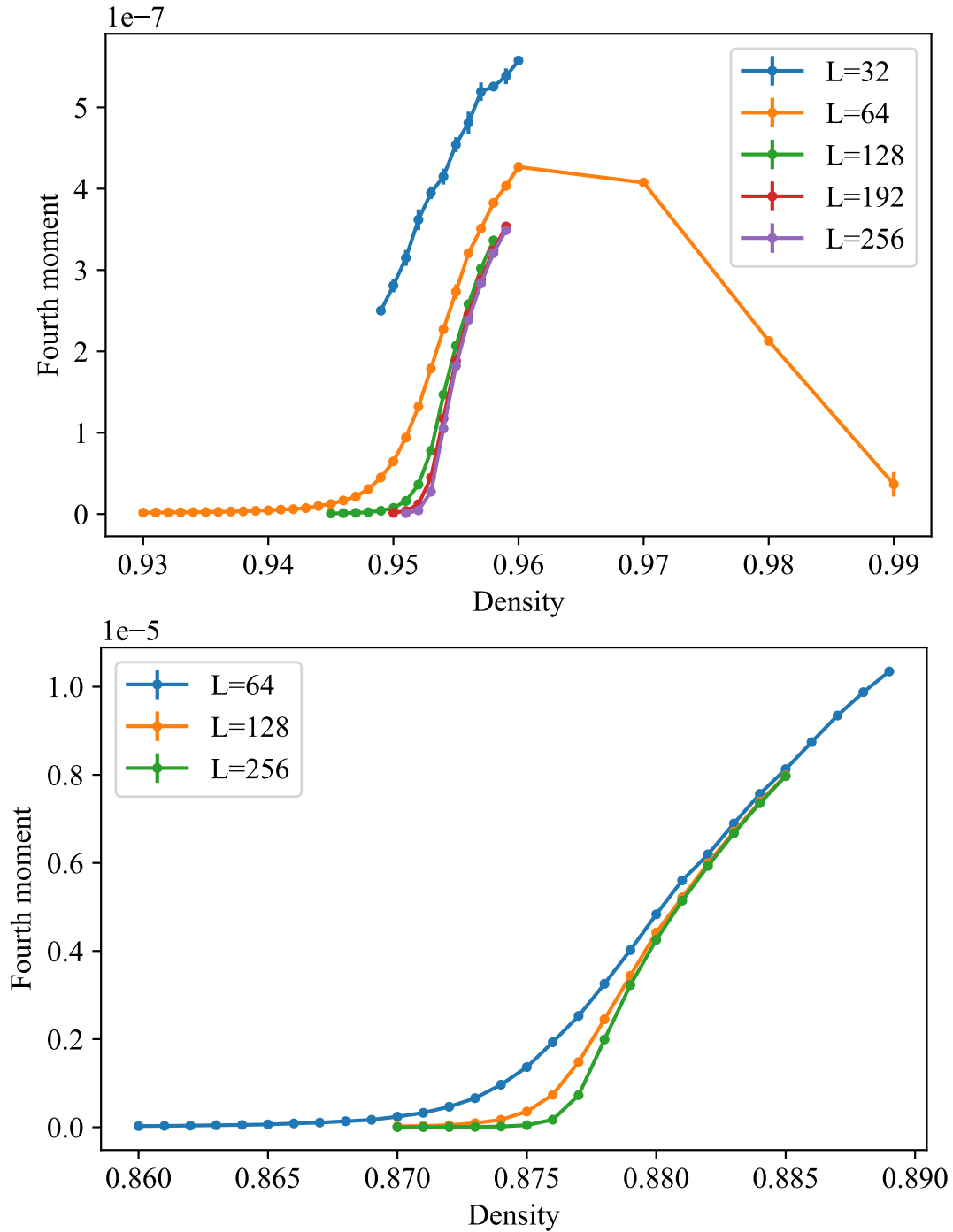
Figure 3.7: Fourth moment of the order parameter $\langle\theta^4\rangle$ for squares (top) and triangles (bottom).

3.4 Characterizing the chiral transition

In this section, I present the data collapses of the Binder cumulant, the second moment, and, for completeness, the fourth moment of the order parameter. These collapses provide sufficient precision to identify that the critical exponents ν and β are consistent with those of the 2D Ising model.

A plot of the collapse of the Binder cumulant $U(L,t)$ is shown in Figure 3.6(a,c). The second moment $M_2(t,L)$ and the fourth moment $M_4(t,L)$ are collapsed in Figure 3.6(b,d) and Figure 3.8. Each collapse is shown using the critical density ϕ_C taken from the intersection of the Binder cumulants and using the values of ν and β from the exact solution to the 2D Ising model.

3.4.1 Critical density and exponents

Figures 3.6 and 3.8 show collapses using the Ising exponents, which visually corroborate the consistency of this phase transition with the Ising universality class. To quantify the exponents, I used the python package `pyfssa` [63, 76]. To perform a collapse of, for example, the second moment, this package first calculates the mean universal curve $\bar{f}(x)$ from the set of all scaled curves $\{f_2(tL_1^{1/\nu}), f_2(tL_2^{1/\nu}) \ldots f_2(tL_j^{1/\nu})\}$ for a set of j system sizes. The sum of the square deviations from $\bar{f}(x)$ for each L is minimized with respect to ϕ_C, ν, and β; this computation is outlined in more detail in the appendix of reference [49]. The minimization process produces the mean scaling form $\bar{f}(x)$, critical exponents β and ν, the critical density ϕ_C, and standard errors on these quantities. The exponents and critical densities obtained from these collapses are shown in Table 3.1.

The critical density for squares is between 0.9537 and 0.9540, and all three collapses for the triangles yield a critical density of 0.8774. All the collapses esimate ν to be slightly under 1, but with relatively large error bars of ± 0.1, this estimate is consistent with the exact Ising exponent. Larger systems could be used to pinpoint ν with further accuracy, though I would not expect the estimate for ν to vary significantly from 1 even if more costly simulations
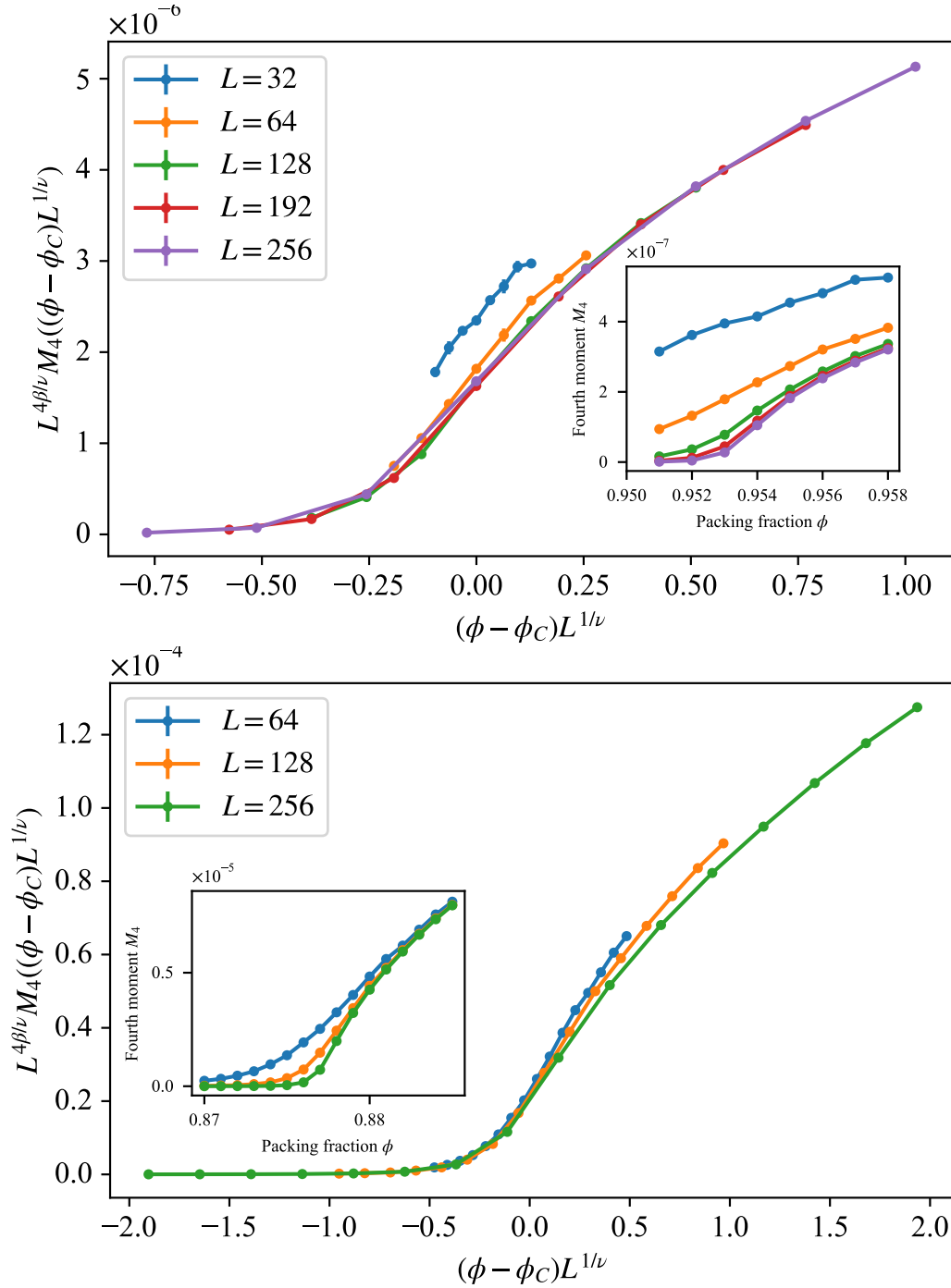
Figure 3.8: Fourth moment collapses for squares (top) and triangles (bottom) using Ising exponents. Critical densities are 0.9540 and 0.8447 respectively.

	Binder cumulant		2ⁿᵈ moment		4ᵗʰ moment	
	□	△	□	△	□	△
ϕ_C	0.9537(2)	0.8774(2)	0.95400(4)	0.8774(1)	0.9540(3)	0.8774(2)
ν	0.91(9)	0.95(10)	1.00(4)	0.98(4)	1.0(1)	1.0(1)
β			0.13(2)	0.149(6)	0.13(3)	0.15(1)

Table 3.1: Critical exponents calculated from various data collapses for each shape.

were run. Estimates for β from the squares are consistent with those of the Ising model, $1/8 = 0.125$, though the triangles overestimate this exponent by about 20%.

3.5 Mapping the entropy through the transition

In the context of hard particle solids, it is natural to ask what happens to the entropy as the system transits from the achiral to the chiral state. Using the methods of Chapter II, we can decompose the total system entropy mode by mode. Figure 3.9 shows the dispersion relation for 128^2 hard squares for a range of densities that spans the chiral transition. The dispersion relations change very little in form, except that all of the frequencies increase with density. For all tested densities, the libron frequencies are all much larger than those of the phonons.

The rotational and translational free energy can be computed from the dispersion relations with Equation 2.7 from Section 2.2. This free energy is shown in Figure 3.10 partitioned by rotation and translation. There is no signature of the chiral phase transition at $\phi = 0.9537$, just as there is no signature in the equation of state (Figures 3.3 and 3.4). The continuous phase transition would manifest itself as an inflection point in the free energy, or equivalently, a kink in the first derivative of the free energy, the pressure. The inset of Figure 3.11 shows the pressure calculated from the free energy of the harmonic modes along with the pressure calculated directly from the NVT simulations. The pressure is calculated from the free energy using the simple relation $-P = \partial F/\partial A$ and $A = NA_p/\phi$, where F is the Helmholtz free energy, A is the area of the simulation box, A_p is the area of one particle
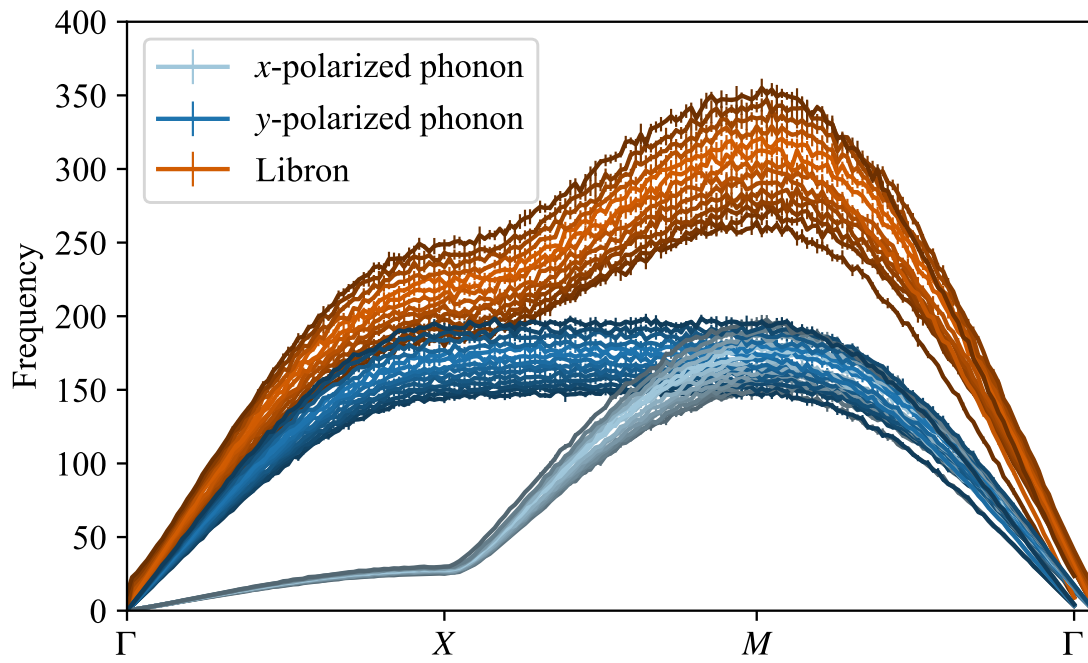
Figure 3.9: Dispersion relations for hard square solid at all densities in the range 0.945–0.958. Frequencies increase with density, and the brightness of the colors of the curves indicate closeness to the critical density $\phi_C = 0.9537$. The bottom axis is a walk through the high symmetry points of the square-shape Brillouin zone, with $\Gamma = (0, 0)$, $X = (0, \pi/a)$, and $M = (\pi/a, \pi/a)$, with a the lattice spacing.

(set to $A_p = 0.5$), ϕ is the packing fraction, and N is the particle number. There is a small discrepancy between the two pressures, likely because the free energy of the system is not fully captured by the simple harmonic approximation, which is expected near the critical point.

Because rotational and translational modes are decoupled at harmonic order, they contribute separately to the free energy and thus the pressure. The main figure of Figure 3.11 shows the *partial* pressures of rotational and translational modes. Upon transiting to the chiral state, rotational modes stiffen and contribute more partial pressure, whereas rotational modes soften and their corresponding partial pressure decreases. A similar transition, the isotropic-nematic transition of hard rods first investigated by Onsager [68], is caused by an interchange of rotational entropy for translational entropy; we find a similar picture for this chiral transition. In the same sense that hard rods sacrifice their rotational entropy for translational entropy in transiting to the nematic phase, hard squares and triangles sacrifice translational entropy for rotational entropy when transiting to the chiral phase.

Still, the microscopic mechanism for the transition is not determined. That the chiral transition exhibits Ising-like features suggests the microscopic mechanism responsible for the transition is similar; there is a driving force that becomes stronger as density is increased that favors the ordered (chiral) state over the disordered (achiral) state. At any given density, particles in the chiral state have their facets closer together and their vertices farther apart than in the achiral state. It is already known that hard particles self-assemble *via* facet alignment; large facets play the role of effective entropic attractive patches whereas vertices are sources of effective entropic repulsion [27, 81]. As density increases, the vertices become more repulsive, eventually inducing the chiral transition to force them apart. That this transition happens at around $\phi = 0.88$ for triangles and slightly higher at $\phi = 0.95$ for squares is likely because the triangles' vertices are much sharper, and six vertices meet at a point rather than four for squares. Furthermore, this type of lattice-preserving chiral transition is completely suppressed by a slight amount of corner rounding, provided the
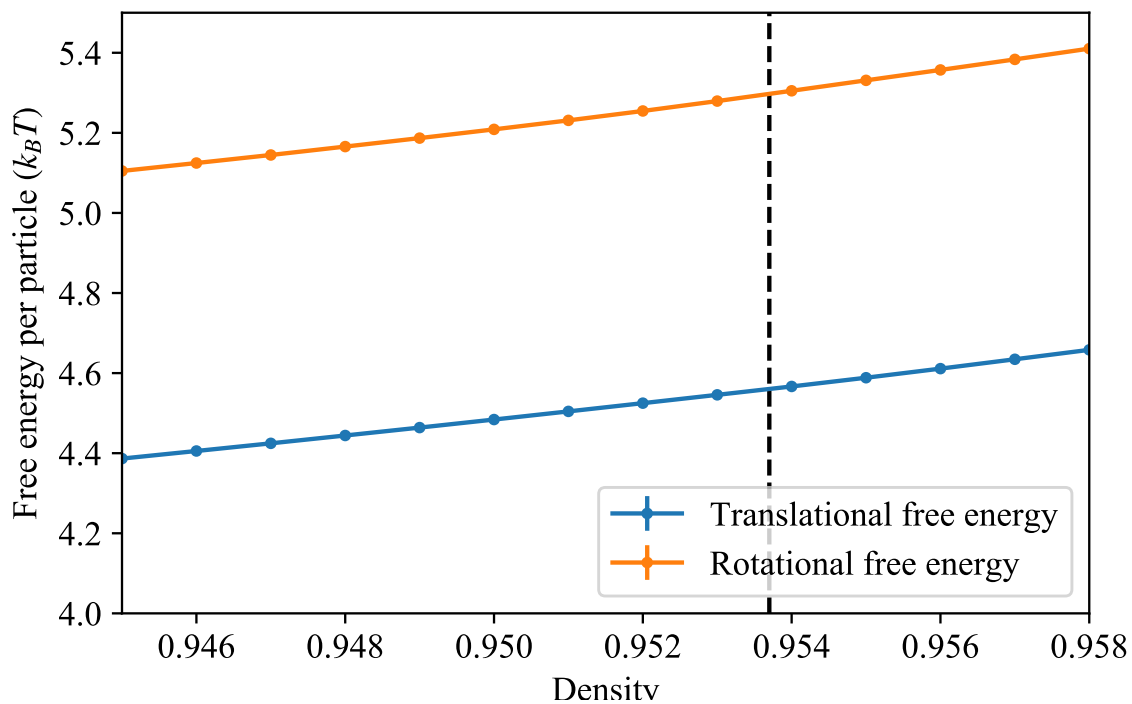
Figure 3.10: Free energy per particle partitioned by mode. The translational free energy is divided by a factor of 2 to account for the two polarizations of the phonons. There is little indication that a phase transition occurs at $\phi = 0.9537$. Dashed line indicates the critical density. 1-σ error bars are smaller than the plot markers.
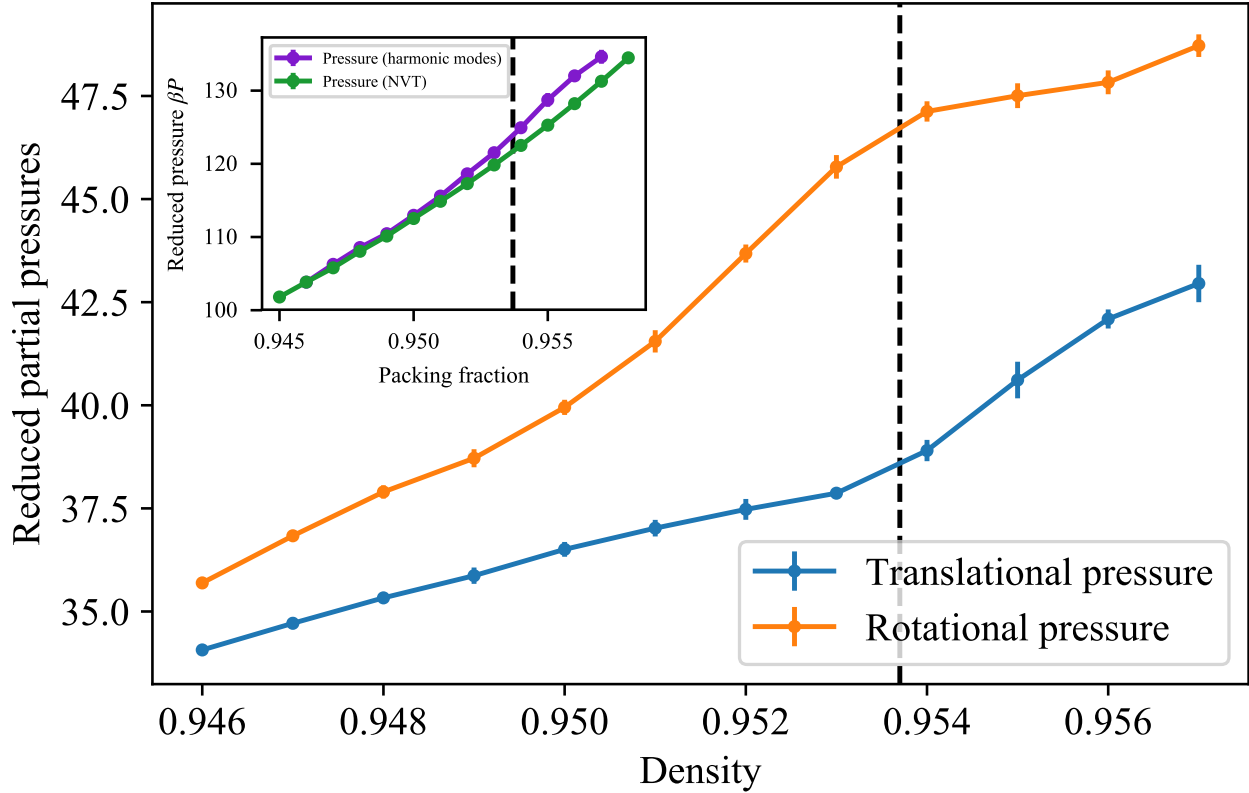
Figure 3.11: Partial pressures from rotational (orange) and translational (blue) modes. Translational pressure is shown divided by a factor of 2 to account for the two polarizations of phonons. Error bars signify 1-σ uncertainty. Dotted line signifies the chiral transition density. Inset: total reduced pressure calculated from sum over contributions from harmonic modes (purple) and from the pressure calculated by the SDF method over the course of the NVT simulations. 1-σ error bars are smaller than the marker size. No easily discernible kink in the pressure is seen. The chiral transition results in a very subtle structural change and does not affect the total system pressure much at all, but the individual partial pressures show clear kinks, demonstrating a tradeoff of pressure.
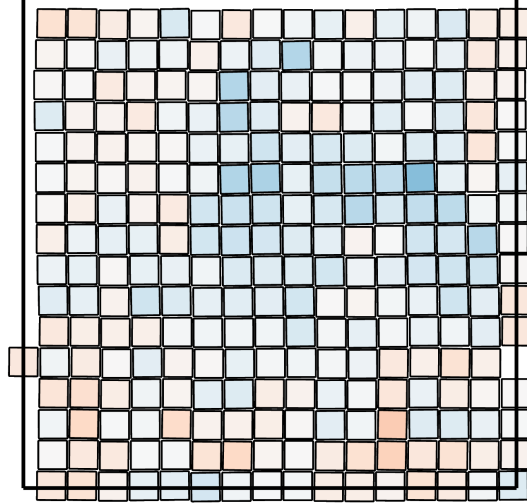
Figure 3.12: Snapshot at $\phi = 0.98$ of rounded squares with rounding radius $r = 0.05$. Colors indicate orientation away from the achiral state; red is counterclockwise and blue is clockwise. No chiral symmetry breaking is seen for the rounded squares.

lattice is preserved by fixed commensurate boundary conditions, rather than in the work of Carmichael and Shell [17]. In Figure 3.12, I present a snapshot of a simulation (NVT with $N = 64^2$) with a small amount of particle rounding at $\phi = 0.98$. The curvature of the corners of the rounded squares is defined by a rounding radius of $r = 0.05$, compared to the particle circumradius of 0.5. That this small rounding effect suppresses the chiral transition completely suggests that effective entropic vertex repulsion is the microscopic cause of this transition. This picture of corner repulsion is consistent with the findings of Zhao and Mason [90] in the context of densely-packed square cross-shaped particles. They showed that the phase behavior is governed by the effective excluded volume swept out by the arms of the crosses averaged over particle orientations—the authors term the effective excluded volume a "crossoid." The effective excluded volume of the cross arms plays the same role as effective vertex repulsion, leading to the same close-packed chiral square lattice at high densities. Further work could be done to sweep across multiple rounding radii; at some radius even smaller than that tested here, the system must recover the chiral transition.

I have demonstrated that regular hard squares undergo a lattice-preserving chiral symmetry breaking transition. I have shown this transition, also exhibited by regular triangles,

falls in the 2D Ising universality class. This transition is driven by an increase in rotational entropy at the expense of a loss in translational entropy.

CHAPTER IV

Characteristic features of photonic band gaps in 3D

4.1 Introduction

My work is a part of a larger collaboration with Rose Cersonsky and Bradley Dice to understand the common structural features of photonic band gap materials [18]. My part in this large project was to examine the configuration of the magnetic and electric fields in detail for a small number of representative structures. In Section 4.2, I provide the necessary theoretical background to understand the electromagnetic problem with Maxwell's equations. In Section 4.3, I explain the computational methods of producing band structures and detail how structural data was gathered and used. In Section 4.4, I motivate and explain my approach to analyze the fields in structures with band gaps.

4.2 Theoretical background

The problem of finding materials with photonic band gaps begins with Maxwell's equations; first I show that Maxwell's equations in macroscopic linear dielectric media can be reduced to an eigenvalue problem. This eigenvalue problem cannot be solved exactly for a general distribution of dielectric material, but it can be greatly simplified for periodic media. Much of this discussion follows Joannopoulos [50].

4.2.1 Maxwell's equations in periodic media and photonic crystals

The band structure of a photonic material is determined by Maxwell's equations. For materials specified by a permittivity function $\varepsilon_0\varepsilon(\mathbf{r})$ (neglecting materials composed of, for example, metals or dielectrics with frequency dependent permittivity), the Maxwell's equations in macroscopic media are,

$$\nabla \times \mathbf{H} = \frac{\partial \mathbf{D}}{\partial t} \qquad \nabla \times \mathbf{E} = -\frac{\partial \mathbf{B}}{\partial t} \tag{4.1}$$

$$\nabla \cdot \mathbf{B} = 0 \qquad \nabla \cdot \mathbf{D} = 0, \tag{4.2}$$

and the constitutive relations are,

$$\mathbf{D} = \varepsilon_0\varepsilon(\mathbf{r})\mathbf{E} \qquad \mathbf{B} = \mu_0\mathbf{H}. \tag{4.3}$$

A few assumptions are implied in this formulation of Maxwell's equations. First, the dielectric medium defined by the dielectric function $\varepsilon(\mathbf{r})$ is linear and frequency independent, so the constitutive relation $\mathbf{D} = \varepsilon_0\varepsilon(\mathbf{r})\mathbf{E}$ does not involve higher powers of $\mathbf{E}$ or time derivatives of $\mathbf{E}$. Second, the magnetic permeability of the dielectric material is assumed to be equal to the vacuum permeability μ_0, which is a good approximation for most dielectrics used in photonic applications. Third, we are interested in the band structure of a dielectric material, so there is no free charge or current.

With the above assumptions, the Maxwell's equations and constitutive relations can be combined into an eigenvalue equation for the magnetic field $\mathbf{H}$,

$$\nabla \times \frac{1}{\varepsilon(\mathbf{r})}\nabla \times \mathbf{H}(\mathbf{r}, t) = -\varepsilon_0\mu_0\frac{\partial^2 \mathbf{H}}{\partial t^2}. \tag{4.4}$$

Assuming time harmonic fields, $\mathbf{H}(\mathbf{r}, t) = e^{-i\omega t}\mathbf{H}(\mathbf{r})$, and using the relationship $\varepsilon_0\mu_0 = 1/c^2$

with c the speed of light,

$$\nabla \times \frac{1}{\varepsilon(\mathbf{r})} \nabla \times \mathbf{H}(\mathbf{r}) = \left(\frac{\omega}{c}\right)^2 \mathbf{H}(\mathbf{r}). \tag{4.5}$$

$$\nabla \cdot \mathbf{H}(\mathbf{r}) = 0. \tag{4.6}$$

The operator on the left-hand side can be written succinctly as Θ,

$$\Theta \mathbf{H}(\mathbf{r}) = \left(\frac{\omega}{c}\right)^2 \mathbf{H}(\mathbf{r}). $$

$$\Theta = \nabla \times \frac{1}{\varepsilon(\mathbf{r})} \nabla \times . \tag{4.7}$$

Equivalent eigenvalue equations can be derived for the other fields $\mathbf{E}(\mathbf{r})$ and $\mathbf{D}(\mathbf{r})$:

$$\frac{1}{\varepsilon(\mathbf{r})} \nabla \times \nabla \times \mathbf{E}(\mathbf{r}) = \left(\frac{\omega}{c}\right)^2 \mathbf{E}(\mathbf{r}). \tag{4.8}$$

$$\nabla \times \nabla \times \frac{1}{\varepsilon(\mathbf{r})} \mathbf{D}(\mathbf{r}) = \left(\frac{\omega}{c}\right)^2 \mathbf{D}(\mathbf{r}). \tag{4.9}$$

In periodic media, where $\varepsilon(\mathbf{r}) = \varepsilon(\mathbf{r}+\mathbf{R})$ with $\mathbf{R}$ a lattice vector, the eigenfunctions $\mathbf{H}(\mathbf{r})$ obey Bloch's theorem:

$$\mathbf{H}(\mathbf{r}) = \mathbf{u}(\mathbf{r})e^{i\mathbf{k}\cdot\mathbf{r}}, \qquad \mathbf{u}(\mathbf{r} + \mathbf{R}) = \mathbf{u}(\mathbf{r}). \tag{4.10}$$

$\mathbf{R}$ is again any real space lattice vector of the periodic medium, and $\mathbf{k}$ is any wavevector that lives in the first Brillouin zone of the reciprocal lattice.

The eigenmodes $\mathbf{H_k}(\mathbf{r})$ are found by then solving the eigenvalue problem

$$(\nabla + i\mathbf{k}) \times \frac{1}{\varepsilon(\mathbf{r})}(\nabla + i\mathbf{k}) \times \mathbf{u_k}(\mathbf{r}) = \left(\frac{\omega}{c}\right)^2 \mathbf{u_k}(\mathbf{r}). \tag{4.11}$$

$$(\nabla + i\mathbf{k}) \cdot \mathbf{u_k}(\mathbf{r}) = 0. \tag{4.12}$$

There are an infinite number of solutions for each value of **k**, and each solution sits in a *band*, numbered n, that varies across the Brillouin zone as **k** is varied. In practice, we calculate only the first 20 or 30 bands. The eigenequation for $\mathbf{H_k(r)}$ is Hermitian, and the solutions $\mathbf{H_{k,n}(r)}$ are orthogonal to each other with respect to the inner product,

$$(\mathbf{H_{k,m}(r)}, \mathbf{H_{k,n}(r)}) = \int_V d^3r \ \mathbf{H^*_{k,m}(r) \cdot H_{k,n}(r)} = \delta_{mn}. \qquad (4.13)$$

Here, the volume V is the volume of the unit cell, and the units and amplitude of **H** have been chosen such that the inner product $(\mathbf{H_{k,n}}, \mathbf{H_{k,n}}) = 1$. The eigenfrequency of a mode $\mathbf{H_{k,n}}$ can be calculated in terms of this inner product. By dotting each side of the Equation 4.6 with $\mathbf{H^*_{k,n}(r)}$ and integrating over the unit cell:

$$\int_V d^3r \ \mathbf{H^*_{k,n}} \cdot \nabla \times \frac{1}{\varepsilon(\mathbf{r})} \nabla \times \mathbf{H_{k,n}} = \frac{\omega^2}{c^2} \int_V d^3r \ \mathbf{H^*_{k,n}} \cdot \mathbf{H_{k,n}}.$$

$$\frac{(\Theta \mathbf{H_{k,n}}, \mathbf{H_{k,n}})}{(\mathbf{H_{k,n}}, \mathbf{H_{k,n}})} = \frac{\omega^2}{c^2}. \qquad (4.14)$$

The frequency bands in any material can generally intersect, and at a given frequency ω, there are a number of different **k** and n for which the frequency of $\mathbf{H_{k,n}}$ is ω. However, structures with a *photonic band gap* exhibit a range of frequency $\Delta\omega$ for which no eigenmode has a frequency within the gap. To find a band gap, it is necessary to calculate the band structure over all of the first Brillouin zone and for sufficiently many bands. It is useful to note that the Maxwell eigenproblem, Equation 4.6, scales simply with the length scale of the dielectric structure; increasing each lattice constant by a factor of a scales the wavevectors **k** and the frequencies by a factor of $1/a$. For this reason, it is useful to describe photonic band gaps nondimensionally as $\Delta\omega^* = \Delta\omega/\omega_{\text{mid}}$, where ω_{mid} is the frequency at the center of the gap.

The band structure, and thus the presence and size of a band gap (or multiple gaps), is

highly dependent on the magnitude of $\varepsilon(\mathbf{r})$ and the symmetry group of the crystal. The theory of the relationship between the crystal space group and the band structure is summarized briefly in Appendix C.

4.3   Methods

4.3.1   Numerical methods

In practice, the eigenproblem Equation 4.12 is solved numerically with an iterative plane-wave expansion using MIT Photonic Bands (MPB) [51]. A trial mode $\mathbf{H}(\mathbf{r})$ is expanded as a sum of plane waves $\mathbf{v_K}e^{i\mathbf{K}\cdot\mathbf{r}}$ where $\mathbf{K}$ is a reciprocal lattice vector, and each individual plane wave satisfies the transversality constraint on the magnetic field, $\nabla \cdot \mathbf{v_K}e^{i\mathbf{K}\cdot\mathbf{r}} = 0$. Any trial mode $\mathbf{H_k}$ is necessarily a linear combination of the eigenmodes $\alpha_1\mathbf{H_{k,1}}+\alpha_2\mathbf{H_{k,2}}+\alpha_3\mathbf{H_{k,3}}+\ldots$. Therefore, the inner product of the trial function satisfies:

$$\frac{(\Theta\mathbf{H_k}, \mathbf{H_k})}{(\mathbf{H_k}, \mathbf{H_k})} = \frac{\omega^2}{c^2} \geq \frac{\omega_1^2}{c^2}. \tag{4.15}$$

MPB then finds the first eigenvalue ω_1 by minimizing ω with respect to the plane-wave coefficients of the trial function $\mathbf{H_k}$. This minimization process furnishes the first eigenmode $\mathbf{H_{k,1}}$. MPB then produces another trial function; the frequency of this new trial function is minimized—subject to the constraint that the trial function is orthogonal to the first eigenmode $\mathbf{H_{k,1}}$—to provide the next eigenfrequency ω_2 and the next eigenmode $\mathbf{H_{k,2}}$. This procedure is continued until N eigenmodes are found; typically N is 20 or 30.

The fields $\mathbf{E}$, $\mathbf{D}$ and $\mathbf{B}$ can be obtained from $\mathbf{H}$ using Maxwell's equations and the constitutive relations, Equations 4.2 and 4.3.

4.3.2   Data production and selection

A data set of 1355 unique structures were compiled from real atomic structures from the Crystallographic Open Database (COD) [40] and the Inorganic Crystal Structure Database

(ICSD) [42]. These structures cover all Bravais lattices, span 227 of the 230 space groups, and are comprised of unit cells with between 1 and 784 particles.

For each structure, each atom is replaced with a sphere of radius r and dielectric constant ε. Overlaps between spheres are allowed for when $2r$ is greater than the nearest neighbor distance; these configurations lead to *connected* dielectric space. The sphere radius r is swept over a range from 0 to $r_{\max}$, where $r_{\max}$ is a structure-dependent radius beyond which the entire unit cell is homogeneously filled with dielectric; between 20 and 100 different radii are chosen in this range depending on the structure. This procedure generates a "direct" structure; additionally, "inverse" structures are constructed, where the spheres are filled with air and the dielectric constant of the surrounding medium is set to ε.

The dielectric constant ε is chosen to be 16, in parallel with previous computational studies of theoretical photonic materials [80, 30, 14, 21]; if a structure at some radius is found to have a band gap when $\varepsilon = 16$, ε is reduced until that gap disappears. Generally, it is unlikely that a structure that does not exhibit a gap at $\varepsilon = 16$ would exhibit one with $\varepsilon < 16$. This procedure of data generation produces a rich space of around 150,000 unique materials; the band structure and eigenmodes are solved for with MPB. Of the 2710 structures (counting both direct and inverse structures), 351 yield a band gap greater than 0.1% at some dielectric filling fraction and dielectric constant, shown in Figure 4.1. For each of these structures with band gaps, a "band atlas" is constructed; a diagram of the band gaps $\Delta\omega^*$ as a function of filling fraction ϕ.

Additionally, four structures, face-centered cubic, body-centered cubic, simple cubic, and diamond cubic, are modified to systematically explore the role of dielectric connectivity in the creation of a photonic band gap. For each of these structures, dielectric spheres of radius r are placed at the lattice sites, then m additional spheres of radius r along the lines joining nearest neighbors. As m increases, these interpolating spheres better approximate rod connections, a structure morphology often studied to achieve good band gaps [69, 47, 58]. For small m and large r, the dielectric can be connected but be comprised of large spheres with small

channels connecting each other. For large m and small r, the dielectric is connected but the channel width is approximately uniform; the "rods" connecting lattice sites are less lumpy than for small m. These parameters provide direct control over the degree of connectivity of the dielectric space comprising the crystal. Figures 4.1c,d shows the band atlases for these "interpolated" structures.

This large data space was used to glean general structural properties of photonic crystals in a symmetry-agnostic way, in contrast with some previous studies that restricted structures to a small subset of space groups [59].

4.4 Field analysis in two and three dimensions

The frequency of an eigenmode can be cast in terms of the displacement field using Maxwell's equations:

$$\frac{\int_V d^d r \ (\nabla \times \mathbf{D}^*) \cdot \left(\nabla \times \frac{1}{\varepsilon} \mathbf{D}\right)}{\int_V d^d r \ |\mathbf{D}|^2} = \frac{\omega^2}{c^2}. \tag{4.16}$$

Heuristically, the frequencies of eigenmodes are lower if the $\mathbf{D}$ field is confined to the higher dielectric region, and they are lower if $\mathbf{D}$ has little curl. However, it is not always geometrically possible for an eigenmode to confine its electric energy density in the high dielectric reigon while remaining orthogonal to the modes lower in frequency. The geometric analysis of field lines is the topic of this section. Meade *et al.* performed this geometric analysis in [61] for two-dimensional photonic crystals, and I present their work here as a starting point for the discussion in three dimensions.

4.4.1 Two dimensions: role of connectivity

In general, Maxwell's equations (without sources) guarantee that the electric and magnetic fields are perpendicular to each other. In two dimensions, polarizations with the magnetic field aligned in the plane of periodicity (transverse magnetic or TM) and polarizations with the electric field aligned in the plane of periodicity (transverse electric or TE)
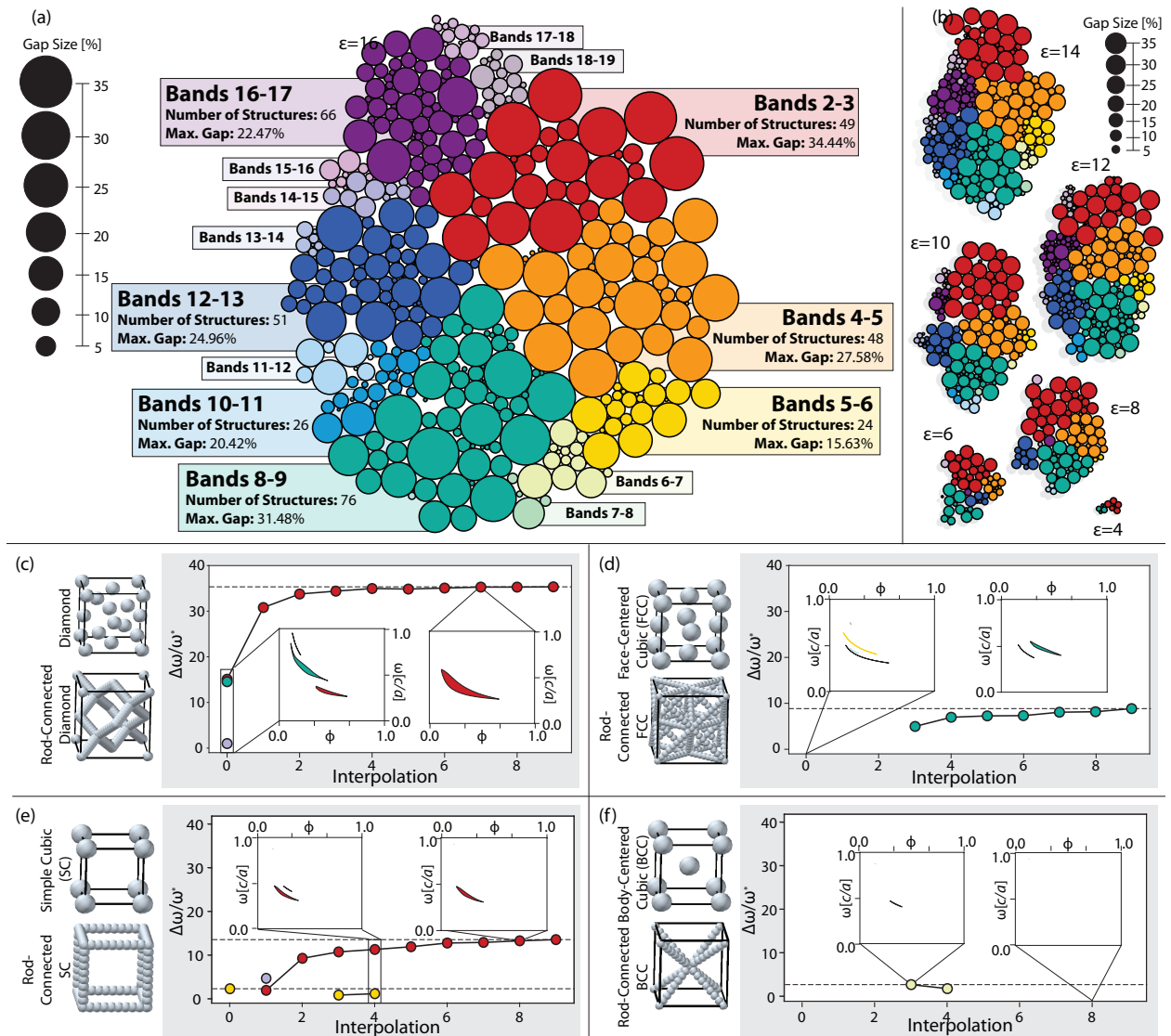
Figure 4.1: (a) Overview of the data produced at the high dielectric constant $\varepsilon = 16$. Circle areas are proportional to the band gap size; colors correspond to the location of the gap. Some structures are shown more than once, because the structure was found to exhibit band gaps in two different locations at different filling fraction. (b) Data for lower dielectric constants, with gaps found in systems with ε as low as 4. The photonic gap atlas for the structures (c) diamond cubic, (d) face-centered cubic, (e) simple cubic, and (f) body-centered cubic for different interpolations, from the original structure (shown to the left) to the rod-connected version (shown to the right), shown at consistent filling fractions. For each structure, the gap size as a function of number of interpolating spheres is shown, with insets giving the gap atlas for a single interpolation. Each atlas is plotted with the x-axis corresponding to filling fraction $\phi \in [0, 1]$ and y-axis corresponding to frequency $\omega \in [0, 1]$.

51

are decoupled from each other. If the two-dimensional crystal is uniform in the z direction, then for TM modes, the electric field is aligned along the z axis and is only a function of x and y. Likewise, for TE modes, the magnetic field is aligned along the z axis and is only a function of x and y. These symmetries greatly simplify the Maxwell eigenproblem:

$$\nabla \times \frac{1}{\varepsilon(x,y)} \nabla \times \hat{z} H_z(x,y) = \frac{\omega^2}{c^2} \hat{z} H_z(x,y), \qquad \text{(TE modes)}, \qquad (4.17)$$

$$\frac{1}{\varepsilon(x,y)} \nabla \times \nabla \times \hat{z} E_z(x,y) = \frac{\omega^2}{c^2} \hat{z} E_z(x,y), \qquad \text{(TM modes)}. \qquad (4.18)$$

These reduce to eigenvalue problems for scalar functions of two variables, x and y:

$$-\left(\partial_x \frac{1}{\varepsilon(x,y)} \partial_x + \partial_y \frac{1}{\varepsilon(x,y)} \partial_y \right) H_z(x,y) = \frac{\omega^2}{c^2} H_z(x,y), \qquad \text{(TE modes)}, \qquad (4.19)$$

$$-\frac{1}{\varepsilon(x,y)} \left(\partial_x^2 + \partial_y^2 \right) E_z(x,y) = \frac{\omega^2}{c^2} E_z(x,y), \qquad \text{(TM modes)}. \qquad (4.20)$$

Meade *et al.* studied the configurations of electric field lines in two-dimensional photonic crystals using the above eigenvalue equations for both the TM and TE polarizations [61]. The group studied two structures: cylindrical rods of dielectric arranged in a square lattice and square-shaped holes drilled through a bulk dielectric arranged in a square lattice. Figure 4.2 shows the band structure for both TE and TM modes in both structures; insets are diagrams of the lattice. Full band gaps—frequency gaps in both polarizations—are difficult to configure in only two dimensions, but Figure 4.2a shows a large gap in the TM mode and Figure 4.2b shows a large one in the TE mode separately.

Meade *et al.* show that the geometric properties of the field lines along with the constraint that modes in different bands must be orthogonal to each other sufficiently explain the frequency gaps for each structure. As shown in Figure 4.3, in the case of the cylinders, the TM mode below the gap is almost completely confined to the high dielectric medium, but the next orthogonal mode is necessarily forced out into the low dielectric air space, pushing the frequency up. However, for the TE modes shown in Figure 4.4, both field configurations

Photonic Band Structure of
Square Lattice of Dielectric Cylinders

Photonic Band Structure of
Square Lattice of Square Holes
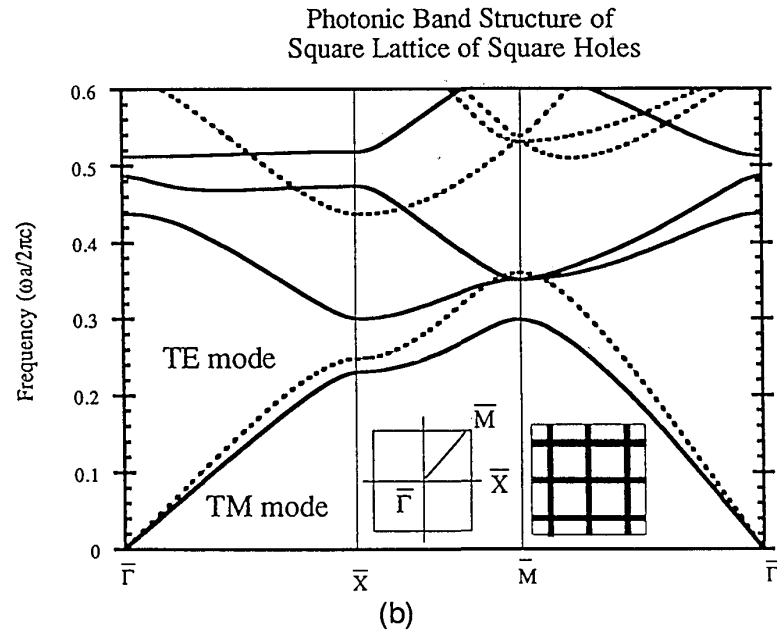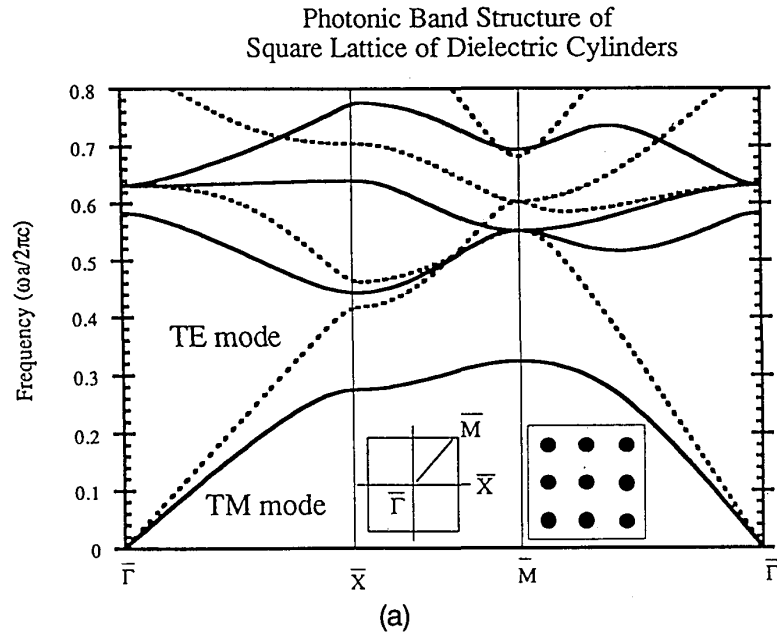
Figure 4.2: Dispersion relations for photonic crystals shown in insets. (a) is a square lattice of dielectric cylinders; (b) is a square lattice of square-shaped voids, forming square window frame-like channels of dielectric. Dielectric constants in each structure is $\varepsilon = 8.9$. Dashed lines indicate TE modes and solid lines indicate TM modes. Figure reproduced from [61].
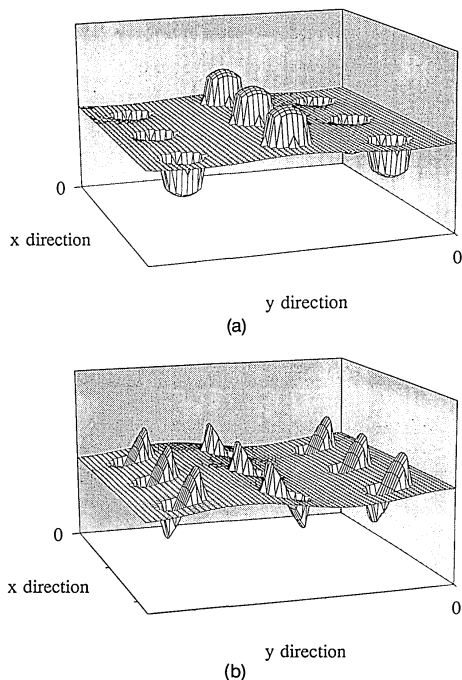
Figure 4.3: TM Displacement field configurations (a) below and (b) above the band gap for the cylinder array. The **D** field is in the z-direction, so it is plotted here as a surface plot over the x-y plane. Figure reproduced from [61].

look similar; the **D** field must traverse both the dielectric and air regions because of the constraint that $\nabla \cdot \mathbf{D} = 0$—the vector nature of **D** ensures both modes are not too dissimilar in frequency. Meade *et al.* thus argue that the *disconnected* nature of the high dielectric space contributes to the frequency gap in the TM modes.

In the case of the square array of square holes, the situation is exactly the opposite. Shown in Figure 4.5, the TM modes below and above the gap are confined well to the dielectric in similar ways, though they remain orthogonal, so their frequencies are similar. In Figure 4.6, however, the TE mode below the gap can continuously traverse the unit cell without exiting the high dielectric medium, ensuring its frequency is low. The mode above the gap is forced out of the high dielectric region to ensure orthogonality with the lower frequency mode, and a large gap forms. In this way, that the dielectric space is *connected* ensures a large gap in the TE modes.

For band gaps in two dimensions, because the band just below the gap exhibits good
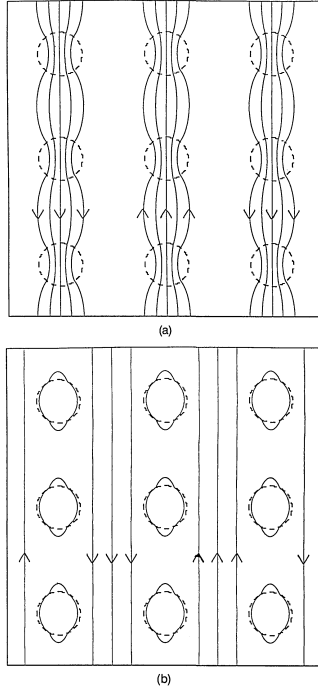
Figure 4.4: TE Displacement field configurations (a) below and (b) above the band gap for the cylinder array. The **D** field is in the x-y plane and obeys the Maxwell equation $\nabla \cdot \mathbf{D} = 0$, so it is divergenceless and continuous. Both modes are of similar frequency. Figure reproduced from [61].
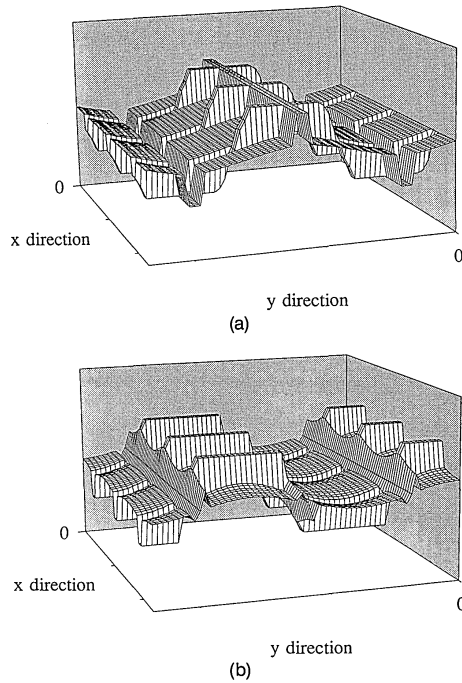
Figure 4.5: TM Displacement field configurations (a) below and (b) above the band gap for the square hole array. Figure reproduced from [61].
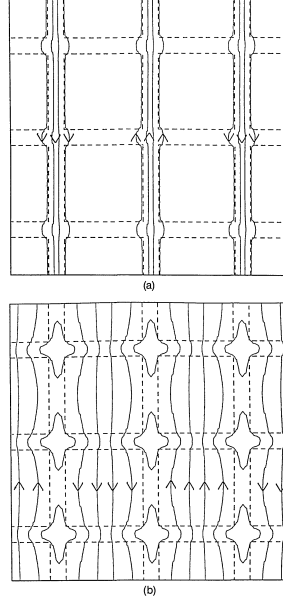
Figure 4.6: TE Displacement field configurations (a) below and (b) above the band gap for the square hole array. Figure reproduced from [61].

confinement of the displacement field to the high dielectric medium, it is called the "dielectric band." The band just above the gap shows modes with fields that penetrate appreciably into the void space, so it is the "air band." This confinement can be quantified with the what Meade terms the fill factor, though I will use the term *concentration factor* so to not confuse it with the dielectric fill fraction ϕ. The concentration factor is a dimensionless measure of the proportion of electric energy density confined to the high dielectric region,

$$f = \frac{\int_{V_\varepsilon} d^d r \; \frac{1}{\varepsilon} \left| \mathbf{D} \right|^2}{\int_V d^d r \; \frac{1}{\varepsilon} \left| \mathbf{D} \right|^2}. \tag{4.21}$$

Here, V is the volume of the unit cell and V_ε is the volume occupied by the high dielectric material. Tables 4.1 and 4.2 show the concentration factors for the modes at the X and M points in bands just below and just above the band gap, recreated from [61]. For most bands, the concentration factor goes down as the band number goes up; decreasing the concentration factor generally increases the frequency. Band gaps for these structures occur between modes with the greatest difference in concentration factor.

56

	k point	f_{diel}	f_{air}
TM	X	0.83	0.32
	M	0.91	0.60
TE	X	0.09	0.23
	M	0.60	0.10

Table 4.1: Concentration factors for square lattice of dielectric cylinders for the band below the gap (dielectric band) and just above the gap (air band). The band gap for this structure lies above the M point and below the X point in the TM mode, highlighted in pink. Table reproduced from [61].

	k point	f_{diel}	f_{air}
TM	X	0.89	0.77
	M	0.92	0.86
TE	X	0.83	0.14
	M	0.84	0.25

Table 4.2: Concentration factors for square lattice of square holes for the band below the gap (dielectric band) and just above the gap (air band). The band gap for this structure lies above the M point and below the X point in the TE mode, highlighted in pink. Table reproduced from [61].

It is generally difficult—though possible—to form a *full* band gap in two dimensions, because the high dielectric space has to be sufficiently disconnected to open a gap in the TM modes but also sufficiently connected to open a gap in the TE modes. In three dimensions, the prospect of such a design is much easier, but the analysis of the fields is necessarily fully vectorial and harder to visualize. In the next subsection, I will examine the field configurations for a small number of representative structures.

4.4.2 Extensions of connectivity principle to three dimensions: examples and counterexamples

The principle of a "dielectric" and an "air" band is sufficient to explain the appearance of gaps in two dimensions, and we find examples in three dimensions where it is also a good framework. In our data are examples of materials that show good confinement to the high dielectric region below the gap and poor confinement above. In this section, I will give a qualitative overview of the modes below and above some selected band gaps in our large

database. For the examples chosen, Table 4.3 lists the concentration factors and band gap sizes.

Configurations of the **D** field are shown in Figures 4.7–4.14. Each mode is normalized such that $\int_V d^3r \; |\mathbf{D}|^2 = 1$. The magnitude of each vector is signified by both its length and its color; green vectors have a large magnitude than blue ones. The regions bound by gray contour are high dielectric material with $\varepsilon = 16$. These visualizations were created using Mayavi [73].

Figure 4.7 shows two modes below and above the gap for the structure tP12-O$_2$Si, or cristobalite, a commonly studied photonic band gap structure [75, 57]. For a sufficiently large dielectric sphere radius, this structure exhibits a completely connected region of high dielectric, such as in the two-dimensional example of the square void structure. The mode below the gap shows smooth, slowly varying field lines flowing through the high dielectric medium, whereas above the gap, field lines are pushed out of the medium into the void space, and field lines within the dielectric are significantly more curled. This structure exhibits a large band gap of 24.3%, likely due to this large difference in concentration factor of $\Delta f = 0.34$.

The three-dimensional analog of the square lattice of voids is a simple cubic lattice of voids; Figure 4.8 shows the modes below and above the band gap for this structure, inverse cP1. Scooping out spherical sections of dielectric on a simple cubic lattice leaves high dielectric regions roughly in the shape of octahedra connected by thin channels. Below the gap, field lines are arranged in a large closed loop that is isolated from other unit cells, unlike tP12-O$_2$Si which has continuous and connected field configurations. Above the gap, significant field density is found outside the dielectric. The differences in concentration factor above and below the gap is 0.3 and the gap is 11.6%.

Finally, the structure tI4-MnY with a radius of $r = 0.20$ exhibits a band gap between bands 14 and 15, relatively high frequency, and the mode profiles are shown in Figure 4.9. Good confinement to the dielectric is achieved in the lower band by each isolated dielectric

sphere hosting a swirling motif of **D** field lines. Above the gap, field lines occur in dipole-like motifs, and the symmetry axes of each sphere are misaligned with all the other spheres. This misalignment ensures the fields need to penetrate significantly into the void space, raising the frequency and opening the gap. Here, the concentration factor difference is 0.43 but the gap size is only 4.8%.

In addition to these three structures that exhibit good concentration factor differences that open their band gaps, we have examples of structures that show gaps without exhibiting significant concentration factor differences. In fact, the same structure tI4-MnY that shows a gap of 4.8% with $\Delta f = 0.43$ shows a gap of 6.1% with only a Δf of 0.12 at a higher dielectric sphere radius. Increasing the radius to $r = 0.29$ connects the dielectric space, and a gap is opened between bands 2 and 3; mode profiles are shown in Figure 4.10. The mode below the gap is characterized by slowly varying, gently curling field lines that connect between unit cells. Above the gap, there are two "lanes" of field lines that run anti-parallel to each other, causing significant local curl inside the dielectric.

Perhaps the most archetypal structure for photonic band gap materials [46, 23, 58, 86, 30], diamond cubic (cF2-C), is capable of exhibiting multiple different band gaps between a variety of different bands; this structure, however, does not open its gaps by optimizing Δf. Diamond cubic is shown for $r = 0.26$ in Figure 4.11 and for $r = 0.33$ in Figures 4.12 and 4.13. At $r = 0.26$, diamond exhibits a gap of 14.5% between bands 8 and 9, but the concentration factors above and below the gap are both 0.74. At this radius, the dielectric spheres are nearly touching but do not connect. Band 8 is characterized by isolated swirling motifs, and band 9 is characterized by isolated dipole-like motifs.

At $r = 0.33$, Figure 4.12 shows modes in bands 2 and 3, which exhibit a gap of 15.2%; the concenration factor difference is $\Delta f = 0.11$. At this density, the dielectric forms a connected network. The picture here is almost the inverse of Figure 4.11; the band below the gap is characterized by a dipole-like configuration that spans both spheres in the unit cell, and the mode above the gap shows swirling modes. The vast difference in curl between these two
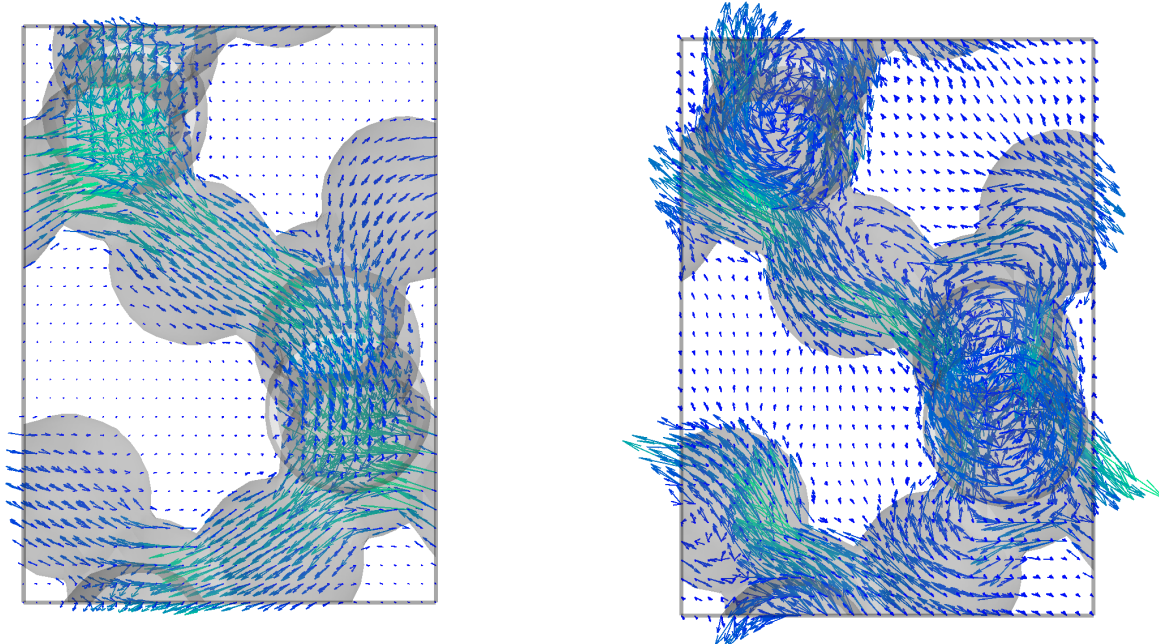
Figure 4.7: Modes in tP12-O$_2$Si, with radius $r = 0.2$. Left is band 4, below the gap; **D** field lines follow the dielectric channels and bend slowly, curling little. Right is band 5, just above the gap; **D** field lines escape the dielectric and fill the void space, raising the frequency significantly above that of band 4. Field lines within the dielectric have much more curl than the mode in band 4.

configurations is likely responsible for opening the gap.

Figure 4.13 shows modes in bands 24 and 25 at the same sphere radius, which exhibit a gap of 4.1%, and the concentration factor difference here is $\Delta f = 0.15$. At these high band numbers, the modes are significantly more complex than at lower bands, and it is not evident from the field configurations what opens this small gap.

Finally, there is a strange example in the structure tP4-PdO that exhibits a small gap of 1.3% between bands 18 and 19 that displays a negative difference in concentration factors; the field of the "dielectric band" has more energy density outside of the dielectric than the "air band" does. Figure 4.14 shows that these modes have a complicated configuration composed of both dipole-like and swirling motifs.

The concentration factor difference is a good explanation of band gap opening in two dimensions, but appears to be an incomplete heuristic in three dimensions. In all of the
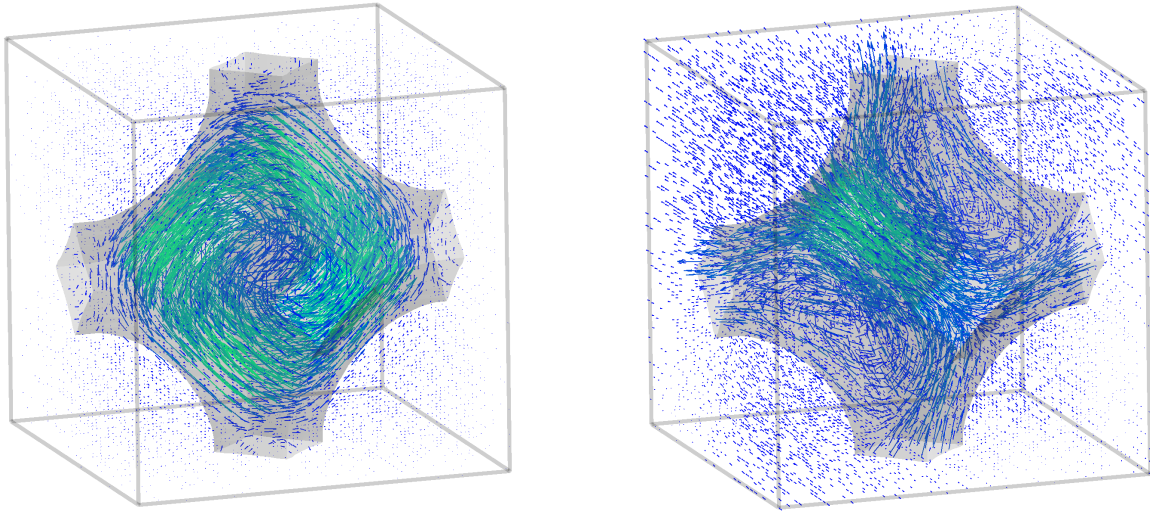
Figure 4.8: Modes in inverse cP1, with void radius of $r = 0.61$. Left is band 5, below the gap; **D** field lines are isolated to a single unit cell in a closed loop. Right is band 6, just above the gap; **D** field lines escape the dielectric, raising the frequency above that of band 5.
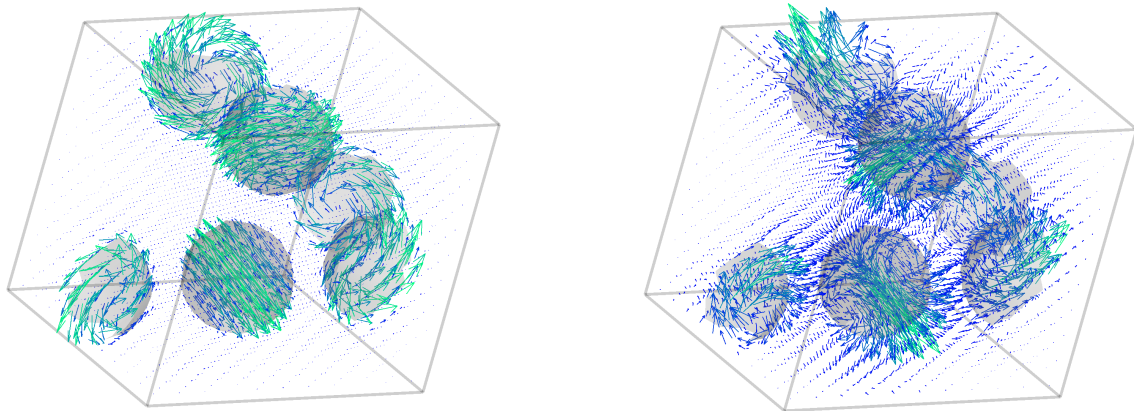
Figure 4.9: Modes in tI4-MnY, with radius $r = 0.20$. Left is band 14, just below the gap; **D** field is well confined in isolated swirling motifs. Right is band 15, just above the gap; **D** field is arranged in dipole-like motifs in isolated dielectric regions.
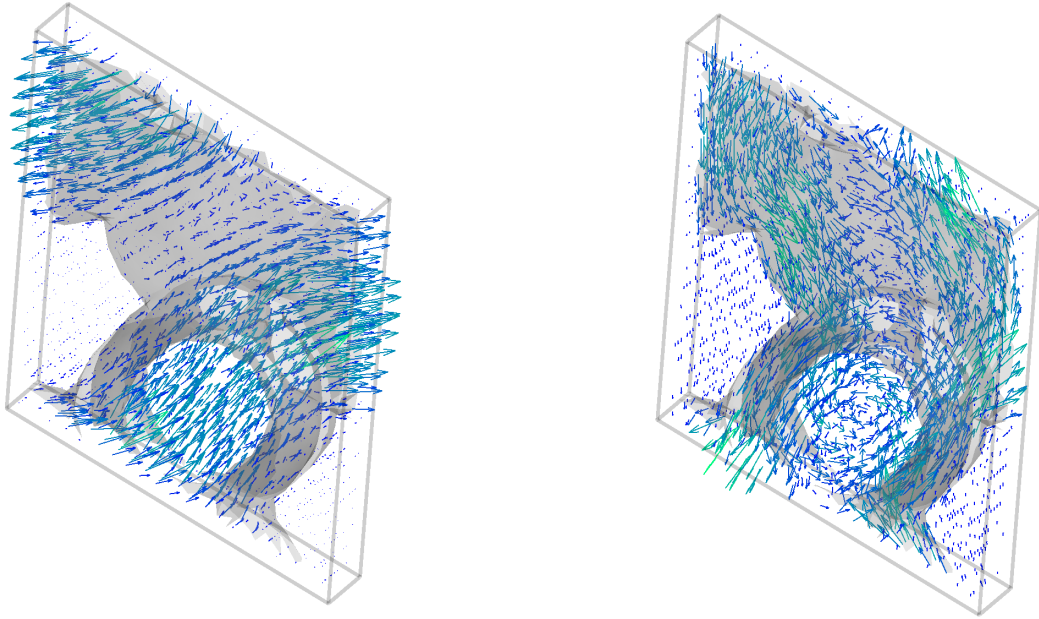
Figure 4.10: Modes in tI4-MnY, with radius $r = 0.29$. Left is band 2, just below the gap; field lines are slowly varying and flow continuously between unit cells. Right is band 3, just above the gap; field lines need to flow past each other, generating local curl, increasing the frequency, and opening the gap.
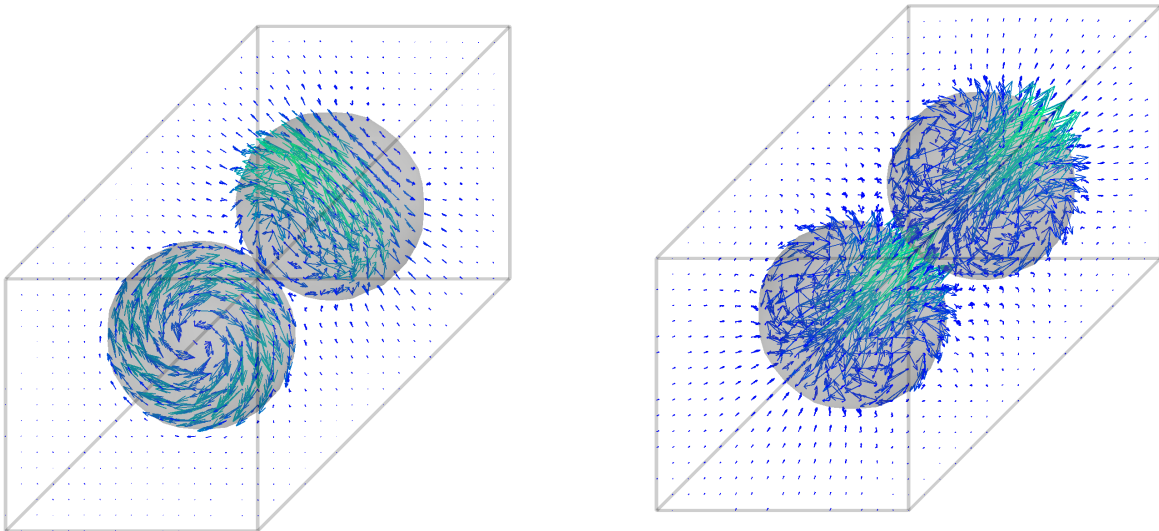
Figure 4.11: Modes in cF2-C, diamond cubic, with $r = 0.26$. Left is band 8, below the gap; swirling motifs are isolated to the disconnected dielectric spheres and little field escapes. Right is band 9, just above the gap; modes are still confined to the dielectric spheres, but exhibit dipole-like configurations.
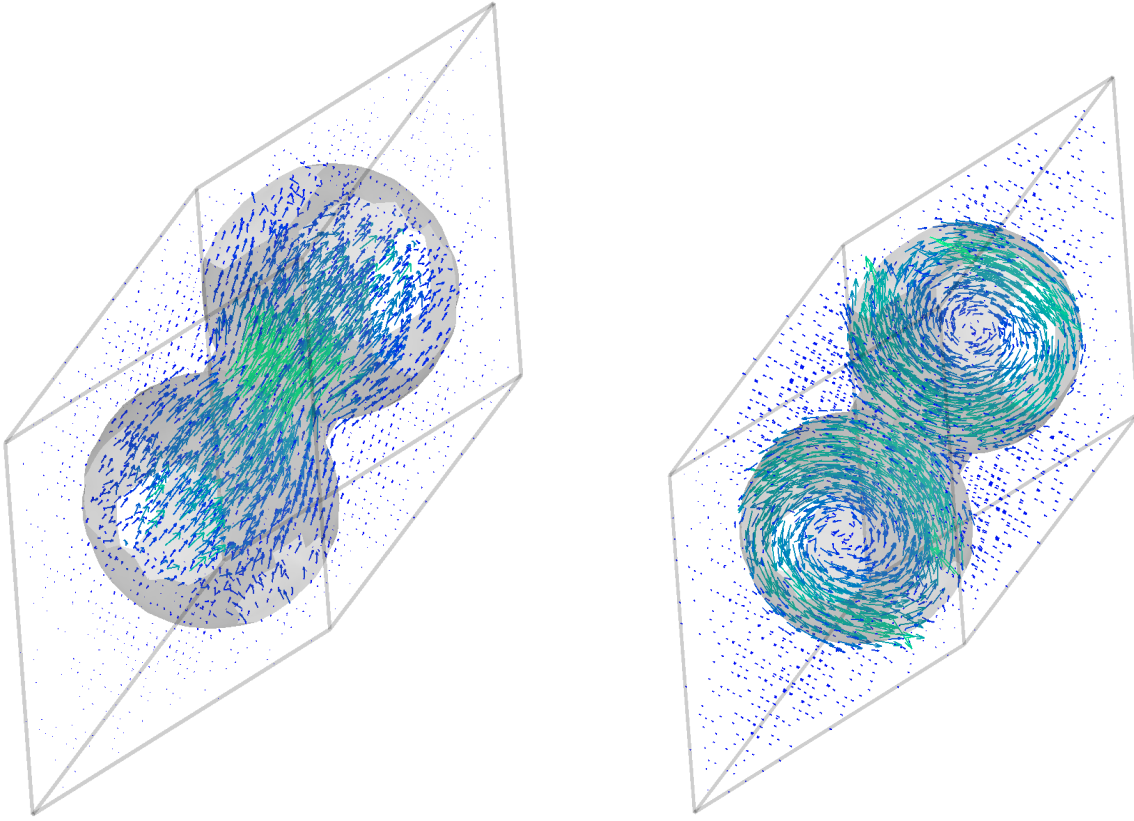
Figure 4.12: Modes in cF2-C, diamond cubic, with $r = 0.33$. Left is band 2, below the gap; field lines flow from one sphere to the other in a large dipole-like configuration. Right is band 3, just above the gap; though the spheres are connected, field lines curl in isolated swirling motifs.

	f_{diel}	f_{air}	$\Delta\omega^*$	Band no.
tP12-O$_2$Si	0.93	0.59	0.243	4–5
cP1 (inv)	0.97	0.67	0.116	5–6
tI4-MnY, $r = 0.20$	0.98	0.55	0.048	14–15
tI4-MnY, $r = 0.29$	0.98	0.86	0.061	2–3
cF2-C, $r = 0.26$	0.74	0.74	0.145	8–9
cF2-C, $r = 0.33$	0.95	0.84	0.152	2–3
cF2-C, $r = 0.33$	0.99	0.84	0.041	24–25
tP4-PdO	0.53	0.64	0.013	18–19

Table 4.3: Concentration factors for modes just below and just above band gaps in a variety of structures. $\Delta\omega^*$ is the nondimensionalized gap width, and band number signifies the location of the gap with how many bands are below the gap.
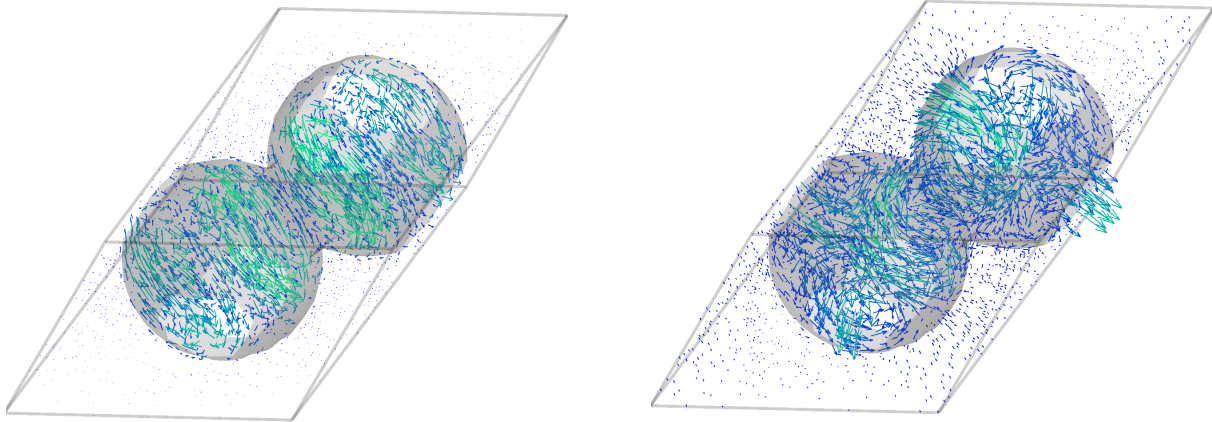
Figure 4.13: Modes in cF2-C, diamond cubic, with $r = 0.33$. Left is band 24, below the gap; field lines are arranged in double-swirl configurations in each sphere. Right is band 25, just above the gap; the field configurations are highly contorted and do not exhibit isolated swirling motifs.
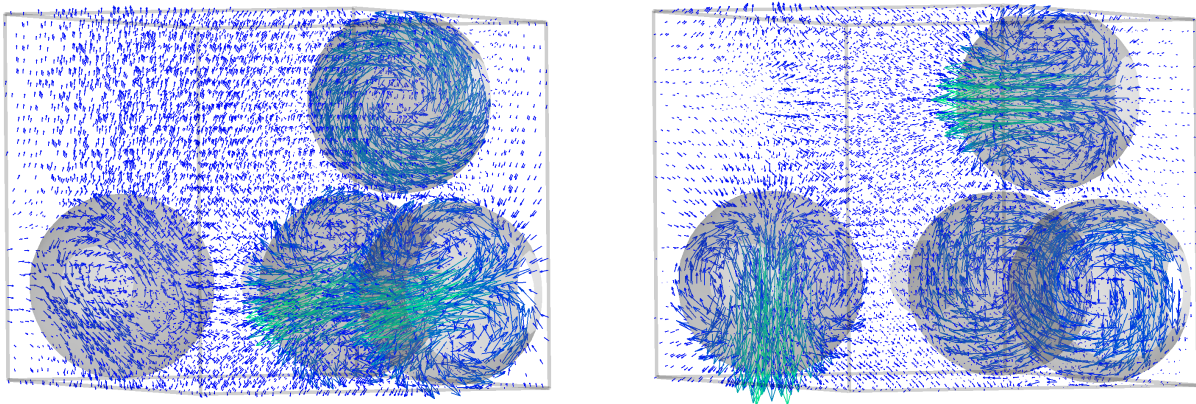
Figure 4.14: Modes in tP4-PdO, with radius $r = 0.25$. Left is band 18, just below the gap; two isolated spheres exhibit a dipole-like motif with axes aligned, one sphere exhibits a swirling motif, and the left-most sphere has little confined field at all. Right is band 19, just above the gap; two spheres again have a dipole-like motif, but at right angles to each other. The remaining two spheres have swirling motifs.

structures shown, however, there is a significant change in symmetry and topology of the mode configurations, even if there is not a large change in concentration factor. Modes can change from swirling to dipole motifs or vice versa across a band gap (Figures 4.9, 4.11, 4.14), or the modes can change from continuous to isolated (Figures 4.7, 4.8, 4.12). In the next section, I will discuss these motifs in the context of vector spherical harmonics.

4.4.3 Common field motifs: vector spherical harmonics

Ohtaka and Tanabe discuss that the iterative solution of the Maxwell eigenproblem is easier basis functions other than plane waves are used. For periodic dielectric media composed of dielectric spheres, vector spherical harmonic waves are good basis functions to solve Maxwell's equations with [67]. To briefly review, two types of vector spherical harmonics, guaranteed to have zero divergence, are used in the context of electromagnetism:

$$\mathbf{D}^M(\mathbf{r}) = i\hat{\mathbf{L}}Y_\ell^m(\theta, \phi), \tag{4.22}$$

$$\mathbf{D}^N(\mathbf{r}) = \frac{1}{q}\nabla \times i\hat{\mathbf{L}}Y_\ell^m(\theta, \phi), \tag{4.23}$$

$$i\hat{\mathbf{L}} = \mathbf{r} \times \nabla. \tag{4.24}$$

Because the spherical harmonics are solutions the Helmholtz equation, the solutions $\mathbf{D}^M(\mathbf{r})$ and $\mathbf{D}^N(\mathbf{r})$ are also guaranteed to be solutions to the Helmholtz equation:

$$\left(\nabla^2 + q^2\right)Y_\ell^m(\theta, \phi) = 0, \tag{4.25}$$

$$\left(\nabla^2 + q^2\right)\begin{pmatrix}\mathbf{D}^M(\mathbf{r})\\\mathbf{D}^N(\mathbf{r})\end{pmatrix} = 0. \tag{4.26}$$

In constant dielectric media, $\varepsilon(\mathbf{r}) = \varepsilon$, the Maxwell eigenproblem reduces simply to this Helmholtz equation, identifying $qc = \omega\sqrt{\varepsilon}$. The notation M and N is taken from Ohtaka and Tanabe [67], who follow the notation of Stratton [78]. For the dielectric media studied

here composed of spherical regions of constant dielectric, it is not surprising that good basis functions for expansion are these vector spherical harmonics.

These vector spherical harmonics are prevalent in many structures we have discussed, diamond cubic at $r = 0.26$ displays both in Figure 4.11. The band below the gap is characterized by M-waves with $\ell = 1$, the swirling motifs, and the band above the gap is characterized by N-waves with $\ell = 1$, the dipole-like motifs. These types of spherical harmonics are excellent approximations when dielectric spheres are well separated, even up to band 18 in the case of tP4-PdO (Figure 4.14). When the dielectric space becomes connected, the motifs must merge and blend together, as demonstrated for diamond cubic at $r = 0.33$ in Figure 4.12. Here, the band below the gap is characterized by two N-like spherical waves that have merged together along the same axis. The band above the gap shows two M-like spherical waves swirling in opposite directions, like two connected rotating gears, which ensures little curl of the **D**-field at the junction between two spheres. In the very high band number gap of diamond cubic with $r = 0.33$, shown in Figure 4.13, the spherical waves are higher order in ℓ. The band below the gap shows M modes with $\ell = 2$ and $m = 0$ or $m = \pm 2$ (changing the value of m simply reorients the primary axis). The band above the gap shows N modes with the same values of ℓ and m.

M and N spherical waves transform differently under inversion, a symmetry group element in many space groups. The swirling M modes transform into themselves under inversion, whereas the N modes pick up a minus sign. The space group symmetry of the photonic crystal strongly constrains the form of the band structure by constraining the *representations* of the space group under which the eigenmodes transform (for a brief overview of representation theory relevant to this band structure problem, see Appendix C). If, in a particular structure, M-like modes are very low energy and N-like modes cause field lines to bleed out into the void space, as in Figure 4.9, the bands belonging to representations even under inversion would likely be comprised mostly of M waves and bands belonging to representations odd under inversion would likely be N waves. Thus, the M-like band would

be far lower in frequency than the N-like band, possibly opening up a gap.

Watanabe and Lu [84] used group theoretical techniques to constrain the band structures of dielectric photonics that exhibit gaps. They determined, for each of the 230 space groups, the minimum number of bands required to connect with each other below and above band gaps, M and M' (not to be confused with the vector spherical harmonic index M). M is the minimum number of bands that must connect with each other and the Γ point below the first band gap. M' is the minimum number of bands that must connect with each other between the first band gap and any second band gap. This theoretical result is useful to constrain the locations of possible band gaps. However, group theoretical predictions must be combined with physics-based intuition; for example, Figures 4.9 and 4.10 show different band gaps and motifs, but belong to the same structure and thus the same space group. Further work on this problem will certainly involve the combination of group theory and the vector spherical harmonic expansion of the eigenmodes. In two dimensions, the presence of a band gap is determined by the behavior of TM and TE polarized modes; it may be the case that M and N spherical waves are the relevant polarizations for investigating 3D band gaps.

CHAPTER V

Conclusions and outlook

In Chapter II, I approximated an entropically stabilized hard particle crystal as a harmonic solid and computed its entropy as contributions from fluctuations of normal modes. *A priori*, the hard hexagon solid had no reason to be approximately harmonic; in fact it seems like a remarkable fact in itself that the structure acted like it was bound by entropic springs. The hexagon solid is a good choice for this approximation, because it exhibits well defined equilibrium positions and orientations. This requirement means that harmonic analysis of liquids, liquid crystals, or plastic crystals, which lack well-defined equilibrium orientations, aren't meaningful. For example, hard pentagons exhibit two solid phases: one is a crystal and one is a rotator crystal. Harmonic mode analysis would only be applicable in the crystal phase, unless the entropy of the orientational degrees of freedom can be estimated another way in the rotator crystal phase.

Regardless of these limitations, harmonic mode analysis is a simple tool to examine the rotational and translational contributions to the entropy. This could find use in analyzing the driving force of solid-solid phase transitions exhibited by some hard particles [32], where harmonic analysis is a good approximation in each phase. The extension to three dimensions is straightforward, though it may be the case that care must be taken to correctly incorporate the non-Abelian nature of the rotation group in three dimensions. Rotations in three dimensions are described by unit quaternions (or equivalently, Pauli matrices), which

are non-commutative. Thus, a harmonic theory for small deviations around an equilibrium quaternion may require more sophisticated mathematical tools than a simple matrix of second derivatives used in two dimensions.

In Chapter III, I reviewed the chiral symmetry breaking transition that hard triangles undergo at high density, and I showed this transition also occurs in hard squares. This continuous transition was shown to belong to the two-dimensional Ising universality class, exhibiting critical exponents $\beta = 1/8$ and $\nu = 1$. Partitioning the entropy by mode across the phase transition showed the system sacrifices translational entropy for rotational entropy in transiting to the chiral phase. I posited the microscopic mechanism likely has to do with the increase of effective vertex repulsion as particles are forced closer together at higher densities, because the phase transition disappears when the polygon corners are rounded. Future work could map out a phase diagram as a function of system density and particle roundness; it must be the case that at some nonzero rounding radius the chiral transition vanishes. Though, rounded polygons may exhibit different kinds of phase transitions at high density that do alter the underlying lattice, as Carmichael and Shell found [17], so this phase diagram may confound the problem rather than illuminate it. Three-dimensional structures can also be examined; hard cubes, for example, could be found to exhibit a chiral symmetry breaking at high densities.

In Chapter IV, I explored the physics of electromagnetic fields in photonic crystals. Along with Rose Cersonsky and Bradley Dice, we found that the heuristics used in two dimensions to form good photonic band gaps are incomplete in three dimensions. I showed counter-examples and motivated them from the perspective of the Maxwell eigenproblem. Immediate work to be done still is a systematic, and likely automated, group theoretical treatment of the band structures from our vast data space.

This problem is afflicted with richness and depth; the design space of potential photonic materials is so vast, and even the data set Rose Cersonsky produced of 2710 structures does not touch on the possibility of metallic photonic crystals, dielectric crystals with anisotropic

dielectric constants, or frequency-dependent dielectric constants. Though, it may be that expanding the search for photonic crystals to those higher-dimensional search spaces would not yield further insight into the electromagnetic eigenproblem. Much more work can be done with the vast database we already have at our disposal. Like the paper that inspired our search into photonics [19], future work could involve a directed search for designer phase transitions for reconfigurable photonic materials.

APPENDICES

APPENDIX A

Properties of Gaussian-distributed random variables

The statistical physics of harmonic Hamiltonians are governed by the statistical properties of Gaussian distributions. Here, I derive rudimentary properties of Gaussian distributions useful for calculating physical properties of harmonic systems.

A general Hamiltonian second order in degrees of freedom x_μ is

$$\beta\mathcal{H} = \frac{1}{2}x_\mu K_{\mu\nu}x_\nu. \tag{A.1}$$

The indices μ and ν run from 1 to N, the number of degrees of freedom, and $K_{\mu\nu}$ is a symmetric, positive-definite matrix, that is, $K_{\mu\nu} = K_{\nu\mu}$ and $x_\mu K_{\mu\nu}x_\nu > 0$ for all configurations x_μ. The partition function of this Hamiltonian is then

$$Z = \int \prod_\mu dx_\mu \, e^{-\frac{1}{2}x_\mu K_{\mu\nu}x_\nu} = \frac{(2\pi)^{N/2}}{\sqrt{\det \mathbf{K}}}. \tag{A.2}$$

Therefore, the probability density over the phase space of x_μ is

$$\rho(x_\mu) = \frac{e^{-\frac{1}{2}x_\mu K_{\mu\nu}x_\nu}}{Z}. \tag{A.3}$$

The moments of this Gaussian distribution can be computed easily by formulating the mo-

ment generating function:

$$Z(J) = \int \prod_\mu dx_\mu \, e^{-\frac{1}{2}x_\mu K_{\mu\nu} x_\nu + J_\mu x_\mu}. \tag{A.4}$$

Derivatives of the function $Z(J)$ with respect to J generate unnormalized moments of the distribution $\rho(x_\mu)$ when $J \to 0$.

$$\frac{\partial Z(J)}{\partial J_\mu} = \int \prod_\mu dx_\mu \, \frac{\partial}{\partial J_\mu} e^{-\frac{1}{2}x_\mu K_{\mu\nu} x_\nu + J_\mu x_\mu} = \int \prod_\mu dx_\mu \, x_\mu e^{-\frac{1}{2}x_\mu K_{\mu\nu} x_\nu + J_\mu x_\mu} \underset{J \to 0}{=} Z \langle x_\mu \rangle. \tag{A.5}$$

Any moment $\langle x_{i_1} x_{i_2} \ldots x_{i_n} \rangle$ is then generated by sequential derivatives of $Z(J)$ with respect to J_{i_1}, $J_{i_2} \ldots J_{i_n}$. The generating function $Z(J)$ can be calculated exactly by completing the square,

$$Z(J) = \int \prod_\mu dx_\mu \, e^{-\frac{1}{2}K_{\mu\nu}\left(x_\mu + K_{\mu\sigma}^{-1} J_\sigma\right)\left(x_\nu + K_{\nu\gamma}^{-1} J_\gamma\right) + \frac{1}{2} J_\sigma K_{\sigma\gamma}^{-1} J_\gamma}.$$

$$Z(J) = \frac{(2\pi)^N}{\sqrt{\det \mathbf{K}}} e^{\frac{1}{2} J_\sigma K_{\sigma\gamma}^{-1} J_\gamma} = Z(0) e^{\frac{1}{2} J_\sigma K_{\sigma\gamma}^{-1} J_\gamma}. \tag{A.6}$$

As an example, here we can show the fourth order correlation function $\langle x_\mu x_\nu x_\sigma x_\gamma \rangle$ breaks up into a sum of products of two-point functions.

$$\langle x_\mu x_\nu \rangle = \frac{1}{Z(0)} \left(\frac{\partial}{\partial J_\mu} \frac{\partial}{\partial J_\nu} Z(0) e^{\frac{1}{2} J_\sigma K_{\sigma\gamma}^{-1} J_\gamma} \right)\bigg|_{J=0} = \left(e^{\frac{1}{2} J_\sigma K_{\sigma\gamma}^{-1} J_\gamma} \left[K_{\mu\nu}^{-1} + K_{\mu\sigma}^{-1} K_{\nu\gamma}^{-1} J_\sigma J_\gamma \right] \right)\bigg|_{J=0}.$$

$$\langle x_\mu x_\nu \rangle = K_{\mu\nu}^{-1}. \tag{A.7}$$

$$\langle x_\mu x_\nu x_\sigma x_\gamma \rangle = \left(\frac{\partial}{\partial J_\mu} \frac{\partial}{\partial J_\nu} \frac{\partial}{\partial J_\sigma} \frac{\partial}{\partial J_\gamma} e^{\frac{1}{2} J_\sigma K_{\sigma\gamma}^{-1} J_\gamma} \right)\bigg|_{J=0}.$$

$$\langle x_\mu x_\nu x_\sigma x_\gamma \rangle = K^{-1}_{\mu\nu} K^{-1}_{\sigma\gamma} + K^{-1}_{\mu\sigma} K^{-1}_{\nu\gamma} + K^{-1}_{\mu\gamma} K^{-1}_{\nu\sigma} = \langle x_\mu x_\nu \rangle \langle x_\sigma x_\gamma \rangle + \langle x_\mu x_\sigma \rangle \langle x_\nu x_\gamma \rangle + \langle x_\mu x_\gamma \rangle \langle x_\nu x_\sigma \rangle \, .$$
$$(A.8)$$

It is a general property of this Gaussian distribution that moments of order $2n$ break up into sums of products of n two-point functions.

APPENDIX B

Hydrodynamic projection operator method for harmonic mode analysis

For a lattice of particles interacting harmonically and not straying too far from their lattice positions, the displacement covariance analysis methods of Section 2.2 are sufficient to calculate correlation functions of normal modes and thus dispersion relations. However, as the system density is decreased, dislocation pairs begin to populate the crystal and allow particles to diffuse. As particles wander arbitrarily far away from their prescribed lattice site, their associated crystal displacement vectors become ill-defined, rendering the Fourier transform in Equation 2.3 of the main text invalid. To say it another way, $\langle \mathbf{r}^i \rangle$, the equilibrium position of particle i becomes undefined over long times. This is not to say that the crystal is ill-defined, because it still has well-defined lattice positions. The particle indices become ill-defined, and so a method that is agnostic to particle identity is required. At these densities, we use the method of Walz and Fuchs [83] which uses the formalism of Zwanzig-Mori projection operators [64, 91] to calculate longitudinal phonon, transverse phonon, and libron modes. Here, we sketch the method briefly and define relevant quantities used to calculate modes with this method.

A liquid in two dimensions has four hydrodynamic modes which arise from four conserved quantities: mass, energy, and both components of momentum. Hydrodynamic modes also

arise in the presence of broken symmetry [34]. In the solid phase the translational order parameters defined by

$$n_{\mathbf{g}} = \frac{1}{V} \sum_{i}^{N} \langle e^{-i\mathbf{g} \cdot \mathbf{r}^i} \rangle \tag{B.1}$$

are nonzero and thus correspond to hydrodynamic variables when $\mathbf{g}$ is any nonzero reciprocal lattice vector ($n_{\mathbf{g}=0}$ is simply the hydrodynamic variable associated with mass conservation, not broken symmetry). The Zwanzig-Mori formalism systematically furnishes the time dependence of any (sufficiently large) set of hydrodynamic variables. In the case of this work, the set of hydrodynamic variables of interest are the density and the translational order parameters $n_{\mathbf{g}}$. The density waves at any given time are defined as

$$\delta n_{\mathbf{g}}(\mathbf{k}, t) = \sum_{i}^{N} e^{-i(\mathbf{g}+\mathbf{k}) \cdot \mathbf{r}^i} - \delta_{\mathbf{k},0} n_{\mathbf{g}}. \tag{B.2}$$

The Zwanzig-Mori formalism better predicts the time dependence of these density waves when $\mathbf{k}$ is small, so the properties of waves near the center of the Brillouin zone ($\mathbf{k} \approx \mathbf{g}$) will be better estimated than those of waves near the edge. Walz and Fuchs show that this set of hydrodynamic modes can be re-expressed in terms of longitudinal and transverse crystal displacement modes,

$$u_{\mu}(\mathbf{k}, t) = i\mathcal{N}_{\mu\nu}^{-1} \sum_{\mathbf{g}} n_{\mathbf{g}}^* g_{\nu} \delta n_{\mathbf{g}}(\mathbf{k}, t). \tag{B.3}$$

The 2×2 matrix $\mathcal{N}$ normalizes the sum over $\mathbf{g}$ and is defined as

$$\mathcal{N}_{\mu\nu} = \sum_{\mathbf{g}} |n_{\mathbf{g}}|^2 g_{\mu} g_{\nu}. \tag{B.4}$$

We use the above definition of the wave amplitudes to compute the dynamical matrix at densities where the definition of $\mathbf{u}^i$ from Equation 2.3 of the main text is ill-defined. The sum over reciprocal lattice vectors $\mathbf{g}$ is, in principle, an unrestricted sum over all possible lattice vectors. In practice, we truncate this sum after including the smallest six $\mathbf{g}$ vectors, which produces dynamical matrices consistent with the DCA method at high densities where

the DCA method is applicable.

The libron modes are found simply with a traditional Fourier transform, as there is no issue defining the equilibrium orientation for each particle even if particles diffuse across lattice sites:

$$\theta(\mathbf{k}, t) = \frac{1}{\sqrt{V}} \sum_i \Delta\theta^i(t) e^{-i\mathbf{k}\cdot\mathbf{r}^i(t)}. \tag{B.5}$$

Here, $\Delta\theta^i(t)$ is the difference between $\theta(t)$ and the equilibrium orientation modulo $2\pi/6$ for hexagons.

APPENDIX C

Group theory, representation theory, and band structure

In the context of any band structure problem, the behavior of the frequency bands $\omega_{\mathbf{k},n}$ is strongly constrained by the space group of the crystal. In this appendix, I use traditional group theory and representation theory tools to examine the Maxwell eigenproblem for photonic crystals. This material is taken from two excellent textbook sources: Dresselhaus, Dresselhaus and Jorio [31] and Sakoda [74].

Following the notation of Section 4.2, for the Maxwell eigenproblem defined by $\Theta \mathbf{H} = (\omega^2/c^2)\mathbf{H}$ (Equation 4.6), a symmetry operation g belonging to the space group G of the crystal can be shown to leave the entire operator Θ invariant,

$$g\Theta \mathbf{H_k} = \Theta g \mathbf{H_k} = \frac{\omega^2}{c^2} g \mathbf{H_k}. \tag{C.1}$$

The action of g on the eigenmode $\mathbf{H_k}$ produces a new mode $\mathbf{H'}_{g\mathbf{k}}$ with the same frequency. The action of all the elements g of G on the wavevector $\mathbf{k}$ produces the "star" of $\mathbf{k}$, the set of inequivalent $\mathbf{k}$-points in the Brillouin zone that host modes of the same frequency. However, if g transforms $\mathbf{k}$ into some $\mathbf{k}'$ that is *equivalent* to $\mathbf{k}$, that is, if $\mathbf{k}' = \mathbf{k} + \mathbf{K}$ with $\mathbf{K}$ some reciprocal lattice vector, then g belongs to the *group of the wavevector* $\mathbf{k}$, $G_{\mathbf{k}}$. These

operations in $G_{\mathbf{k}}$ either leave the eigenmode $\mathbf{H}_{\mathbf{k}}$ invariant or produce another eigenmode $g\mathbf{H}_{\mathbf{k}} = \mathbf{H}'_{\mathbf{k}}$ with the same eigenfrequency at the same point the Brillouin zone $\mathbf{k}$. The group structure of $G_{\mathbf{k}}$ thus governs the patterns of degeneracy at high-symmetry points in the Brillouin zone.

Representation theory is used to determine the degeneracies and the behavior of bands in photonic crystals, which I will briefly review here. In general, there is a set of *degenerate* eigenmodes $\{\mathbf{H}_{\mathbf{k}}^{(1)}, \mathbf{H}_{\mathbf{k}}^{(2)} \ldots \mathbf{H}_{\mathbf{k}}^{(j)}\}$ all with the same frequency $\omega_{\mathbf{k}}$ that transform into each other under the group elements of $G_{\mathbf{k}}$. Any mode at $\mathbf{k}$ with frequency $\omega_{\mathbf{k}}$ can be written as a linear combination of the $\mathbf{H}_{\mathbf{k}}^{(i)}$ which can then be considered to be the *basis functions* for a j-dimensional vector space. The action of a group element $g_{\mathbf{k}}$ on some basis function $\mathbf{H}_{\mathbf{k}}^{(1)}$ produces some linear combination of the basis functions, so $g_{\mathbf{k}}$ acts like a rotation in the vector space of $\mathbf{H}_{\mathbf{k}}^{(j)}$. The action of $g_{\mathbf{k}}$ can then be described by a $j \times j$ matrix $R(g_{\mathbf{k}})$, a *representation* of the group element $g_{\mathbf{k}}$. Each element in $G_{\mathbf{k}}$ is mapped to a matrix $R(g_{\mathbf{k}})$ such that,

$$g_{\mathbf{k},1}g_{\mathbf{k},2} = g_{\mathbf{k},3} \quad \rightarrow \quad R(g_{\mathbf{k},1})R(g_{\mathbf{k},2}) = R(g_{\mathbf{k},3}). \tag{C.2}$$

It also follows that,

$$R(g_{\mathbf{k},1}g_{\mathbf{k},2}) = R(g_{\mathbf{k},1})R(g_{\mathbf{k},2}). \tag{C.3}$$

If we instead choose a different set of basis functions $\{\mathbf{H}_{\mathbf{k}}'^{(1)}, \mathbf{H}_{\mathbf{k}}'^{(2)} \ldots \mathbf{H}_{\mathbf{k}}'^{(j)}\}$, these are necessarily linear combinations of the original unprimed basis functions such that $U\{\mathbf{H}\} = \{\mathbf{H}'\}$. The representations $R(g_{\mathbf{k}})$ then transform to $UR(g_{\mathbf{k}})U^{-1}$. Though the entries of the matrix have changed, this transformation preserves the trace of the matrix, referred to as the *character* χ of the matrix $R(g_{\mathbf{k}})$.

$$\chi^{\Gamma}(g_{\mathbf{k}}) = \mathrm{Tr}R(g_{\mathbf{k}}). \tag{C.4}$$

Here, Γ signifies the particular representation.

A representation is *reducible* if it can be transformed by some choice of U into a block

79

diagonal form:

$$R^{\Gamma_1+\Gamma_2} = \begin{pmatrix} R^{\Gamma_1} & 0 \\ 0 & R^{\Gamma_2} \end{pmatrix}. \tag{C.5}$$

The representation $\Gamma_1+\Gamma_2$ is a direct sum of the representations Γ_1 and Γ_2. If no transformation exists to bring a representation to block diagonal form, the representation is *irreducible*. The groups $G_{\mathbf{k}}$ have a finite number of irreducible representations (irreps). Furthermore, the character of a reducible representation is the sum of the characters of the irreducible representations that comprise it.

If $g_{1,\mathbf{k}} = h_{\mathbf{k}} g_{2,\mathbf{k}} h_{\mathbf{k}}^{-1}$ for $h_{\mathbf{k}}$ any arbitrary element of $G_{\mathbf{k}}$, then $g_{1,\mathbf{k}}$ and $g_{2,\mathbf{k}}$ belong to the same *conjugacy class*, or they are *conjugate*. Representations of group elements that belong to the same class have the same character, using Equation C.2 and the properties of the trace, (briefly suppressing the $\mathbf{k}$ subscripts)

$$\mathrm{Tr}R(g_1) = \mathrm{Tr}R(hg_2h^{-1}) = \mathrm{Tr}\left[R(h)R(g_2)R(h^{-1})\right] = \mathrm{Tr}R(h)\mathrm{Tr}R(g_2)\mathrm{Tr}R(h^{-1}) = \mathrm{Tr}R(g_2). \tag{C.6}$$

It can be shown that the number of conjugacy classes of a group is equal to the number of irreps. The relationship between the the conjugacy classes of a group, the group's irreps, and the characters of those irreps is summarized by a *character table*. As an example, the character table of the point group O_h, which is the symmetry group $G_{\mathbf{k}}$ for simple cubic at $\mathbf{k} = 0$ (signified as the Γ point in k-space) is shown in Table C.1. The identity operation, E, under any representation is the unit matrix, so the character of E is simply the dimension of the representation (the trace of a unit matrix is its dimension). The group O_h has ten irreps of one, two, or three dimensions; it thus will never be the case that four or more modes related to each other by symmetry operations of O_h have the same degenerate frequency.

Off of the Γ-point, the group of the wavevector $G_{\mathbf{k}}$ is generally reduced. For example, at the Δ-point when $\mathbf{k} = (2\pi/a, 0, 0)$, the point group characterizing the symmetry operations that leave this wavevector invariant is C_{4v}, which has only eight elements (O_h has 48

O_h	E	$3C_4^2$	$6C_4$	$6C_2$	$8C_3$	i	$3iC_4^2$	$6iC_4$	$6iC_2$	$8iC_3$
Γ_1^+	1	1	1	1	1	1	1	1	1	1
Γ_2^+	1	1	−1	−1	1	1	1	−1	−1	1
Γ_{12}^+	2	2	0	0	−1	2	2	0	0	−1
Γ_{15}^+	3	−1	1	−1	0	3	−1	1	−1	0
Γ_{25}^+	3	−1	−1	1	0	3	−1	−1	1	0
Γ_1^-	1	1	1	1	1	−1	−1	−1	−1	−1
Γ_2^-	1	1	−1	−1	1	−1	−1	1	1	−1
Γ_{12}^-	2	2	0	0	−1	−2	−2	0	0	1
Γ_{15}^-	3	−1	1	−1	0	−3	1	−1	1	0
Γ_{25}^-	3	−1	−1	1	0	−3	1	1	−1	0

Table C.1: Character table for the point group O_h, which characterizes the symmetries of simple cubic at the Γ point ($\mathbf{k} = 0$). The columns are labeled by the operations of each conjugacy class: E is the identity operation, $3C_4^2$ are rotations by π around the three four-fold axes (100), $6C_4$ are rotations by $\pi/2$ or $-\pi/2$ around the three four-fold axes, $6C_2$ are rotations by π around the six two-fold axes (110), $8C_3$ are rotations by $2\pi/3$ around the eight three-fold axes (111), and i is inversion about the center. Each rotation can be compounded with inversion to form roto-inversions. The rows are listed by the ten irreps of O_h, labeled under the Bouckaert notation [15]. There are four 1d irreps, two 2d irreps, and four 3d irreps; these are the only allowed number of degeneracies at the Γ point. The structure of the O_h group prohibits, for example, four-fold degeneracies.

C_{4v}	E	C_4^2	$2C_4$	$2iC_4^2$	$2iC_2$
Δ_1	1	1	1	1	1
Δ_2	1	1	−1	1	−1
Δ_1'	1	1	−1	−1	1
Δ_2'	1	1	1	−1	−1
Δ_5	2	−2	0	0	0

Table C.2: Character table for the point group C_{4v}, which characterizes the symmetries of simple cubic at the Δ point ($\mathbf{k} = (2\pi/a, 0, 0)$). The columns are labeled by the operations of each conjugacy class: E is the identity operation, C_4^2 are rotations by π around the four-fold axis along the x-axis (100), C_4 are rotations by $\pi/2$ or $-\pi/2$ around the four-fold axis along the (100) axis, $2iC_4^2$ are rotoinversions by π around either the (010) or (001) axis, and $2iC_2$ are rotoinversions by π around either the (011) or (01$\bar{1}$) axis. The rows are listed by the five irreps of C_{4v}. There are four 1d irreps and only one 2d irrep.

elements). The character table for this group is shown in Table C.2. Generally, modes that are degenerate at one high-symmetry point can split when the symmetry is reduced; moving off from Γ to Δ in the Brillouin zone reduces the symmetry and lifts degeneracies. In a band diagram, bands that converge at Γ will diverge when moving onto Δ. Representation theory can also be used to determine how degeneracies will be lifted when moving from a high symmetry point to a lower one. C_{4v} is a subgroup of O_h, so some symmetry operations are preserved under the symmetry reduction, and so are the characters of those symmetry operations. For symmetry operations in both O_h and C_{4v}, representations of O_h must be reducible to representations of C_{4v}. For example, the O_h irrep Γ_{15}^+ must break up into at least two irreps of C_{4v}, because C_{4v} does not have any 3d irreps. By comparing characters for the operations common to both O_h and C_{4v}, it must be the case that $\Gamma_{15}^+ \to \Delta_1 + \Delta_5$. This decomposition is unique, and these relations that describe how representations of higher order symmetries break up into representations of lower order ones are called *compatibility relations*. The compatibility relations for any group $G_{\mathbf{k}}$ to any other group $G_{\mathbf{k}'}$ are known for all 230 space groups [10, 9, 11]. $\Gamma_{15}^+ \to \Delta_1 + \Delta_5$ entails that the triple degeneracy at $\mathbf{k} = 0$ (described by Γ_{15}^+) is lifted to a two-fold degeneracy (described by Δ_5) and a non-degenerate mode (described by Δ_1).

Each band can be labeled by its representation at each point in the Brillouin zone, and the compatibility relations determine how the representations of a group of bands change over the Brillouin zone. In general, the highest frequency below a band gap (and the lowest frequency above the gap) can occur at any point in the Brillouin zone; representation theory allows a unique connection from those arbitrary points to, for example, the Γ-point. This unique connection to the Γ-point classifies the bands below and above band gaps by their representations. Using group theory and representation theory provides a theoretically well-founded way to determine the role space group symmetries play in determining the band gaps of photonic crystals.

BIBLIOGRAPHY

BIBLIOGRAPHY

[1] Carl S. Adorf, Paul M. Dodd, Vyas Ramasubramani, and Sharon C. Glotzer. Simple data and workflow management with the signac framework. *Computational Materials Science*, 146:220–229, 2018.

[2] Umang Agarwal and Fernando A. Escobedo. Mesophase behaviour of polyhedral particles. *Nat. Mater.*, 10:230–235, 2011.

[3] B.J. Alder and T.E. Wainwright. Phase transition for a hard sphere system. *J. Chem. Phys.*, 27(5):1208–1209, 1957.

[4] J Anderson, C Lorenz, and A Travesset. General purpose molecular dynamics simulations fully implemented on graphics processing units. *J. Comp. Phys.*, 227(10):5342–5359, 2008.

[5] Joshua A Anderson, James Antonaglia, Jaime A Millan, Michael Engel, and Sharon C Glotzer. Shape and symmetry determine two-dimensional melting transitions of hard regular polygons. *Phys. Rev. X*, 7(2):021001, 2017.

[6] Joshua A Anderson, M Eric Irrgang, and Sharon C Glotzer. Scalable Metropolis Monte Carlo for simulation of hard shapes. *Comp. Phys. Commun.*, 204:21–30, 2016.

[7] James Antonaglia, Greg van Anders, and Sharon C. Glotzer. Mapping disorder in entropically ordered crystals. *Submitted*, 2019.

[8] Richard Dacre Archer-Hind et al. *The Timaeus of Plato*. Macmillan, 1888.

[9] M.I. Aroyo, J.M. Perez-Mato, D. Orobengoa, E. Tasci, G. De La Flor, and A. Kirov. Crystallography online: Bilbao crystallographic server. *Bulgarian Chemical Communications*, 43(2):183–197, 2011. cited By 179.

[10] Mois I. Aroyo, Asen Kirov, Cesar Capillas, J. M. Perez-Mato, and Hans Wondratschek. Bilbao crystallographic server. II. Representations of crystallographic point groups and space groups. *Acta Crystallographica Section A*, 62(2):115–128, Mar 2006.

[11] Mois Ilia Aroyo, Juan Manuel Perez-Mato, Cesar Capillas, Eli Kroumova, Svetoslav Ivantchev, Gotzon Madariaga, Asen Kirov, and Hans Wondratschek. Bilbao crystallographic server: I. Databases and crystallographic computing programs. *Zeitschrift für Kristallographie-Crystalline Materials*, 221(1):15–27, 2006.

[12] Neil W Ashcroft and N David Mermin. *Solid State Physics*. Holt, Rinehart, and Winston, 1976.

[13] K. Binder. Finite size effects on phase transitions. *Ferroelectrics*, 73(1):43–67, 1987.

[14] R Biswas, M M Sigalas, G Subramania, and K.-M Ho. Photonic band gaps in colloidal systems. *Physical Review B*, 57(7):3701–3705, feb 1998.

[15] L. P. Bouckaert, R. Smoluchowski, and E. Wigner. Theory of Brillouin zones and symmetry properties of wave functions in crystals. *Phys. Rev.*, 50:58–67, Jul 1936.

[16] Tomas Brauner and Haruki Watanabe. Spontaneous breaking of spacetime symmetries and the inverse higgs effect. *Phys. Rev. D*, 89:085004, Apr 2014.

[17] Scott P Carmichael and M Scott Shell. A simple mechanism for emergent chirality in achiral hard particle assembly. *The Journal of Chemical Physics*, 139(16):164705, oct 2013.

[18] Rose K. Cersonsky, James Antonaglia, Bradley D. Dice, and Sharon C. Glotzer. Untangling the role of connectivity in 3D photonic crystals. *In preparation*.

[19] Rose K Cersonsky, Julia Dshemuchadse, James Antonaglia, Greg van Anders, and Sharon C Glotzer. Pressure-tunable photonic band gaps in an entropic colloidal crystal. *Physical Review Materials*, 2(12):125201, 2018.

[20] Paul M Chaikin, Tom C Lubensky, and Thomas A Witten. *Principles of condensed matter physics*, volume 1. Cambridge university press Cambridge, 1995.

[21] C. T Chan, K. M Ho, and C M Soukoulis. Photonic band gaps in experimentally realizable periodic dielectric structures. *Europhysics Letters (EPL)*, 16(6):563–568, oct 1991.

[22] Zhengdong Cheng, Jixiang Zhu, William B. Russel, and P. M. Chaikin. Phonons in an entropic crystal. *Physical Review Letters*, 85(7):1460–1463, 2000.

[23] Alongkarn Chutinan and Susumu Noda. Spiral three-dimensional photonic-band-gap structure. *Physical Review B*, 57(4):R2006–R2008, jan 1998.

[24] Rudolph Clausius. *Abhandlungen Über Die Mechanische Wärmetheorie*. Friedrich Vieweg und Sohn, Braunschweig, 1864.

[25] Cornelius F Coll III and A Brooks Harris. Effect of anharmonic libron interactions on the single-libron spectrum of solid H_2 and D_2. *Physical Review B*, 4(8):2781, 1971.

[26] D. W. J. Cruickshank. The analysis of the anisotropic thermal motion of molecules in crystals. *Acta Crystallographica*, 9:754–756, 1956.

[27] Pablo F Damasceno, Michael Engel, and Sharon C Glotzer. Crystalline assemblies and densest packings of a family of truncated tetrahedra and the role of directional entropic forces. *Acs Nano*, 6(1):609–614, 2011.

[28] Pablo F Damasceno, Michael Engel, and Sharon C Glotzer. Predictive self-assembly of polyhedra into complex structures. *Science*, 337(6093):453–457, 2012.

[29] D. Dlott. Optical phonon dynamics in molecular crystals. *Annual Review of Physical Chemistry*, 37(1):157–187, 1986.

[30] James A. Dolan, Bodo D. Wilts, Silvia Vignolini, Jeremy J. Baumberg, Ullrich Steiner, and Timothy D. Wilkinson. Optical properties of gyroid structured materials: From photonic crystals to metamaterials. *Advanced Optical Materials*, 3(1):12–32, jan 2015.

[31] Mildred S. Dresselhaus, Gene Dresselhaus, and Ado Jorio. *Group Theory: Application to the Physics of Condensed Matter*. Springer Berlin Heidelberg, Berlin, Heidelberg, jun 2008.

[32] Chrisy Xiyu Du, Greg van Anders, Richmond S Newman, and Sharon C Glotzer. Shape-driven solid-solid transitions in colloids. *Proceedings of the National Academy of Sciences*, 114(20):E3892–E3899, 2017.

[33] R. Eppenga and D. Frenkel. Monte Carlo study of the isotropic and nematic phases of infinitely thin hard platelets. *Molecular Physics*, 52(6):1303–1334, aug 1984.

[34] Dieter Forster. Hydrodynamic fluctuations, broken symmetry, and correlation functions. In *Reading, Mass., WA Benjamin, Inc.(Frontiers in Physics. Volume 47), 1975. 343 p.*, volume 47, 1975.

[35] Daan Frenkel. Entropy-driven phase transitions. *Physica A: Statistical Mechanics and its Applications*, 263(14):26 – 38, 1999.

[36] Daan Frenkel. Order through entropy. *Nat. Mater.*, 14:9–12, 2015.

[37] Anjan P Gantapara, Weikai Qi, and Marjolein Dijkstra. A novel chiral phase of achiral hard triangles and an entropy-driven demixing of enantiomers. *Soft Matter*, 11(44):8684–8691, 2015.

[38] Jens Glaser, Trung Dac Nguyen, Joshua A Anderson, Pak Lui, Filippo Spiga, Jaime A Millan, David C Morse, and Sharon C Glotzer. Strong scaling of general-purpose molecular dynamics simulations on GPUs. *Comp. Phys. Commun.*, 192:97–107, 2015.

[39] Nigel Goldenfeld. *Lectures on Phase Transitions and the Renormalization Group*. CRC Press, 2018.

[40] Saulius Gražulis, Adriana Daškevič, Andrius Merkys, Daniel Chateigner, Luca Lutterotti, Miguel Quirós, Nadezhda R. Serebryanaya, Peter Moeck, Robert T. Downs, and Armel Le Bail. Crystallography open database (COD): An open-access collection of crystal structures and platform for world-wide collaboration. *Nucleic Acids Research*, 40(D1):D420–D427, 2012.

[41] Amir Haji-Akbari, Michael Engel, Aaron S. Keys, Xiaoyu Zheng, Rolfe G. Petschek, Peter Palffy-Muhoray, and Sharon C. Glotzer. Disordered, quasicrystalline and crystalline phases of densely packed tetrahedra. *Nature*, 462:773–777, 2009.

[42] Mariette Hellenbrandt. The inorganic crystal structure database (ICSD): Present and future. *Crystallography Reviews*, 10(1):17–22, 2004.

[43] Joel Henzie, Michael Grünwald, Asaph Widmer-Cooper, Phillip L. Geissler, and Peidong Yang. Self-assembly of uniform polyhedral silver nanocrystals into densest packings and exotic superlattices. *Nat. Mater.*, 11:131–137, 2012.

[44] Berk Hess. Similarities between principal components of protein dynamics and random diffusion. *Phys. Rev. E*, 62(6):8438, 2000.

[45] R. M Hexter and D. A Dows. Low-frequency librations and the vibrational spectra of molecular crystals. *The Journal of Chemical Physics*, 25(3):504–509, 1956.

[46] K. M. Ho, C. T. Chan, and C. M. Soukoulis. Existence of a photonic gap in periodic dielectric structures. *Physical Review Letters*, 65(25):3152–3155, dec 1990.

[47] K.M. Ho, C.T. Chan, C.M. Soukoulis, R. Biswas, and M. Sigalas. Photonic band gaps in three dimensions: New layer-by-layer periodic structures. *Solid State Communications*, 89(5):413–416, feb 1994.

[48] Katsuya Honda. On a hard-sphere crystal. *Prog. Theor. Phys.*, 55(4):1024–1037, 1976.

[49] Jérôme Houdayer and Alexander Hartmann. Low-temperature behavior of two-dimensional Gaussian Ising spin glasses. *Physical Review B*, 70(1):014418, jul 2004.

[50] J.D. Joannopoulos. *Photonic Crystals: Molding the Flow of Light, 2nd Edition*. Princeton University Press, 2008.

[51] Steven Johnson and John Joannopoulos. Block-iterative frequency-domain methods for Maxwell's equations in a planewave basis. *Optics Express*, 8(3):173, jan 2001.

[52] Jonathan C Knight, Jes Broeng, Tim A Birks, and P St J Russell. Photonic band gap guidance in optical fibers. *Science*, 282(5393):1476–1478, 1998.

[53] Kenji K. Kobayashi. Theory of translational and orientational melting with application to liquid crystals. I. *Journal of the Physical Society of Japan*, 29(1):101–105, 1970.

[54] J.M. Kosterlitz and Nelson D.R. Universal jump in the superfluid density of two-dimensional superfluids. *Phys. Rev. Lett.*, 39(19):1201, 1977.

[55] D. P. Landau. Finite-size behavior of the Ising square lattice. *Physical Review B*, 13(7):2997–3011, 1976.

[56] Lev Davidovich Landau. On the theory of phase transitions. *Zh. Eksp. Teor. Fiz.*, 11:19, 1937.

[57] Sung-En Lin, Bang-Ying Yu, Jing-Jong Shuye, and Wen-Cheng J Wei. Photoluminescence and microstructure investigation of SiO_2@Y:Eu photonic bandgap crystals. *Journal of the American Ceramic Society*, 91(12):3976–3980, 2008.

[58] Martin Maldovan and Edwin L Thomas. Diamond-structured photonic crystals. *Nature Materials*, 3(9):593–600, sep 2004.

[59] Martin Maldovan, Chaitanya K. Ullal, W. Craig Carter, and Edwin L. Thomas. Exploring for 3D photonic bandgap structures in the 11 f.c.c. space groups. *Nature Materials*, 2(10):664–667, oct 2003.

[60] Kenny Mayoral and Thomas G. Mason. Entropic chiral symmetry breaking in self-organized two-dimensional colloidal crystals. *Soft Matter*, 10(25):4471, 2014.

[61] R. D. Meade, A. M. Rappe, K. D. Brommer, and J. D. Joannopoulos. Nature of the photonic band gap: some insights from a field analysis. *Journal of the Optical Society of America B*, 10(2):328, feb 1993.

[62] Robert D Meade, A Devenyi, JD Joannopoulos, OL Alerhand, DA Smith, and K Kash. Novel applications of photonic band gap materials: Low-loss bends and high Q cavities. *Journal of applied physics*, 75(9):4753–4755, 1994.

[63] Oliver Melchert. autoScale.py - a program for automatic finite-size scaling analyses: A user's guide. *arXiv preprint arXiv:0910.5403*, 2009.

[64] Hazime Mori. Transport, collective motion, and Brownian motion. *Progress of theoretical physics*, 33(3):423–455, 1965.

[65] DR Nelson and BI Halperin. Dislocation-mediated melting in two dimensions. *Phys. Rev. B*, 19(5), 1979.

[66] Peter Nightingale. Finite-size scaling and phenomenological renormalization (invited). *Journal of Applied Physics*, 53(11):7927–7932, nov 1982.

[67] Kazuo Ohtaka and Yukito Tanabe. Photonic bands using vector spherical waves. III. group-theoretical treatment. *Journal of the Physical Society of Japan*, 65(8):2670–2684, 1996.

[68] Lars Onsager. The effects of shape on the interaction of colloidal particles. *Ann. New York Acad. Sci.*, 51(4):627–659, may 1949.

[69] E. Özbay, A Abeyta, G Tuttle, M Tringides, R Biswas, C T Chan, C M Soukoulis, and K M Ho. Measurement of a three-dimensional photonic band gap in a crystal structure made of dielectric rods. *Physical Review B*, 50(3):1945–1948, jul 1994.

[70] Nikoletta Pakalidou, David L Cheung, Andrew J Masters, and Carlos Avendaño. Macroscopic chiral symmetry breaking in monolayers of achiral nonconvex platelets. *Soft Matter*, 13(45):8618–8624, 2017.

[71] Linus Pauling. The rotational motion of molecules in crystals. *Physical Review*, 36, 1930.

[72] Sander Pronk and Daan Frenkel. Large difference in the elastic properties of fcc and hcp hard-sphere crystals. *Phys. Rev. Lett.*, 90(25 Pt 1):255501, 2003.

[73] P Ramachandran and G Varoquaux. Mayavi: 3D visualization of scientific data. *Computing in Science & Engineering*, 13(2):40–51, 2011.

[74] Kazuaki Sakoda. *Optical Properties of Photonic Crystals*, volume 80 of *Springer Series in Optical Sciences*. Springer Berlin Heidelberg, Berlin, Heidelberg, 2001.

[75] Alexander S Sinitskii, Alexander V Knot'ko, and Yuri D Tretyakov. Silica photonic crystals: Synthesis and optical properties. *Solid state ionics*, 172(1-4):477–479, 2004.

[76] Andreas Sorge. pyfssa 0.7.6, 2015.

[77] Frank H. Stillinger. Elasticity in rigid-disk and -sphere crystals. *J. Chem. Phys.*, 46(10):3962, 1967.

[78] JA Stratton. *Electromagnetic Theory*. McGraw-Hill, 1941.

[79] Marc Thevenot, Cyril Cheype, Alain Reineix, and Bernard Jecko. Directive photonic-bandgap antennas. *IEEE Transactions on microwave theory and techniques*, 47(11):2115–2122, 1999.

[80] O Toader and S John. Proposed square spiral microfabrication architecture for large three-dimensional photonic band gap crystals. *Science (New York, N.Y.)*, 292(5519):1133–5, may 2001.

[81] Greg van Anders, N. Khalid Ahmed, Ross Smith, Michael Engel, and Sharon C. Glotzer. Entropically patchy particles: Engineering valence through shape entropy. *ACS Nano*, 8:931–940, 2014.

[82] Greg van Anders, Daphne Klotsa, N. Khalid Ahmed, Michael Engel, and Sharon C. Glotzer. Understanding shape entropy through local dense packing. *Proc. Natl. Acad. Sci. U.S.A.*, 111:E4812–E4821, 2014.

[83] C. Walz and M. Fuchs. Displacement field and elastic constants in nonideal crystals. *Phys. Rev. B*, 81(13):134110, apr 2010.

[84] Haruki Watanabe and Ling Lu. Space group theory of photonic bands. *Physical Review Letters*, 121(26):263903, dec 2018.

[85] Haruki Watanabe and Hitoshi Murayama. Redundancies in Nambu-Goldstone bosons. *Phys. Rev. Lett.*, 110(18):2401–2420, 2013.

[86] Meinhard Wohlgemuth, Nataliya Yufa, James Hoffman, and Edwin L Thomas. Triply periodic bicontinuous cubic microdomain morphologies by symmetries. *Macromolecules*, 34(17):6083–6089, aug 2001.

[87] KW Wojciechowski and AC Brańka. Elastic moduli of a perfect hard disc crystal in two dimensions. *Physics Letters A*, 134(5):314–318, 1989.

[88] W. W. Wood and J. D. Jacobson. Preliminary results from a recalculation of the Monte Carlo equation of state of hard spheres. *J. Chem. Phys.*, 27(5):1207–1208, 1957.

[89] Kun Zhao, Robijn Bruinsma, and Thomas G. Mason. Local chiral symmetry breaking in triatic liquid crystals. *Nature Communications*, 3(1):801, jan 2012.

[90] Kun Zhao and Thomas G Mason. Self-organized chiral colloidal crystals of Brownian square crosses. *Journal of Physics: Condensed Matter*, 26(15):152101, apr 2014.

[91] Robert Zwanzig. Time-correlation functions and transport coefficients in statistical mechanics. *Annual Review of Physical Chemistry*, 16(1):67–102, 1965.